# Aerosol Synthesis and Characterization of Heterogeneous Bimetallic Nanoparticles

Snellman, Markus

2023

*Document Version:*
Publisher's PDF, also known as Version of record

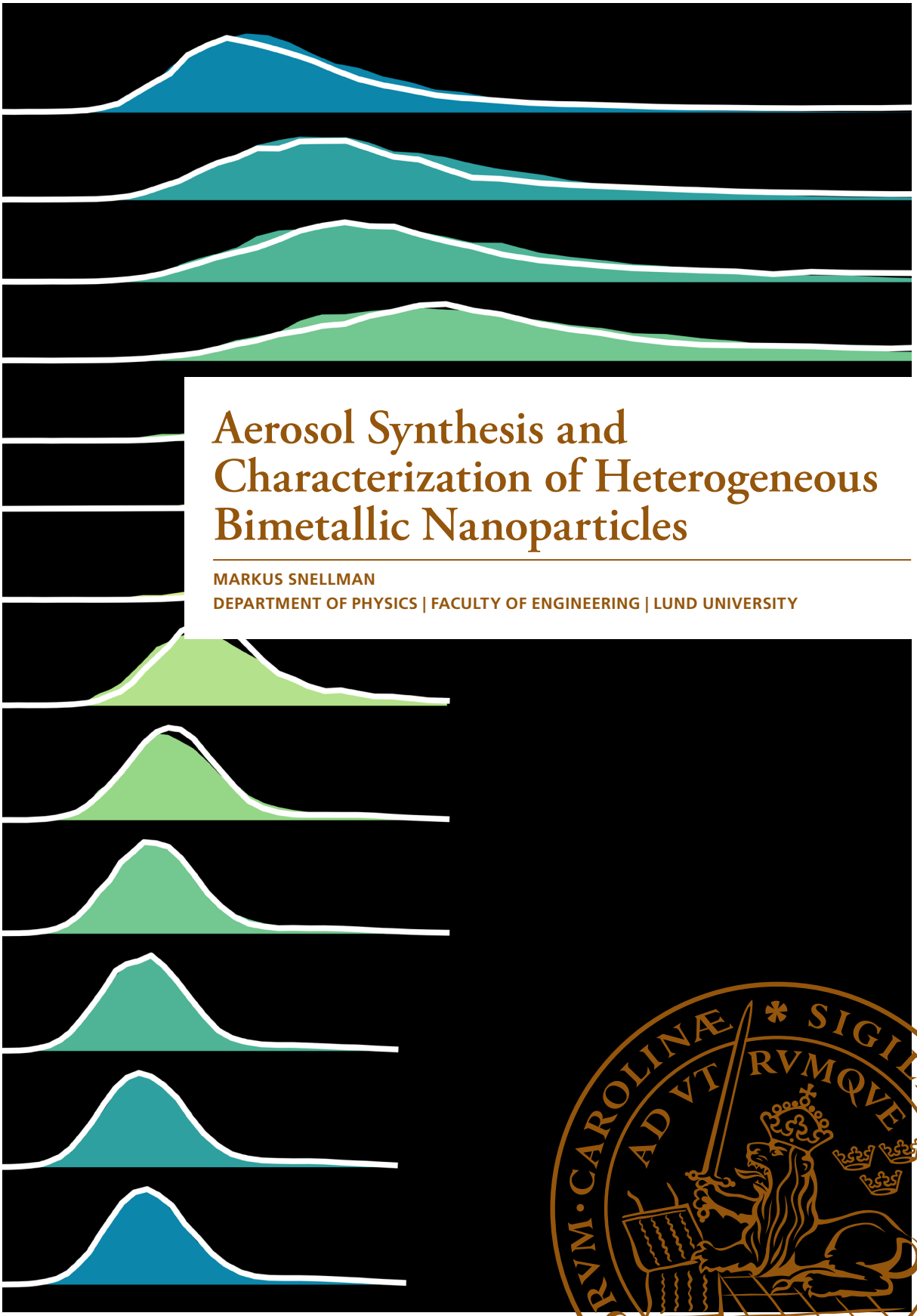

# Aerosol Synthesis and Characterization of Heterogeneous Bimetallic Nanoparticles

MARKUS SNELLMAN
DEPARTMENT OF PHYSICS | FACULTY OF ENGINEERING | LUND UNIVERSITY

Aerosol Synthesis and Characterization of Heterogeneous Bimetallic Nanoparticles

# Aerosol Synthesis and Characterization of Heterogeneous Bimetallic Nanoparticles

Markus Snellman


LUND
UNIVERSITY

DOCTORAL DISSERTATION

Doctoral dissertation for the degree of Doctor of Philosophy (PhD) at the Faculty of Engineering at Lund University to be publicly defended on December 1st, 2023, at 09.15 in Rydberg Hall, Department of Physics, Sölvegatan 14, Lund, Sweden.

*Thesis advisor*
Prof. Knut Deppert

*Co-supervisors*
Dr. Maria E. Messing, Dr. Namsoon Eom, Dr. Martin Ek & Dr. Rasmus Westerström

*Faculty opponent*
Dr. Martin Seipenbusch
ParteQ GmbH & Universität Stuttgart

**Organization:** LUND UNIVERSITY, Department of Physics, Box 118, SE-221 00, LUND, SWEDEN

**Document name: DOCTORAL DISSERTATION** **Date of issue** 2023-12-01

**Author(s):** Markus Snellman **Sponsoring organization:**

**Title and subtitle:** Aerosol Synthesis and Characterization of Heterogeneous Bimetallic Nanoparticles

**Abstract:** As the proverbial noose tightens around humanity's resource spending, research is focused on utilizing materials to their fullest potential. Nanotechnology is the ultimate way to economize by splitting objects into smaller parts and dispersing the material properties over greater surface to volume ratios. Emerging quantum effects at the nanoscale present unique tweaking opportunities in applications. This thesis deals with creating and characterizing heterogeneous nanoparticles, including Janus and core-shell nanoparticles: segregated structures where the different parts having different properties allow for multiple functionalities within individual units. Heterogeneous nanoparticles that have already attracted interest in fields ranging from catalysis to biotechnology are typically made by chemical methods. Here, aerosol technology has been used to realize these nanostructures, as such physical synthesis hold advantages in improved purity of the product, and reduced waste from the process.

The two main approaches that have been developed in this work to create bimetallic heterogenous nanoparticles, surface segregation and condensational growth, both use spark ablation as the material source. From the optical emission in the electrical discharges, we use machine learning to determine the composition of bimetallic AuAg nanoparticles. Thermally induced surface segregation in CuAg agglomerates forming Janus and core-shell nanoparticles have been studied on- and off-line with aerosol metrology and electron microscopy. Compared to analogue works where the particles sit on a substrate, the aerosol phase is ideal to study surface segregation of "free" nanostructures. A more general route toward arbitrary metal-metal core-shell combinations is explored with condensational growth by thermal evaporation and photolysis. To understand the condensation inside a custom thermal evaporator designed in this work, a novel approach to measure the residence time distribution of aerosol nanoparticles is presented. Condensational growth of aerosol nanoparticles by photolysis of metal-organic precursors is a new route that can be carried out at room temperature. The process therefore allows for formation of core-shell particles of miscible materials and avoids thermophoretic losses of particles experienced in conventional thermal evaporation.

Combining on-line compositional monitoring with the unique, precursor-less pathways to create heterogeneous nanoparticles that aerosol technology enables, this thesis is a step toward more sustainable synthesis of tailored bimetallic nanostructures with applications in, for instance, catalysis, sensors, and electronics.

**Key words:** Nanoparticles, core-shell, Janus, aerosol technology

Classification system and/or index terms (if any) Supplementary bibliographical information

**Language:** English **ISSN and key title**:

**ISBN:** 978-91-8039-874-9 (print)

978-91-8039-875-6 (electronic)

Recipient's notes **Number of pages**: 101

Price Security classification



Signature Date 2023-10-20

# Aerosol Synthesis and Characterization of Heterogeneous Bimetallic Nanoparticles

Markus Snellman


LUND
UNIVERSITY

**Cover illustration front:** Artistic rendition of size distribution curves of gold nanoparticles growing by zinc condensation (white traces). Colored fills correspond to a condensational growth model.

**Cover illustration back:** photo of clouds over Kattegatt, near Hovs Hallar.



Division of Solid State Physics, Department of Physics

Faculty of Engineering, Lund University, Lund, Sweden

ISBN 978-91-8039-874-9 (print)

ISBN 978-91-8039-875-6 (electronic)

Printed in Sweden by Media-Tryck, Lund University

Lund 2023

*No piece of writing is ever finished. It's just due.*

- Bill Condon

# Table of Contents

# Abstract

As the proverbial noose tightens around humanity's resource spending, research is focused on utilizing materials to their fullest potential. Nanotechnology is the ultimate way to economize by splitting objects into smaller parts and dispersing the material properties over greater surface to volume ratios. Emerging quantum effects at the nanoscale present unique tweaking opportunities in applications. This thesis deals with creating and characterizing heterogeneous nanoparticles, including Janus and core-shell nanoparticles: segregated structures where the different parts having different properties allow for multiple functionalities within individual units. Heterogeneous nanoparticles that have already attracted interest in fields ranging from catalysis to biotechnology are typically made by chemical methods. Here, aerosol technology has been used to realize these nanostructures, as such physical synthesis hold advantages in improved purity of the product, and reduced waste from the process.

The two main approaches that have been developed in this work to create bimetallic heterogenous nanoparticles, surface segregation and condensational growth, both use spark ablation as the material source. From the optical emission in the electrical discharges, we use machine learning to determine the composition of bimetallic AuAg nanoparticles. Thermally induced surface segregation in CuAg agglomerates forming Janus and core-shell nanoparticles have been studied on- and off-line with aerosol metrology and electron microscopy. Compared to analogue works where the particles sit on a substrate, the aerosol phase is ideal to study surface segregation of "free" nanostructures. A more general route toward arbitrary metal-metal core-shell combinations is explored with condensational growth by thermal evaporation and photolysis. To understand the condensation inside a custom thermal evaporator designed in this work, a novel approach to measure the residence time distribution of aerosol nanoparticles is presented. Condensational growth of aerosol nanoparticles by photolysis of metal-organic precursors is a new route that can be carried out at room temperature. The process therefore allows for formation of core-shell particles of miscible materials and avoids thermophoretic losses of particles experienced in conventional thermal evaporation.

Combining on-line compositional monitoring with the unique, precursor-less pathways to create heterogeneous nanoparticles that aerosol technology enables, this thesis is a step toward more sustainable synthesis of tailored bimetallic nanostructures with applications in, for instance, catalysis, sensors, and electronics.

# Acknowledgements

This thesis was written with the help of many incredible people. Some of them are my supervisors, others are colleagues and family. Knut, thank you for offering me this position and for mentoring me throughout these five years (where did all the time go!?). You have always supported my (sometimes far-fetched) ideas. Thank you, Maria, for being "executive" co-supervisor and for leading the aerosol group. You always challenge us to think ahead and not jump to conclusions. Your and Knut's knowledge and contacts in the field of aerosol technology are very important to our group.

I want to thank Namsoon for your great work on our collaborations that led to two of the publications in this thesis. I wish you all success at the Division of mechanics. Martin, thank you for sharing your extensive knowledge on electron microscopy, and treatment of related spectroscopy methods. You have opened my eyes to the "data science" of spectroscopy. The little I know about X-ray techniques I attribute to Rasmus. Measurements at MAX IV has been a great experience and your expertise in synchrotron experiments is valuable to our research group.

Then, I want to give a shoutout to the rest of the aerosol group. Pau, Marie, Linnéa, and Mehran: thank you for great discussions, help and collaborations. A special thanks goes to Calle and Sara who showed me the ropes in the lab. It's been great to be able to go through the struggles with this thesis thing simultaneously with you, Sara. Thanks to Bengt for enabling us to do experimental work with your technical support and knowledge. Thomas, I'm looking forward to seeing the group progress experimentally with your knowledge. Speaking of technical (and other) support, thank you to Alfons, Andreas, Håkan, George, Emil, Peter, Natalia, Anders, Marcus, Marica and Alexandra for making research possible. A special thanks to Carina and Dan for their work in education and trusting me to teach in their courses. To the rest of my colleagues at solid state physics: thank you for making our division such a great place to work at!

I have been fortunate to do collaborations with people at other departments. Axel, thank you for our collaborations and letting me borrow your equipment. I have learned a lot from collaborations with Li and Per, and your novel work is always inspiring. I wish you the best of luck in China, Per. I want to thank Michael for giving my nanoparticles a purpose in crystal growth inside the environmental TEM, and congratulations on your success in Copenhagen.

Second last, I want to thank my friends, especially Internetriddarna, who have not only protected the realm of the internet but also my sanity. Finally, I want to thank Andrea, and our families – the most important people in my life – without whom I would not have been able to complete this thesis.

# Populärvetenskaplig sammanfattning

I dagens samhälle blir utveckling av nya tekniker och hushållande med befintliga resurser alltmer viktigt för en hållbar framtid. Nanoteknik, som handlar om att undersöka och använda material på nanoskalan, tacklar båda dessa problem. Nanoskalan är oerhört liten. En nanometer är en miljarddels meter, och 100 nanometer motsvarar ungefär *en tusendel* av vidden av ett hårstrå! Nanoteknik är på sätt och vis det ultimata sättet att hushålla med resurser. Genom att dela upp material i mindre och mindre bitar kan man sprida deras egenskaper över större ytor till samma volym. På nanoskalan ändras samtidigt i princip alla fysiska egenskaper, vilket man vill dra nytta av för att förbättra tekniker som katalys, batteriteknologi, medicin, solceller och lysdioder.

Hur hänger nanoteknik ihop med inplastade grönsaker, glappande kontakter, moln, och olja och vatten? Med dessa liknelser ska jag försöka beskriva den här avhandlingen, som handlar om att skapa och karaktärisera en speciell sorts nanopartiklar med aerosolteknologi. Nanopartiklar är helt enkelt objekt som är mindre än 100 nm och uppkommer naturligt i många sammanhang: när saker brinner bildas massvis med nanopartiklar, och i atmosfären spelar nanopartiklar en stor roll för moln- och regnbildning. Det dessa exempel har gemensamt är att nanopartiklarna flyter fritt i en gas, i dessa fall luften. Sådana "gas-partikel-blandningar" kallas aerosoler, och inom aerosolteknologi sysslar vi bland annat med att skapa och studera luftburna nanopartiklar. Det huvudsakliga instrumentet jag arbetar med för att skapa aerosoler är en gnistgenerator, och tekniken kallas gnistgenerering. Du har säkert sett det slå gnistor när du dragit ut kontakten på en dammsugare. Sådana gnisturladdningar kan levera en stor mängd energi på kort tid, tillräckligt för att slå ut atomer från metallkontakterna. På liknande vis slår gnistgeneratorn ut moln av atomer från två metallelektroder, och dessa moln kondenserar till nanopartiklar. Elektroderna fungerar som materialkällor för aerosolpartiklarna; genom att byta elektroderna kan man skapa nanopartiklar av nästan vilket material som helst!

I detta arbete ligger fokus på *segregerade* eller *heterogena* nanopartiklar. Två vanliga typer av segregerade nanopartiklar är "kärna-skalpartiklar" och "Januspartiklar", som visas i figur 1. Januspartiklar är partiklar med två delar av olika material och får sitt namn från den romerska guden Janus, som hade två ansikten. Kärna-skalpartiklar har, som namnet antyder, en kärna av ett material och ett eller fler skal av andra material. Man kan likna det vid inplastade grönsaker där plasten skyddar grönsaken från luften och förlänger dess hållbarhet. Eftersom nanopartiklar är så små upptar ytan en stor andel av volymen, och därför kan ett skyddande skal behövas om kärnan är känslig för luften. Omvänt kan man behöva skydda omgivningen från giftiga material. Med ett skyddande skal kan

man göra vissa nanopartiklar som kroppen inte tål biokompatibla, vilket används för att utveckla ny medicin.

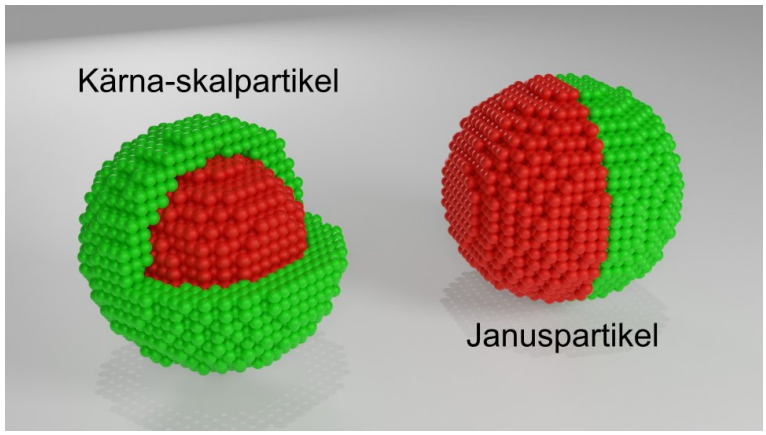


**Figur 1.**
En kärna-skalpartikel har en kärna av ett material och ett skal av ett annat. Januspartikeln har två distinkta "ansikten" av olika material.

Generellt kan man säga att segregerade nanopartiklar är uppdelade i två eller fler distinkta material som kan ha olika egenskaper och fylla olika funktioner i ett och samma paket. I avhandlingen har två principiella metoder utvecklats för att skapa sådana nanopartiklar i aerosolfasen genom att modifiera partiklar från gnistgenerering. Den första metoden kallas ytsegregering, och påminner om hur olja separerar sig från vatten, som i figur 2. Med gnistgenerering skapar vi först nanopartiklar av ämnen som inte vill blanda sig, i detta fall koppar och silver. Genom att värma upp de luftburna partiklarna med en sintringsugn visar vi på att man kan skapa Janus- och kärna-skalpartiklar genom att variera temperaturen i ugnen. Ytsegregering är fördelaktigt för att det är en enkel metod, men den fungerar bara för vissa materialkombinationer.

Vill man skapa mer godtyckliga materialkombinationer kan man växa skal genom att kondensera en ånga av ett material på redan existerande partiklar, vilket är den andra metoden som utvecklats. Processen är kan liknas vid hur moln bildas i atmosfären, när vattenånga kondenserar på små partiklar och växer till större vattendroppar (som molnen i figur 2). I vårt system använder vi höga temperaturer för att förånga ett material; när det kyls i närvaron av partiklar kondenserar det och bildar ett skal på partiklarna. Ett annat sätt att kondensera skal på aerosolpartiklar är att blanda en gas av ljuskänsliga molekyler med partiklarna, och "trigga" kondensering med ljus. De speciella molekylerna innehåller kolföreningar bundna till metallatomer. När de belyses med UV-ljus klyvs bindningarna till kolföreningarna vilket frigör metallatomerna som

kan kondensera på partiklarna vid rumstemperatur. Oavsett metod kan vi optimera och förstå den bättre genom att mäta hur partiklarna växer i luften med smarta instrument, något som är en unik fördel i aerosolteknologi. Framsidan på denna avhandling visar data från sådana mätningar, mer specifikt hur en guld-aerosol växer av zink som kondenserar på den.

**Figur 2.**
Likt hur olja och vatten separerar i glaset till vänster kan man skapa segregerade nanopartiklar av vissa material som inte vill blanda sig. Ett annat sätt är att kondensera ångan av ett material på partiklar av ett annat material, på samma vis som molnen i bilden till höger bildats i atmosfären när vattenånga kondenserar på små partiklar.

I den här avhandlingen beskriver jag hur vi utvecklat ovanstående metoder i detalj, och deras för- och nackdelar. Detta arbete utgör en vidareutveckling och specialisering av tidigare metoder inom aerosolteknologi för att skapa skräddarsydda nanopartiklar, med fokus på segregerade nanostrukturer som kärna-skalpartiklar. Vi har redan testat att använda sådana strukturer för halvledarväxt, vilket är ett stort fält med många användningsområden. Förhoppningen är att metodiken beskriven här ska kunna byggas vidare på, och att dessa strukturer ska kunna testas i applikationer såsom katalys, och materialteknologi. Kanske kommer avhandlingen inspirera framtida doktoranders forskning.

# Popular science summary

Nowadays, the development of new technologies and conservation of present resources become increasingly important for a sustainable future. Nanotechnology, which is the research and use of nanoscale materials, combats both issues. The nanoscale is incredibly small. A nanometer is a billionth of a meter, and 100 nanometers is about a thousandth of the width of a human hair! Nanotechnology is in a sense the ultimate way of economizing with resources. By dividing materials into smaller and smaller parts, we can spread their properties over larger surfaces to the same volume. On the nanoscale, virtually all physical properties change, which we want to take advantage of to improve technologies like catalysis, batteries, medicine, solar cells and light emitting diodes.

How does nanotechnology relate to plastic wrapped vegetables, loose electric connections, clouds, and oil and water? Using these as metaphors, I will describe this thesis, which is about creating and characterizing a certain kind of nanoparticles with aerosol technology. Nanoparticles are simply objects smaller than 100 nm and emerge naturally in many occasions: when things burn, a large amount of nanoparticles form, and nanoparticles play an important role in the atmosphere for cloud and rain formation. What these examples have in common is that the nanoparticles are floating freely in a gas, in this case the air. Such "gas-particle-mixtures" are known as aerosols, and aerosol technology is about creating and studying airborne nanoparticles. The main instrument I work with to create aerosols is a spark discharge generator, and the method is often called spark ablation. You have probably seen sparks flying when you pull the plug on a vacuum cleaner. These spark discharges can deliver a large amount of energy in a short amount of time, enough to knock out atoms from the metal contacts. In a similar way, the spark discharge generator knocks out clouds of atoms from two metal electrodes, and these vapor clouds condense to nanoparticles. The electrodes serve as material sources for the aerosol particles; by switching electrodes, you can make nanoparticles out of almost any material!

The focal point of this work has been *segregated* or *heterogeneous* nanoparticles. Two common types of segregated nanoparticles are "core-shell" particles and "Janus" particles, shown in figure 1. Janus particles are particles with two parts of different materials, and get their name from the Roman god Janus, who had two faces. Core-shell particles have, as their name implies, a core of one material and one or more shells of other materials. One can compare such particles to vegetables wrapped in plastic, where the plastic protects the vegetable from the air and prolongs the shelf life. Because nanoparticles are so small, the surface occupies a large fraction of their volume, and a protecting shell can be needed for air sensitive materials. On the flip side, we may need

to protect the environment from poisonous materials. With a protective shell, we can make certain nanoparticles biocompatible, which is a strategy used to create new medicine.

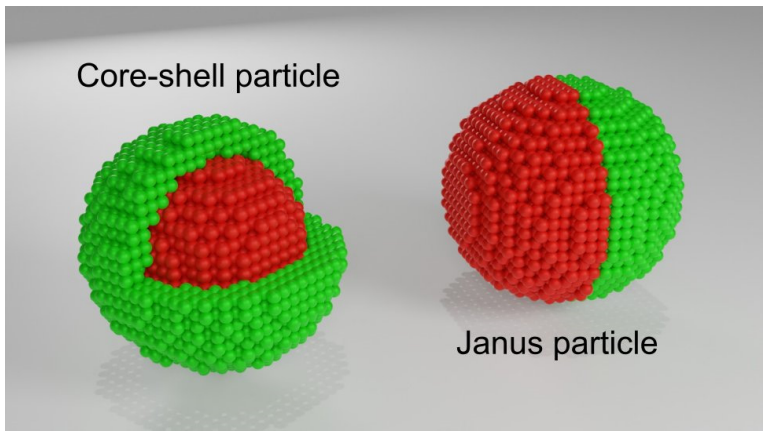


**Figure 1.**
A core-shell particle has a core of one material and a shell of another material. The Janus particle has two distinct "faces" of different materials.

Generally speaking, segregated nanoparticles are split into two or more distinct materials that can have different properties and implement different functionalities in the same structure. In this thesis, two principal methods have been developed to create such nanoparticles in the aerosol phase by modifying particles made with spark ablation. The first method is called surface segregation and has similarities to how oil and water separate, shown in figure 2. With spark ablation, we first create nanoparticles of immiscible materials, in this case copper and silver. By heating the airborne particles with a sintering furnace we show that we can create both Janus and core-shell particles by varying the furnace temperature. Surface segregation is advantageous because it is simple, but it only works for certain material combinations.

If you want to have core-shell particles of arbitrary material combinations, you can grow a shell by condensing a vapor of one material onto core particles of another material, which is the second method developed here. This process is analogous to how clouds form in the atmosphere, when water vapor condenses on small particles and grow to large droplets (like the clouds in figure 2). In our system we use high temperatures to evaporate a material; when it cools in the presence of an aerosol it condenses and forms a shell on the particles. Another approach for condensing a shell onto aerosol particles is to mix a gas of light sensitive molecules with the particles, and to "trigger" the condensation with light. The special molecules contain carbon compounds bound to

metal atoms. Upon UV illumination, the carbon-metal bonds break, freeing the metal atoms that can condense on aerosol particles at room temperature. Regardless of method, we can optimize and understand it better by measuring how the particles grow in the gas with smart instruments, something that is a unique benefit to aerosol technology. The cover of this thesis shows data from such measurements, more specifically how a gold aerosol grows by zinc condensing on the particles.

**Figure 2.**
Similar to how water and oil separate in the glas on the left, we can create segregated nanostructures with certain materials that don't want to mix. Another way is to condense the vapor of one material onto core particles of another material, like how the clouds in the picture on the right form by water vapor condensation on small particles in the atmosphere.

In this thesis I describe how we have developed these methods in detail, and their pros and cons. This work presents a further development and specialization of previous methods in aerosol technology to create custom nanoparticles, focusing on segregated nanostructures including core-shell particles. We have already explored using these structures for semiconductor growth, which is a large field with many applications. My hopes are that the methods described here can be further developed, and that the structures they can create can be tested and optimized for applications including catalysis and materials technology. Perhaps, this thesis will be an inspiration for the work of future PhD students.

# List of Papers

Results discussed in this thesis are partly based on the following articles, referred to in the text by their capital Roman numerals:

*Paper I*

**On-line compositional measurements of AuAg aerosol nanoparticles generated by spark ablation using optical emission spectroscopy**

**Snellman, M.**, Samuelsson, P., Eriksson, A., Li, Z. and Deppert, K.

*Journal of Aerosol Science*, **2022**, 165, 106041.

This paper develops a simple and cost-effective method to determine the composition of AuAg nanoparticles from optical emission spectroscopy on-line. I conceived of the project, collected and analyzed the data and wrote the manuscript.

*Paper II*

**Continuous gas-phase synthesis of core–shell nanoparticles via surface segregation**

**Snellman, M.**, Eom, N., Ek, M., Messing, M. E. and Deppert, K.

*Nanoscale Advances*, **2021**, 3 (11), 3041 – 3052.

The paper presents an aerosol synthesis of segregated core-shell and Janus nanoparticles via heat induced surface segregation. Me and my co-supervisor N. Eom conceived the project. I collected and analyzed the experimental data and co-wrote the manuscript with N. Eom.

*Paper III*

**A thermal evaporator for aerosol core-shell nanoparticle synthesis**

**Snellman, M.**, Eom, N., Messing, M. E. and Deppert, K.

*Journal of Aerosol Science,* **2024,** 175, 106276.

This paper deals with the development of a thermal evaporator to coat aerosol nanoparticles with a Zn shell. Me, N. Eom and K. Deppert conceived the idea. I collected and analyzed experimental data and wrote the manuscript.

The following articles are not included in the thesis:

*Paper iv*

**Interface Dynamics in Ag-$Cu_3P$ Nanoparticle Heterostructures**

Seifner, M. S., **Snellman, M.**, Makgae, O. A., Kumar, K., Jacobsson, D., Ek, M., Deppert, K., Messing, M. E. and Dick, K. A.

*Journal of the American Chemical Society,* **2021**, 144 (1), 248 – 258.

*Paper v*

**Airborne Gold Nanoparticle Detection Using Photoluminescence Excited with a Continuous Wave Laser**

Samuelsson, P., **Snellman, M.**, Magnusson, M. H., Deppert, K., Aldén, M. and Li, Z.

*Applied Spectroscopy,* **2021**, 75 (11), 1402 – 1409.

*Paper vi*

**Insigts into the Synthesis Mechanisms of Ag-$Cu_3P$-GaP Multicomponent Nanoparticles**

Seifner, M. S., Hu, T., **Snellman, M.**, Jacobsson, D., Deppert, K., Messing, M. E. and Dick, K. A.

*ACS Nano,* **2023**, 17 (8), 7674 – 7684.

*Paper vii*

**Direct Observation of Liquid-Solid Two-Phase Seed Particle-Assisted Kinking in GaP Nanowire Growth**

Hu, T., Seifner, M. S., **Snellman, M.**, Jacobsson, D., Sedrpooshan, M., Ternero, P., Messing, M. E. and Dick, K. A.

*Small Structures,* **2023**, 2300011.

*Paper viii*

**The Effect of Electrode Composition on Bimetallic AgAu Nanoparticles Produced by Spark Ablation**

Jönsson, L., **Snellman, M.**, Eriksson, A., Kåredal, M., Preobrajenski, A., Generalov, A., Wallenberg, L. R., Blomberg, S., Kohut, A., Hartman, L. and Messing, M. E.

*In manuscript.*

*Paper ix*

**Combustion of micron-sized Al-Mg alloy wires in hot H2O/O2/N2 flows**

Can, R., Wu, Z., Stiti, M., **Snellman, M.**, Qiu, Y., Subas, A. A., Berrocal, E., Aldén, M. and Li, Z.

*Fuel,* **2024**, 357, Part A, 129719.

# Abbreviations

| | |
|---|---|
| At. % | Atomic percent |
| BSE | Backscattered electrons |
| DMA | Differential mobility analyzer |
| EDX | Energy dispersive X-ray spectroscopy |
| EM | Electron microscopy |
| EMG | Exponentially modified Gaussian |
| ESP | Electrostatic precipitator |
| GMD | Geometric mean diameter |
| GSD | Geometric standard deviation |
| HEPA | High efficiency particulate air (filter) |
| HV | High voltage |
| Kn | Knudsen number |
| LASSO | Least absolute shrinkage and selection operator |
| LIBS | Laser induced breakdown spectroscopy |
| MAE | Mean absolute error |
| MD | Molecular dynamics |
| M/HAADF | Medium/high angle annular dark field |
| MFP | Mean free path |
| MOCVD | Metal-organic chemical vapor deposition |
| NMF | Non-negative matrix factorization |
| NP | Nanoparticle |
| OES | Optical emission spectroscopy |
| PCA | Principal component analysis |
| $R^2$ | Coefficient of determination |
| Re | Reynolds number |
| RLC | Resistance inductance capacitance |

| | |
|---|---|
| RMSE | Root mean squared error |
| RTD | Residence time distribution |
| SE | Secondary electrons |
| SEM | Scanning electron microscope/microscopy |
| SIBS | Spark induced breakdown spectroscopy |
| (S)TEM | (Scanning) Transmission electron microscope/microscopy |
| TMIn | Trimethylindium |
| XRF | X-ray fluorescence spectroscopy |
| Z | Atomic number |

# 1 Introduction

This thesis describes the aerosol synthesis and characterization of bimetallic nanoparticles (NPs) with a focus on heterogeneous structures including core-shell and Janus NPs. NPs come in many shapes and forms, and they are often defined as structures with all physical dimensions in a range of 1 nm to 100 nm. Materials with these dimensions have found a big interest in research and applications as physical properties like magnetic properties, optical properties and mechanical properties diverge more from the bulk state with decreasing particle size. Nanoscale carbon, for instance, provides car tires strength and abrasion resistance. Sunscreens take advantage of reduced optical scattering in titania and zinc oxide NPs, leading to improved transparency while maintaining excellent UV absorption properties [1]. Composite NPs, consisting of more than one material or element, may exploit both size effects and individual properties of the constitute materials, offering an extended range of tailored applications. A good example is how the optical absorption can be precisely tuned by composition in alloyed AuAg NPs [2], which can be used in optical detection of molecules [3]. Bimetallic NPs are one of the most elementary types of composite NPs and have been the focus of study in this thesis.

Perhaps most notably, the surface to volume ratio increases with decreasing particle size, with profound impacts for nanomaterials as interactions between NPs and the outside world often occur across surfaces. In ambient conditions, most metals and semiconductors form passivating surface oxides. On the nanoscale, such oxides may constitute a significant portion of the volume. This is the simplest example of a core-shell NP: a concentric (oxide) shell encapsulating a (metal) core. For instance, Fe NPs readily turn into Fe-$Fe_xO_y$ core-shell particles in air. The oxide may change the overall physical properties, and partly protects the metallic core from further oxidation [4, 5]. Dispersing a catalytic material over the surface of a core NP of another material is a way to take advantage of the high surface to volume ratio, while keeping the often expensive catalytic material usage to a minimum [6, 7].

The high specific surface area of NPs is a double-edged sword. Small Fe NPs are pyrophoric and may completely oxidize in air [8]. Passivating the surface to retain particle “bulk” properties is a common goal of core-shell NPs. Conversely, it can be

desirable to protect the outside environment from the core material with a shielding shell. Coating Ag NPs with Au is a way to optimize optical detection of certain biomarkers, and simultaneously making the particles biocompatible [9, 10]. Another use case of the core-shell morphology is to combine or enhance physical properties, such as optical and magnetic properties, of the present materials [11, 12]. A catalytic shell material covering a magnetic core NP can retain the magnetic properties of the core and enables magnetic separation and recyclability in heterogeneous catalysis [13, 14].

Core-shell NPs is one example of heterogenous nanostructures. Another example is the Janus structure where the two materials divide the particle in two distinct "faces". The shell in core-shell particles, and the faces in Janus NPs can arrange in various configurations, with some examples shown in figure 1.1. Like the core-shell structure, the phases in Janus particles may implement multiple distinct functionalities in the same structure [15]. The nanoscale interfaces between materials with different properties in Janus NPs have found particular interest in photocatalysis, where a photocatalytic material, often some semiconducting metal oxide, is aided by a plasmonically active material like Au [16] to improve charge carrier separation in the semiconductor [17].

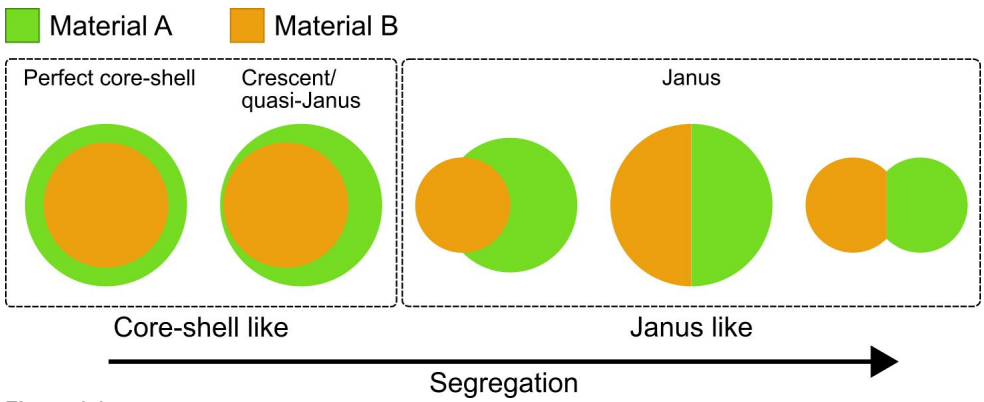


**Figure 1.1.**
Schematic drawing of cross-sections of spherical, heterogeneous nanoparticles. Common chemical orderings include core-shell and Janus morphologies. Core-shell structures are characterized by a shell of one material wrapping around another material. Janus structures are divided into two distinct "faces" of two different materials.

In this thesis, aerosol technology has been the methodology to create NPs. Although less common than chemical synthesis, physical routes, including some methods employed in aerosol technology, hold certain benefits. Physical synthesis can be more efficient as fewer processing steps often are required. Waste and byproducts obtained in chemical processes can in many implementations be reduced or completely avoided,

resulting in potentially more environmentally friendly and purer products [18]. Like many physical methods, however, aerosol synthesis usually results in broad NP size distributions from particle-particle interactions [1], and size-selection is often required to obtain narrow size distributions, which is desirable in many cases. Thankfully, the continuous nature of aerosol technology lends itself well for in situ studies and actuation, and a suite of tools exist to monitor and control the aerosol to obtain the desired product.

The aerosol synthesis method used in this thesis to produce NPs is spark ablation, where electrical discharges ablate material from the surface of pairs of electrodes. A vast range of different NPs can be obtained from the ablated material by selecting appropriate electrode materials, which makes the method a versatile starting point for creating nanostructures. Spark ablation is, however, limited by the stochastic nature of particles nucleating and coagulating to larger structures. There is a need for techniques to modify and further customize the aerosol NPs. A significant goal of the thesis is to characterize new methods to continuously modify spark ablation made NPs in-flight to realize well-defined bimetallic heterostructures.

Despite the relative technological simplicity of spark ablation, there are several processes acting at different timescales that may be measured and tuned by changing process parameters to optimize and understand the NP synthesis. In bimetallic NP systems, composition is one of the most important properties. Progress in compositional control of spark synthesized NPs would benefit from characterization that can be used to monitor the generation process. Therefore, another topic explored in this thesis is the implementation of a simple, cost-effective technique to characterize the stoichiometry of NPs as they are produced by spark ablation. Combining such compositional measurements with the subsequent processing methods to obtain tailored heterostructures will hopefully further aerosol technology as a viable platform for new, multifunctional materials.

## 1.1 Outline

One feature of spark ablation is the optical emission from the plasma created during the discharges. This emission is characteristic for the gas as well as the electrode material species present in the plasma. We can directly relate the optical emission to the composition of the produced NPs, which is promising as an on-line process monitoring tool for composite NPs. This is the topic of **Paper I**, where machine learning regression models were built using optical spectra emitted during spark ablation of AuAg NPs to determine the stoichiometry during synthesis.

Going beyond composition, it is useful to be able to measure the size of the produced aerosol, and to size-select particles within a narrow size range. Such aerosol manipulation is central in aerosol technology and for the experimental setups used in the works that compose this thesis. Together with spark ablation, the governing aerosol physics and techniques used in the experimental setups will be described in **Chapter 2**.

There are essentially two approaches to create segregated nanostructures in aerosol technology that have been developed in this thesis. The first approach explored is to heat treat complex structures in-flight to induce segregation between immiscible components. The process, known as surface segregation, is exploited to form both core-shell and Janus NPs from CuAg agglomerates in **Paper II**. These results, together with the general process of sintering aerosol particles is described in **Chapter 3**. While surface segregation is appealingly simple, it does not work for all materials. We need additional processing steps to obtain heterogeneous NPs of more general material combinations.

The most intuitive sequential synthesis approach is to start with an aerosol of core NPs and condense another material onto them, similar to how water droplets form around small particles in the atmosphere [19, 20]. Condensational growth of heterogeneous NPs has been studied with two distinct approaches: by thermal and photolytic condensation. Thermal condensation, which is the central methodology of **Paper III**, uses temperature gradients to condense the vapor of an evaporated shell material onto aerosol core particles. In photolytic condensation, photons are used to decompose light-sensitive metal-organic precursors in a process called photolysis. Combined with an aerosol, photolysis leads to the condensation of the metal on core NPs even at room temperature. Thermal and photolytic condensation are the topics of **Chapter 4** in the thesis.

Both surface segregation and condensation present unique pathways to realize heterogeneous NPs in the aerosol phase. Combined with novel approaches to monitor the stoichiometry of bimetallic NPs on-line, aerosol technology is poised to have a unique position in the synthesis of advanced materials with applications in areas including catalysis, sensors, and fuel cells. A summary and an outlook on the synthesis and characterization of these NPs will be presented in **Chapter 5**, including examples of uses for bimetallic particles in semiconductor growth.

# 2 Aerosol technology and analytical methods

The methodological platform used in this thesis is aerosol technology, which studies synthesis, properties, characterization, and applications of aerosol particles. Being a subfield of the broader discipline of aerosol science, which deals with as important topics as air pollution and infection spreading, aerosol technology shares the theories of aerosol dynamics and many tools to investigate and actuate aerosols. Historically, natural and anthropogenic aerosols have been the main focus in aerosol technology. With the rise of nanotechnology in the last decades, aerosol technology has found increased popularity in fabrication and characterization of engineered NPs.

This chapter explains the physics and operations of the experimental methods used to create and characterize aerosol NPs, both directly in the aerosol phase (on-line) and deposited on substrates (off-line). After a brief introduction to aerosol physics, the most important aerosol characterization methods, size-selection and counting, are described. These allow us to study the evolution of size of the particulate output of aerosol generators, like spark ablation. Important process parameters and observables in spark ablation are discussed to obtain desired NPs. One useful observable is the optical emission from the electrical discharges. Results from real-time process monitoring of aerosol particle composition using the optical emission is therefore presented before we describe the NP formation process. Finally, aerosol deposition and some powerful off-line methods for characterizing nanostructures are described.

## 2.1 Basic aerosol dynamics

An aerosol is a suspension of liquid or solid particles in a gas. The suspended particles can be in a wide size range of diameters, from ca. 1 nm to several microns. Since NPs can have irregular shapes, one must be careful when specifying what diameter means. Here, we will for simplicity assume that the particles are spherical, and so we will use their geometrical diameter. Because aerosol particles are so small, they can stay

suspended for significant amounts of time, which we can estimate by balancing the principal forces involved in free fall: gravity and drag [19]. The force a spherical aerosol particle of diameter $d_p$ and density $\rho_p$ experiences due to gravity is

$$F_g = \frac{\pi}{6} d_p^3 \rho_p g \tag{2.1}$$

The opposing drag force the particle experiences as it falls through the medium of viscosity $\eta$ at some velocity $v$ with respect to the gas medium is described by Stoke's law:

$$|F_d| = \frac{3\pi\eta d_p v}{C_c} \tag{2.2}$$

$$C_c = 1 + \frac{\lambda}{d_p}\left[2.34 + 1.05\exp\left(-0.39\,\frac{d_p}{\lambda}\right)\right] \tag{2.3}$$

By balancing the gravitational and drag forces, we can solve for a terminal settling velocity

$$v_{\mathrm{TS}} = \frac{\rho_p d_p^2 g C_c}{18\eta} \tag{2.4}$$

Equations (2.2) and (2.4) are valid for aerosol particles when the Reynolds number (Re) is smaller than 1.0, which is often the case for aerosol NPs. Re is a dimensionless number that indicates if a fluid flow (here: the gas) around some object (like a particle or inside a tube) is laminar or turbulent. A laminar flow occurs at low Re < 1.0 around particles, meaning that gas streamlines flowing around the particle are "smooth". Re is proportional to the ratio of inertial forces to viscous forces acting on fluid elements in the gas, and is calculated using the gas density and viscosity, and particle diameter, as well as the relative velocity between gas and particle. Using the terminal settling velocity, we can estimate that it would take a 10 µm spherical particle with unit density ca. 5 minutes to fall one meter, whereas a similar 100 nm particle would stay airborne for more than ten days!

The Cunningham slip correction factor $C_c$ (equation (2.3)) accounts for the non-zero gas velocity at the surface of particles smaller than ca. 100 nm. This is one example how NPs behave differently from macroscopic particles: in the aerosol phase, NPs experience larger settling velocities from decreased drag as gas collisions become more discrete with decreasing particle size. In equation (2.3), $\lambda$ is the mean free path (MFP) of gas molecules, *i.e.*, the average distance between molecule-molecule collisions. The ratio between MFP and particle diameter is characterized by the Knudsen number, Kn =

$2\lambda/d_p$, which is a figure useful to describe of heat, mass and momentum transfer between particle and gas for different particle sizes [21].

With the simple gravitational settling calculation above, it seems we have plenty of time to study NPs while they are still airborne. However, NPs undergo rapid Brownian motion from collisions with gas molecules, which is described by their diffusion coefficient given by the Stokes-Einstein relation [19]:

$$D = \frac{k_B T C_c}{3\pi\eta d_p} \tag{2.5}$$

Apart from particle properties ($C_c, d$) and gas viscosity ($\eta$), equation (2.5) contains the Boltzmann constant $k_B$ and gas temperature $T$. If we consider the root-mean-square net displacement $x_{rms}$ due to Brownian motion during some time $t$, $x_{rms} = \sqrt{2Dt}$, we find that the 100 nm particle will be, on average, displaced only about 40 microns in one second. This displacement is in many cases insignificant, but the situation is worse for smaller NPs. A 10 nm particle being transported in a 6 mm tube (4.8 mm inner diameter) will be lost from the aerosol by depositing on the tube sidewall within less than a minute. Dealing with small aerosol NPs in aerosol technology is, in some sense, a race against time.

## 2.2 Aerosol characterization

The rapid diffusion of small particles in a gas is a reason not only for particle losses to surfaces, but also the temporal evolution of their sizes by coagulation that tend to result in broad size distributions. If we want NPs within a well-defined, narrow size range, we need to either limit the coagulation time or apply size-selection. Combining size-selection with particle concentration measurements allows us to measure the aerosol size distribution, which is a powerful on-line method in aerosol technology commonly implemented with a differential mobility analyzer (DMA) and an electrometer or a condensation nuclei counter (CPC).

### 2.2.1 Charging

The DMA works based on charged particle motion in an electric field. For this to work, the particles need to be charged. In this thesis, radioactive chargers have been used to charge the aerosol to a known charge distribution. They consist of a chamber with a radioactive substrate that ionizes the gas molecules, who in turn transfer charge by

collisions with aerosol particles. Depending on the charge of the particle and the ion, some particles become positive, negative, or neutral.

Due to the dynamics between species with the same or opposite charge, aerosol NPs obtain a small average charge. In fact, most particles smaller than 50 nm will be neutral after passing through these bipolar chargers, which is why they are also called neutralizers [19]. After enough time inside the neutralizer, typically a couple of seconds, the particles will obtain an equilibrium Boltzmann charge distribution that can be approximated by equation (2.6) [19]:

$$f_n = \frac{\exp\left(-\frac{1}{4\pi\epsilon_0} n^2 e^2 / d_p k_B T\right)}{\sum_{n=-\infty}^{\infty} \exp\left(-\frac{1}{4\pi\epsilon_0} n^2 e^2 / d_p k_B T\right)} \tag{2.6}$$

$f_n$ describes the probability of finding a particle of diameter $d_p$ carrying $n$ charges. In the equation, $e$ is the elementary charge, and $\epsilon_0$ is the vacuum permittivity. A more accurate approximation that takes into account the different mobilities of negatively and positively charged ions is given in Ref. [22].

### 2.2.2 Size-selection

The force charged particles experience due to an electric field $E$, $F_e = neE$, can, similar to the gravitational settling case, be balanced with the drag force to extract a terminal velocity. From this, we define the particle electrical mobility $Z_p$ (for Re < 1.0) as [19]

$$Z_p = \frac{v_T}{E} = \frac{neC_C}{3\pi\eta d_p} \tag{2.7}$$

Inside the DMA, schematically depicted in figure 2.1, an electric field $E$ is set with a voltage $U$ between two concentric cylinders of radii $r_{\text{inner}}$ and $r_{\text{outer}}$. An additional sheath flow, $Q_{\text{sheath}}$, removes uncharged particles, and oppositely charged particles. The sheath flow, voltage, and the dimensions of the DMA, including the cylinder length $L$, determine the mean electrical mobility of particles exiting the DMA [23]:

$$Z_p^* = Q_{\text{sheath}} \ln\left(\frac{r_{\text{outer}}}{r_{\text{inner}}}\right) / 2\pi LU \tag{2.8}$$

Equation (2.8) holds for a balanced sheath flow, where the sheath in and out flows are the same. From equations (2.7) and (2.8) we find we can size-select particles of diameter $d_p \propto neC_C U$, *i.e.,* smaller particles can be selected with a lower voltage and larger particles with a higher voltage. Particles with higher mobilities will deposit inside the

DMA and be lost from the aerosol. Particles with smaller mobilities exit with uncharged and low mobility oppositely charged particles through the sheath flow outlet. Because NPs can have irregular shapes, such as agglomerates, we use the concept of (electrical) mobility diameter to describe their size. The mobility diameter, $d_m$, is the diameter of a sphere with the same electrical mobility as the NP in question [21]. For spherical NPs, the geometrical and mobility diameters are equal, which is one reason spherical NPs are convenient to work with in aerosol technology.

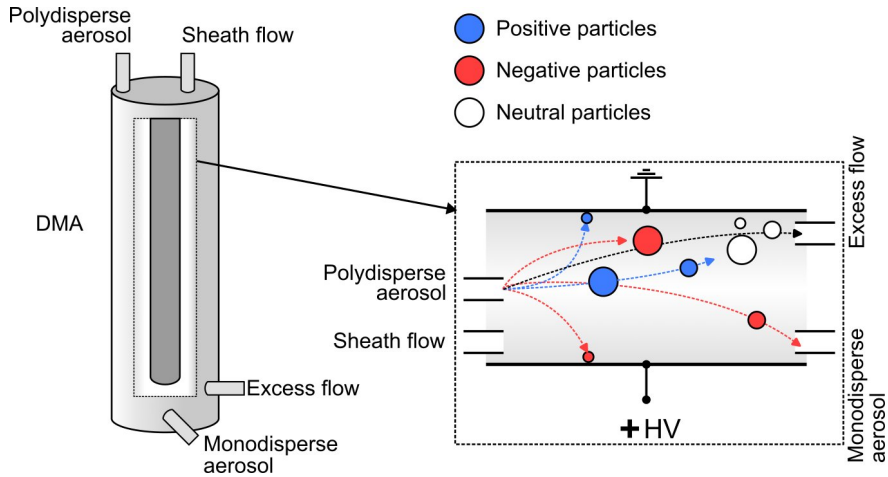


**Figure 2.1.**
Schematic drawing of a DMA showing size-selection of charged aerosol particles. Only particles within a narrow mobility diameter range will exit the DMA, allowing us to size-select monodisperse subpopulations of a polydisperse aerosol.

### 2.2.3 Counting

NPs that exit the DMA are ideally monodisperse and singly charged. In that case, we can measure the concentration of particles through their charge. The aerosol electrometer (figure 2.2) measures the current induced from the charged aerosol flow and converts it to a particle concentration. Alternatively, a condensation nuclei counter (CPC) can be used (figure 2.2). The CPC condenses a liquid (often water or butanol) on the aerosol NPs such that they grow to micrometer sizes and can be detected by optical scattering in a laser. CPCs can also detect uncharged particles, but the total concentration of particles it can detect is usually much lower compared to an electrometer. By combining the DMA size-selection with a CPC or electrometer detector, we can measure the size distribution of the aerosol on-line. This is a crucial technique in aerosol science to measure dynamics like coagulation, growth, and evaporation directly in the aerosol phase. Observing and analyzing such changes in the

aerosol size distribution is central in this thesis and will be discussed in more detail later. Since the particles are size-selected with a DMA, the colloquial concept of size distribution in this thesis always refers to the mobility diameter size distribution of the aerosol.

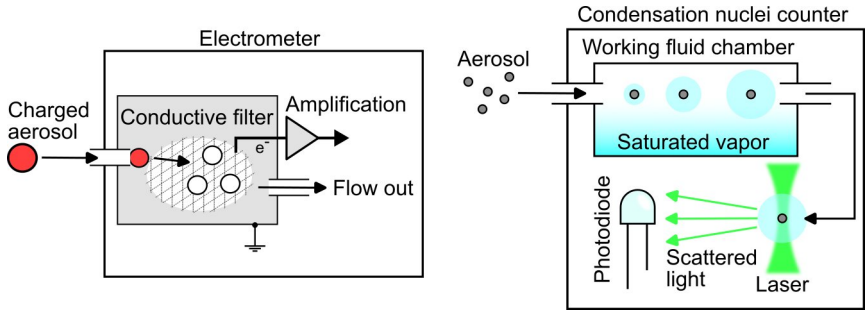


**Figure 2.2.**
Schematic drawings of an electrometer and a CPC that are used to measure aerosol nanoparticle concentrations. The electrometer measures the current induced by charged nanoparticles depositing on a conductive filter. The CPC measures the optical scattering from nanoparticles grown to micrometer size with a working fluid, typically some alcohol or water. Combined with size-selection with a DMA, these counters can be used to measure (mobility diameter) size distributions of an aerosol.

## 2.3 Aerosol generation: Spark ablation

Spark ablation was first used in 1986 and 1988 [24, 25] to produce carbonaceous aerosols. Thanks to the relatively simple setup, it has since found many uses in producing a suite of NPs including monometallic [26-28], bi- and multimetallic [26, 27, 29-31], oxide [32, 33] and semiconducting [34-36] NPs.

Figure 2.3 below shows a schematic of a common spark ablation setup. A high voltage, high power supply applies a charging current $I_{ch}$ to charge a capacitor bank with some capacitance $C$ shunted to one or more pairs of electrodes. The most common electrode setup is the rod-to-rod configuration, where the biased electrode usually is the anode, and the grounded electrode is the cathode. When the voltage across the capacitors reaches the breakdown voltage $V_b$ of the gas between the electrodes, a conductive path is formed through a plasma in the electrode gap, across which the capacitors discharge their energy, after which the charging cycle is repeated.

The discharge energy ablates atoms from the electrode surfaces and leads to emission of sound and light from the expanding plasma. The optical emissions can provide information about the spark ablation process and, importantly, the particles that subsequently form through nucleation, coalescence and coagulation as the plasma

cools. By tuning the process parameters, we control the number of NPs produced and their size, and to some extent their composition. A wide distribution of NP sizes ranging from atomic clusters [37] to 100 nm agglomerates are attainable, with composition mainly determined by the choice of electrode materials.

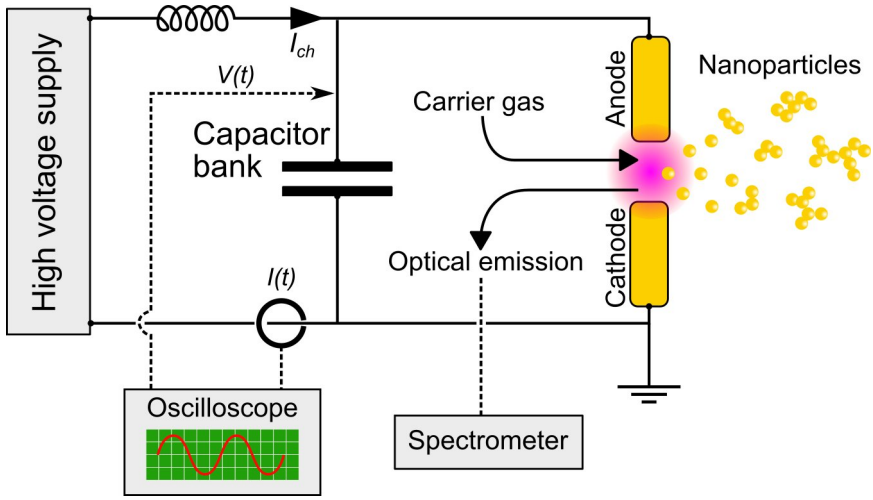


**Figure 2.3.**
Schematic of the spark ablation setup and equipment to measure observables like discharge current and voltage, and optical emission. The high voltage supply charges a capacitor bank with a charging current. When the capacitors discharge, material ablated from the shunted electrodes form nanoparticles, and the discharge voltage and current can be measured with an oscilloscope. The optical emission from the discharge plasma can be measured with a spectrometer.

### 2.3.1 Process parameters and observables

Some the most important process parameters in spark ablation are the capacitance, charging current, discharge or breakdown voltage, $V_\mathrm{b}$, and aerosol carrier gas flow rate, $Q_\mathrm{a}$. These parameters are in many ways intertwined. By choosing some capacitance, we change both the (maximum) energy in each discharge, $E = 0.5CV_\mathrm{b}^2$ which originates from the energy stored in the capacitors, and the discharge frequency, $f = I_\mathrm{ch} / CV_\mathrm{b}$. A higher capacitance entails a higher energy per discharge, which leads to more material output per spark. On the other hand, increasing the capacitance decreases the discharge frequency, which results in a lower material output rate. Further, an increasing discharge frequency tends lower the discharge voltage, due to a shorter time for the carrier gas to flush out ions from the previous discharge [38]. The carrier gas flow rate also controls the dilution of the aerosol. A higher flow, and hence dilution, leads to smaller particles as the coagulation is slowed down, which will be discussed more later.

Typical values for capacitance, charging current are in the order of 10 nF and 10 mA. In "free running" spark ablation, where discharges are triggered by a breakdown of the carrier gas and not externally triggered, the breakdown voltage is a property of the carrier gas and pressure [39], and is practically tuned by setting the electrode distance for a fixed carrier gas composition and pressure. In this case, breakdown voltage and discharge voltage are typically used interchangeably. For most carrier gases, the breakdown voltage is about 1 – 10 kV for electrode separations on the order of a few mm. With these operating values for capacitance, charging current and breakdown voltage, we find that discharge energy and frequency typically lie around 100 mJ and 100 Hz. More advanced setups have been used to increase discharge frequency and energy by decoupling the capacitor charging and discharging cycles, thereby achieving higher discharge voltages than the carrier gas permits [40].

We can understand and possibly control spark ablation by measuring observables like discharge current and voltage, and the optical emission from the plasma. During discharge, the cables, the electrodes and plasma channel between the electrodes provide a resistance $R$. The cables also provide an inductance $L$ that together with the capacitance $C$ form an RLC circuit which is a simple model for the oscillating discharge process. We can use an RLC model to the discharge current:

$$\tilde{I}(t) = I_0 e^{-t/\tau} \sin(\omega t) \tag{2.9}$$

Where $\tau = 2L/R$ is the oscillation decay time constant and $\omega = \sqrt{1/LC - (R/2L)^2}$ is the oscillation frequency. Fitting equation (2.9) to a current trace (see *e.g.,* figure 2.4) allows us to extract the total resistance $\tilde{R}$ and inductance $\tilde{L}$ as free parameters, which are in the orders of 1 Ω and 1 µH respectively. These RLC parameters result in discharge durations of ca. 10 µs, significantly faster than the discharge frequency. The inverse of the discharge duration sets an upper discharge frequency limit on the order of 100 kHz. In practice, however, external triggering is required to obtain controlled discharges at frequencies beyond 1 kHz in rod-to-rod electrode configurations [40], although alternative electrode configurations like wire-to-plate have demonstrated much higher discharge frequencies [41] by more efficient residual ion flushing. Simply increasing the charging current will eventually lead to glow or arc discharge [38, 40], which have different electrical and particle production characteristics and are beyond the scope of this thesis.

From the current fit and estimated resistance, we can also estimate the instantaneous power and discharge energy:

$$\tilde{P}(t) = \tilde{I}(t)^2 \tilde{R} \tag{2.10}$$

$$\tilde{E}(t) = \int_0^t \tilde{P}(\tau) d\tau \qquad (2.11)$$

Estimating the discharge energy with equations (2.10) and (2.11) is more straightforward than from the product of individual current and voltage measurements that require the phase between them to be accurately measured [42]. Compared to the theoretical amount of energy stored in the capacitors, applying equation (2.11) results in lower discharge energy values. Measurements by Mylnikov et al. indicate that a fraction in the order of 10% of the discharge energy dissipates over the electrode gap, where the rest is consumed by parasitic resistances in the circuit [43].

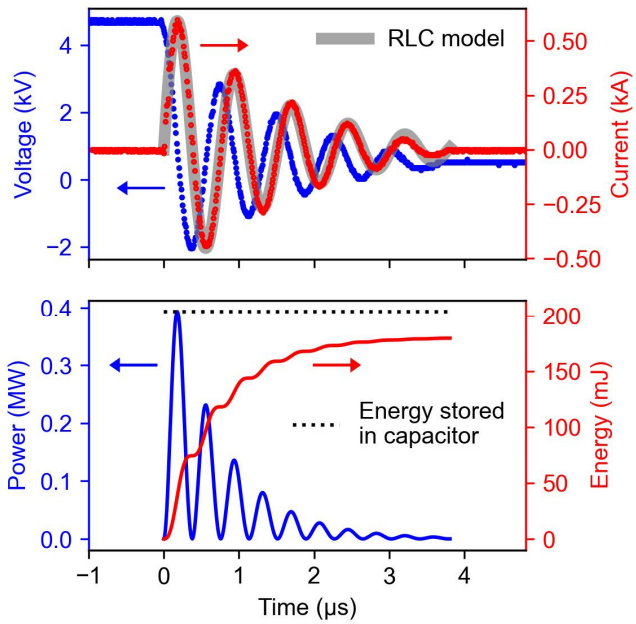


**Figure 2.4.**
Electrical discharge characteristics in spark ablation. Top panel shows the oscillating discharge voltage and current typical for spark ablation. The current trace has been fit with an RLC model that is used in the bottom panel to estimate instantaneous power and energy dissipation during disharge, which is lower than the theoretical amount of energy stored in the capacitor bank.

Additionally, not all energy dissipated across the spark gap is used toward NP generation. This is evident to anyone who has experienced spark ablation in operation: each discharge is associated with emission of sound and light. A portion of the energy is lost as heat; some energy leads to optical emission from atomic and ionic species in the plasma, which can provide information on the abundance, and spatial and temporal profiles of the present species [42, 44, 45]. Optical emission spectroscopy (OES) is a

non-intrusive technique that can extract useful process information from the discharges in spark ablation. Figure 2.5 shows an example of optical spectra collected from spark ablation of AuAg NPs at different discharge energies, as estimated with equation (2.11). All spectra contain atomic and ionic emission lines of both electrode metals, indicating we could use this information to determine NP composition. Composition is an important metric for bimetallic NPs, and the next section describes how we can relate these optical spectra to NP stoichiometry with machine learning models.

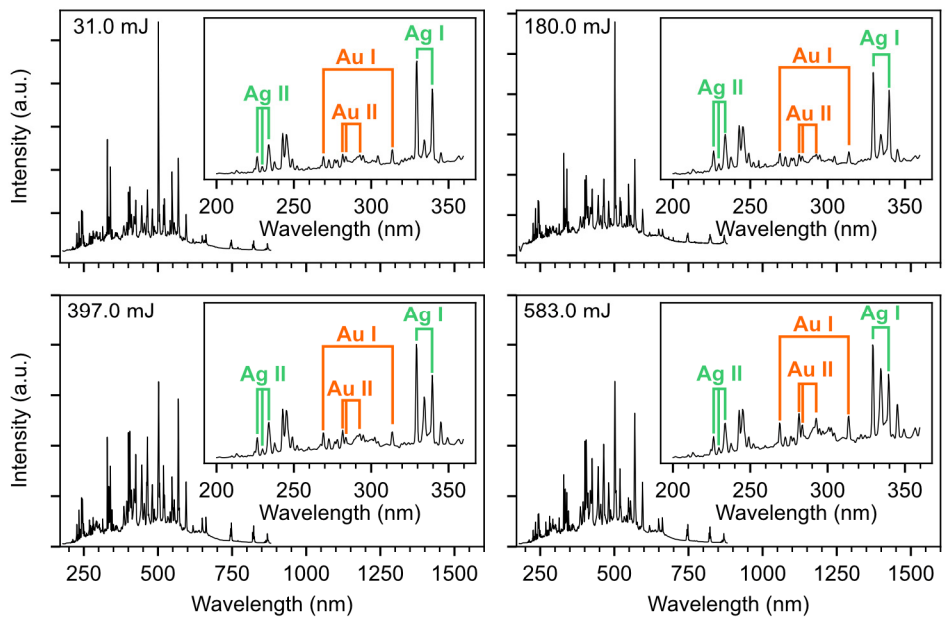


**Figure 2.5.**
Optical spectra from spark ablation of alloyed AuAg electrodes (50 at. % Au) collected at different discharge energies. Insets show the UV wavelength range with some Au and Ag emission lines labelled.

Importantly, the oscillating discharge power ablates material from both electrodes, which allows us to make mixed aerosol NPs containing elements from each electrode. This is a crucial feature of spark ablation to realize composite nanoparticles like bimetallic NPs from two or more electrodes of different materials. In figure 2.6 below is an example of the resulting nanoparticle composition of spark ablation of alloyed and pure Au and Ag electrodes, measured by X-ray fluorescence (XRF). The pure electrodes were configured in two ways: Au cathode and Ag anode; Ag cathode and Au anode. The composition of the alloyed AuAg electrodes is labeled after composition; for instance, 25:75 means 25 at. % Au and 75 at. % Ag.

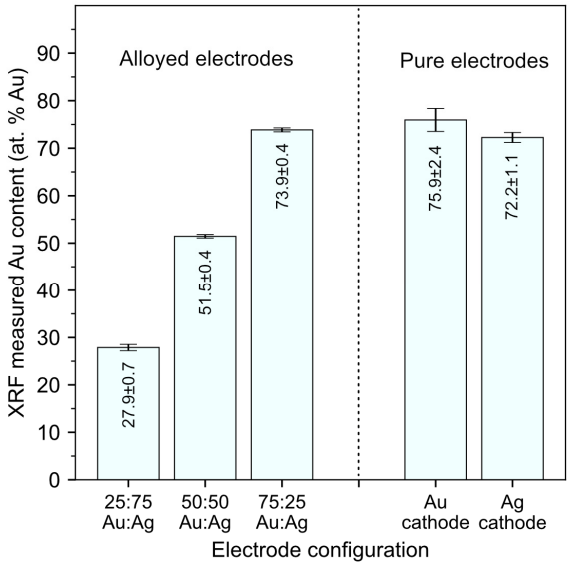


**Figure 2.6.**
XRF measured compositions of AuAg nanoparticle samples generated by spark ablation with various electrode configurations of alloyed electrodes (left side) and pure electrodes (right side).

For the pure electrodes, the ablation is generally stronger on the grounded cathode. This is seen as the increase in measured Au content for the bar corresponding to "Au cathode". If we consider the flow of energy by integrating the power when current flows in the positive direction versus the negative direction, we realize that most of the power dissipates in the cathode, due to the exponential damping. During the discharge, the alternating direction of current flow makes it so that both electrodes take turn being cathode, and hence we obtain composite aerosol NPs from using different electrodes. The fact that the Au content still dominates when Ag is cathode is due to difference in "ablatability". It is well-known, though not precisely why, some materials are easier to ablate than others. Au, for example, has a much higher ablatability than Ag in spark ablation [26].

An interesting consequence of the oscillating power during discharges is that it is possible to partly control how much energy deposits to the anode and cathode, which in turn means how much material is produced from each electrode. If we again consider equation (2.11), we realize that if we change any of the electrical parameters, the oscillation will change, too. Specifically, if we change the resistance $R$, we change the dampening of the oscillation. The higher the resistance, the shorter the duration of the discharge and the less energy deposits in the anode, resulting in a particle enrichment

of the cathode material. The consequences of changing the circuit resistance in spark ablation in terms of particle production was studied Kohut et al. [46] who found, not surprisingly, that an increase in circuit resistance decreased the electrode erosion rate leading to a lower aerosol concentration of smaller NPs due to more power dissipation in the added resistance. Feng et al. [47] proposed a model based on the influence of resistance on the energy partitioning between anode and cathode to control the particle composition in the generation of bimetallic NPs. Kohut et al. [48] refined this model and demonstrated good compositional tunability of a bimetallic AuAg aerosol.

### 2.3.2 Process monitoring: aerosol stoichiometry from optical emission

With the ability to make composite NPs with spark ablation and to control their chemical composition by tuning process parameters [48], determining the stoichiometry on-line without slower and costly off-line analysis would be attractive to monitor and optimize the synthesis process. In **Paper I**, a simple method was developed to determine the composition of a bimetallic aerosol on-line from the optical emission during the discharges in spark ablation. A bimetallic AuAg aerosol was used as a test system, though the method is in principle generalizable to other materials, as long as emissions corresponding to the present materials can be resolved in the optical spectra.

#### *2.3.2.1 Data collection*

The experimental setup is shown in figure 2.7. AuAg aerosols with different compositions ranging from 0 at. % Au to 100 at. % were synthesized with spark ablation using pure Au and Ag electrodes, and alloyed AuAg electrodes at 25 at. % Au, 50 at. % Au and 75 at. % Au content to span the entire compositional range. During the sample synthesis duration of 1 min, optical emission in the 250 nm – 800 nm range was sampled with a low-cost spectrometer through a parabolic mirror and an optical fiber over durations on the order of 10s of milliseconds. This allows us to sample many spectra during a 1 min NP synthesis session, and the collected spectra were averaged into one that represents one sample. Examples of these spectra are shown in figure 2.5. Simultaneously, the generated NPs were deposited on a filter roll inside an aerosol X-ray fluorescence (XRF) device that, after the 1 min NP sampling, analyzed the sample composition for 5 min, exemplified in figure 2.6. This procedure was repeated for four different discharge energies, which were set by the electrode distance and determined by measuring the discharge current and applying equation (2.11).

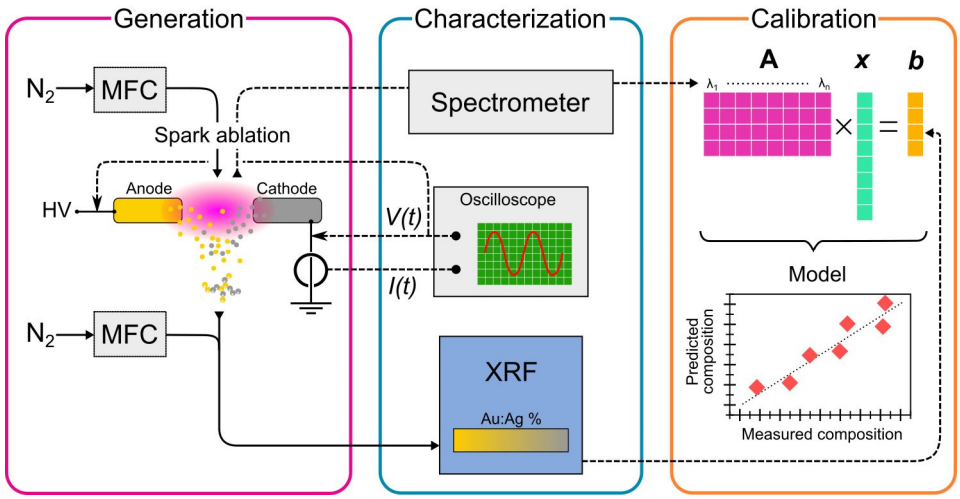


**Figure 2.7.**
Schematic setup for on-line compositional measurements of bimetallic nanoparticles generated by spark ablation. During spark ablation of AuAg nanoparticles, optical emission is sampled with a spectrometer, and the composition of the generated particles is measured with XRF. This data is used to build machine learning calibration models with the LASSO in order to be able to estimate composition from solely optical spectra.

### *2.3.2.2 Regression model*

A simple approach to connect the optical emission spectra to the NP composition is using linear multivariate calibration models, which have proven to be as effective or better than more advanced, non-linear models [49], while not requiring any a priori knowledge of the specific optical transitions in the spectra. Sparse models like the least absolute shrinkage and selection operator (LASSO) [50] that use only a fraction of the available variables (wavelengths) have found success in related work to determine composition of particulate matter [51, 52].

A linear calibration model can be described by the matrix equation $\mathbf{A}\boldsymbol{x} = \boldsymbol{b}$ where $\mathbf{A}$ is a $m \times n$ matrix of $m$ spectra and $n = 2048$ channels (wavelengths), $\boldsymbol{x}$ is a $n$-sized coefficient vector describing the weight (importance) of each wavelength to determine the composition of the $m$ samples in $\boldsymbol{b}$ measured by XRF. The goal is to find an appropriate coefficient vector that minimizes some error function. LASSO minimizes the following error function:

$$\underset{\boldsymbol{x}}{\operatorname{argmin}} \left\{ \frac{1}{2} \|\boldsymbol{b} - \mathbf{A}\boldsymbol{x}\|_2^2 + \beta \|\boldsymbol{x}\|_1 \right\} \qquad (2.12)$$

Where the first term in equation (2.12) is the least-squares solution and the second term is a $L_1$ penalty tuned by the $\beta$ hyperparameter. The $L_1$ penalty measures the absolute distance of each coefficient from zero and minimizing the error function allows the LASSO to shrink some coefficients to zero. The idea behind applying the LASSO to this kind of data is that from the 2048 sampled wavelengths, only a few are likely to be needed to make predictions of the NP composition. For instance, most transitions in the optical emission from spark ablation come from the carrier gas, simply from its abundance compared to the electrode material vapor [44]. Further, because the OES data is integrated over durations much longer than a discharge (10s of ms compared to ca. 10 µs), a significant bremsstrahlung background is present in the spectra (figure 2.5), and many of the channels only contain bremsstrahlung background radiation. This $L_1$ penalty enables the LASSO to select the most important wavelengths, that are presumably correlated to Au and Ag wavelengths, forcing other, "unnecessary" wavelengths to zero.

Figure 2.8 shows LASSO calibration model results applied to test data at four different discharge energies of 31.0 mJ, 180.0 mJ, 397.0 mJ and 583.0 mJ. The test data are spectra the model has not analyzed before, which constitutes 30% of the sampled spectra and corresponding NP compositions; the remaining 70% were used to train the models.

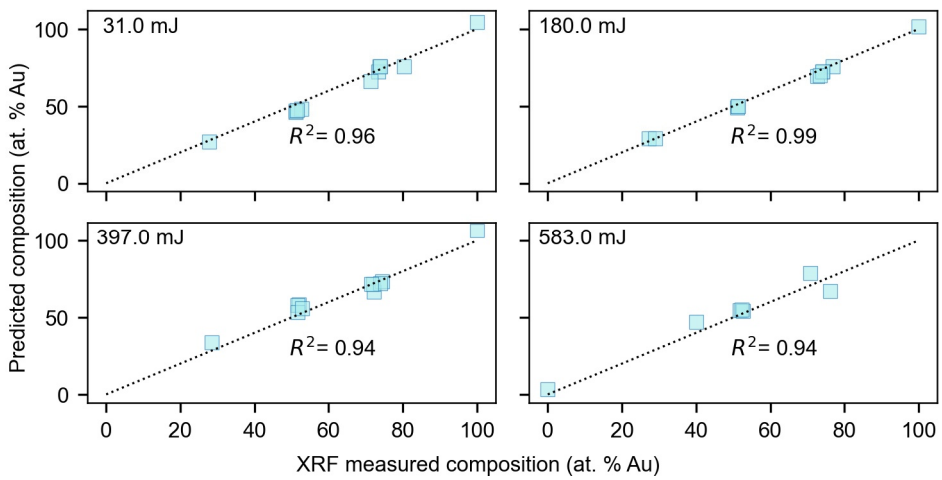


**Figure 2.8.**
LASSO calibration results for models trained on optical spectra from spark ablation of AuAg nanoparticles at different discharge energies. The dotted curves show the 1:1 line between the Au at. % content (measured by XRF) and the predicted Au at. % content from the optical spectra.

We imposed constraints on the models such that a *maximum* of 50 wavelengths could be used, corresponding to less than 3 % of all sampled wavelengths. This constraint is somewhat arbitrary, but the guiding principle is to make the model as simple as possible while maintaining good performance. If too many wavelengths are used, the models tend to overfit the data. If too few wavelengths are used, the model does not have enough flexibility to predict composition. Performance has been measured in mean absolute error (MAE), root mean squared error (RMSE) and $R^2$ (coefficient of determination). MAE and RMSE are both measured in the same unit as the unit we are trying to predict (at. % Au), though the MAE is less sensitive to outliers. $R^2$ is another common metric that indicates how well the variance in the data is described by the LASSO model. The model results are summarized in table 2.1, including a model trained on data pooled from all discharge energies.

**Table 2.1.**
LASSO model statistics for four models trained on spectra sampled at different discharge energies and one model trained on spectra from all discharge energies.

| | 31.0 mJ | 180.0 mJ | 397.0 mJ | 583.0 mJ | All energies |
|---|---|---|---|---|---|
| **$R^2$** | 0.96 | 0.99 | 0.94 | 0.94 | 0.95 |
| **RMSE (at. % Au)** | 3.8 | 1.9 | 4.3 | 5.6 | 6.5 |
| **MAE (at. % Au)** | 3.4 | 1.7 | 3.5 | 4.9 | 4.9 |
| **Wavelengths used** | 12 | 31 | 40 | 37 | 44 |

The results are promising, with MAEs generally < 5 at. % and RMSE values comparable to other multivariate calibration models applied to similar techniques like laser induced breakdown spectroscopy (LIBS) [49] and spark induced breakdown spectroscopy (SIBS) [52, 53] of aerosol NPs. Compared to LIBS and SIBS, our setup is non-destructive, as the information on the NPs' composition comes from the same process generating them. Our setup is also arguably faster, easier and more cost-effective, as LIBS requires a laser system, and SIBS may require lengthy particle deposition times to achieve enough material that can be ablated and give a sufficient signal-to-background in the OES data [52].

### 2.3.3 Particle formation

The discharge process is characterized by several stages, where the arc stage, which occurs within some microsecond of the onset of discharge, leads to electrode ablation [44]. OES investigations have found that the discharge plasma temperature can reach temperatures of 10 000 K – 20 000 K [44, 45]. It is believed that this high temperature combined with sputtering from ions in the plasma drives the electrode ablation [28,

40, 42, 54], which makes spark ablation able to create NPs out of most solid materials that are conductive enough to facilitate discharges over the electrodes.

After a few microseconds, the energy input from the capacitors ceases. The plasma, now containing a high concentration of electrode atoms and ions, rapidly cools to the surrounding gas temperature (typically room temperature) at rates of up to $10^8$ K $s^{-1}$ [45], precipitating NPs by nucleation. Using the information of plasma temperature and cooling rate, we can estimate the nucleation process duration to some 10 µs [54]. In this afterglow stage, large supersaturation of electrode atoms leads to the nucleation of particles. Supersaturation is the ratio of vapor pressure $p$ to the equilibrium vapor pressure $p_s$ at some temperature $T$ (here: room temperature) over a flat surface, $S = p/p_s$. Over curved surfaces, like NP surfaces, the Kelvin or Thomson-Gibbs equation describes the supersaturation required to maintain mass equilibrium (the Kelvin ratio) in a particle with diameter $d_p^*$ [19]:

$$p/p_s = \exp\left(\frac{4\gamma M}{\rho_p R T d_p^*}\right) \tag{2.13}$$

Where $R$ is the gas constant and $\gamma$, $M$ and $\rho_p$ are the surface energy, molecular weight and density of the particle. For some Kelvin ratio, particles larger than $d_p^*$ will grow by condensation [19]. Due to the high supersaturation after the discharge, this theoretically entails all electrode vapor atoms and clusters can form stable particles, growing into single digit nm NPs, called "singlets" [55]. Growth by condensation will be covered later in the thesis.

A high concentration of singlet NPs leads to particle-particle collisions and further growth by coagulation, which is the dominating NP growth mechanism in most cases for spark ablation. Depending on the singlet size and material, and the temperature, coagulation between two singlets may lead to full coalescence driven by a reduction in particle surface energy [56]. If the coagulation time is quicker than the coalescence time, however, fractal-like nanostructures consisting of primary particles form [57]. Usually, "loosely" bound primary particles (bound by *e.g.,* van der Waals forces) are called agglomerates, whereas "strongly" bound primary particles (*e.g.,* partially sintered) are called aggregates [58]. For simplicity, we will refer to these nanostructures as agglomerates. Aerosols undergoing coagulation tend to attain a log-normal size distribution, which is the typical particulate output from spark ablation.

The coagulation rate of NPs produced, and hence their sizes, can to some extent be controlled. Decreasing the discharge power in general, either through discharge energy (by changing gas or decreasing electrode distance) or frequency (*e.g.,* by decreasing charging current) leads to a decrease in singlet concentration and coagulation rate. The

carrier gas used and its flow rate have large impacts on NP generation. A higher flow rate leads to a lower particle concentration which dilutes the aerosol and slows coagulation [18]. Additionally, increasing flow rate decreases residence time in the aerosol setup, which is beneficial for reduced material loss from deposition of small NPs inside the spark ablation chamber and tubes transporting the aerosol. Some carrier gases, like He, have comparatively small breakdown voltages. Combined with a small discharge energy, for instance by using a low capacitance, spark ablation can produce NPs containing only a few atoms, called atomic clusters [37].

## 2.4 Off-line characterization

While on-line characterization is useful to monitor and optimize processes in aerosol technology, complementary off-line techniques like electron microscopy are crucial to analyze the product and help us understand what happens in the aerosol synthesis. To apply any off-line characterization, the airborne particles need to first be deposited on a suitable substrate, which can be done by for example electrostatic deposition.

### 2.4.1 Electrostatic deposition

In this thesis, an electrostatic precipitator (ESP) has been used to deposit NPs from the aerosol phase. The ESP uses a strong electric field to attract charged particles onto a grounded plate where the substrate is placed. While the particles need to be charged, the ESP boasts a high collection efficiency for NPs (in laminar flow) and flexibility in choice of deposition substrate. Additionally, with knowledge of particle concentration in the gas, $c_{\mathrm{gas}}$, and aerosol flow rate, $Q_{\mathrm{a}}$, it is possible to control the surface concentration and size of the circular area over which particles deposit.

Preger et al. [59] showed that the ESP deposition spot radius $r_{\mathrm{spot}}$ has a simple analytic expression:

$$r_{\mathrm{spot}} = \sqrt{\frac{Q}{\pi v_d}} \tag{2.14}$$

$$v_d = E\frac{neC_c}{3\pi\eta d_p} \tag{2.15}$$

Where $v_d$ is the particle drift velocity in the electric field, $E$. In the monodisperse case, *i.e.,* when we have size-selected particles with a DMA prior to deposition, the surface

concentration of NPs in the deposition spot, $c_{\text{spot}}$, is directly proportional to deposition time $t$ and $c_{\text{gas}}$ [59]:

$$c_{\text{spot}} = t c_{\text{gas}} v_d \tag{2.16}$$

In the polydisperse case, we need to account for the concentration of particles with a particular diameter, the diameter dependence in equation (2.15), and the charging probability $f_n(d_p)$. Then, we find

$$c_{\text{spot}}(d_p) = t\frac{Ee}{3\pi\eta} \times c_{\text{gas}}(d_p)\frac{C_C}{d_p}\left(f_{n=-1}(d_p) \times 1 + f_{n=-2}(d_p) \times 2 + \cdots\right) \tag{2.17}$$

Where $f_{n=-1}(d_p)$ is the probability of a particle with diameter $d_p$ having charge $-1 \times e$ (assuming negatively charged particles). This assumes an aerosol with a known charge distribution. For the Boltzmann charge distribution, $f_n(d_p)$ can be estimated with equation (2.6). The factor 1, 2, …, etc. is to account for the increased drift velocity for particles with multiple charges (equation (2.15)). This has a minor impact for small NPs as the probability of multiply charged particles is low. Note that the size and charge dependence for $r_{\text{spot}}$ means that equation (2.17) only holds within this radius for a given particle diameter and charge.

### 2.4.2 Electron microscopy

Electron microscopy (EM) is probably the most powerful analytical technique for characterizing NPs. Thanks to the short de Broglie wavelength of electrons, the EM resolution is superior to optical microscopy. The dynamics between high energy electrons and matter further allows for the collection of complementary information to electron imaging (figure 2.9).

The two main configurations of EM, transmission electron microscopy (TEM) and scanning (transmission) electron microscopy (SEM/STEM, S(T)EM) conceptually share likenesses to optical microscopy. In both configurations, an electron gun provides “illumination” with accelerated electrons that are shaped to a beam by a set of electromagnetic condenser lenses. Depending on the configuration, the electron beam is either made parallel (TEM) or converged to a small spot (S(T)EM). In S(T)EM, electromagnetic coils are used to scan the electron probe over the sample.

In TEM, the sample induces amplitude and phase variations in the outgoing electron wave that is transferred as an image via another set of electromagnetic lenses to a fluorescent screen or digital image sensor. In SEM, the converged beam produces

(elastically) backscattered electrons (BSE; from the beam) and secondary electrons (SE; emitted from the sample) (figure 2.9). The low energy of the SE entails a short mean free path in the sample and therefore a resolution close to the electron beam diameter, often ~1 nm or better, the size of which is mainly set by acceleration voltage. The much higher energy BSEs emerges from deeper within the sample, and hence provide a lower resolution. BSE intensity is on the other hand related to the atomic number (Z), which provides elemental contrast. In a similar way, a good Z contrast with superior resolution is obtainable by collecting *transmitted* electrons from the scanned electron probe in STEM with a medium to high angle annular dark field (M/HAADF) detector. HAADF STEM is particularly useful for imaging heterogeneous NPs with elements with large Z differences.

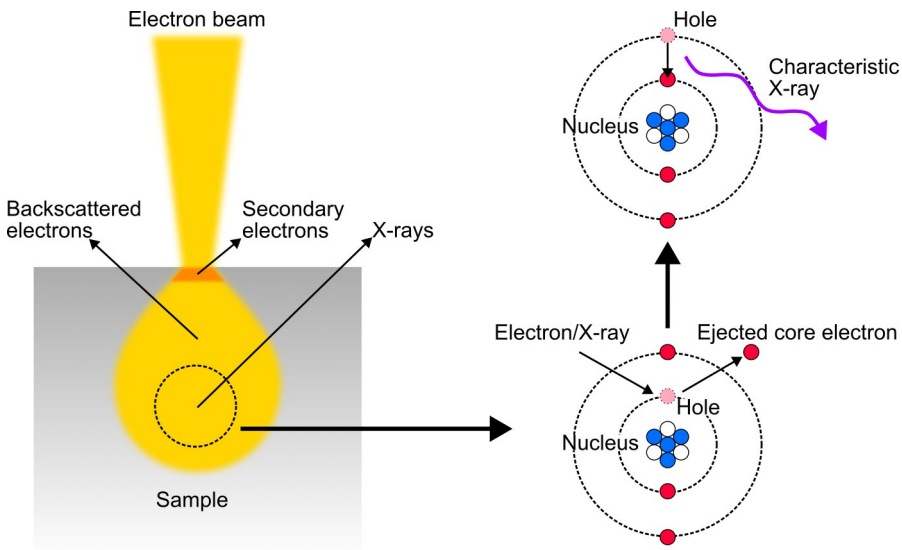


**Figure 2.9.**
Schematic figure of electron-matter interactions and the atomistic mechanism for characteristic X-ray emission used in X-ray spectroscopy. A focused electron beam probe will spread out to a "pear shaped" interaction volume in the sample. Secondary electrons with low mean free paths originate from near the surface of the sample, whereas backscattered electrons and sample characteristic X-rays come from deeper within the interaction volume.

### 2.4.3 X-ray spectroscopy

High energy particles, like photons and electrons, can transfer energy to matter by inelastic collisions, leading to the ejection of core electrons from the atom. The excited matter may relax by filling the core hole with an electron from a higher energy state, emitting an X-ray photon with energy equivalent to the difference between the hole

and electron energy in a process known as X-ray fluorescence (XRF; figure 2.9). These X-rays are characteristic of the element they originated from, which makes the process useful as an analytical technique to determine what elements are present in a sample.

In this thesis, XRF has been used with excitation from X-ray photons and electrons inside EMs. The latter technique is more commonly known as energy dispersive X-ray spectroscopy (EDX), though apart from the energy source, the two techniques are analogous and use the same type of sensor to detect the characteristic X-rays from the sample. The benefits with XRF using separate X-ray sources as excitation are that it can operate at ambient pressure with bulk samples. Whilst TEM-EDX and STEM-EDX require samples thin enough for electron transmission, the ability to focus the electron beam presents unparalleled resolution of the sampling area. Indeed, by scanning the electron probe in STEM-EDX, we can capture an X-ray spectrum at each "pixel" and transform the data to high resolution elemental maps (figure 2.10). This technique is arguably the most useful off-line analytical technique to study nanostructures, especially segregated NPs like core-shell and Janus NPs.

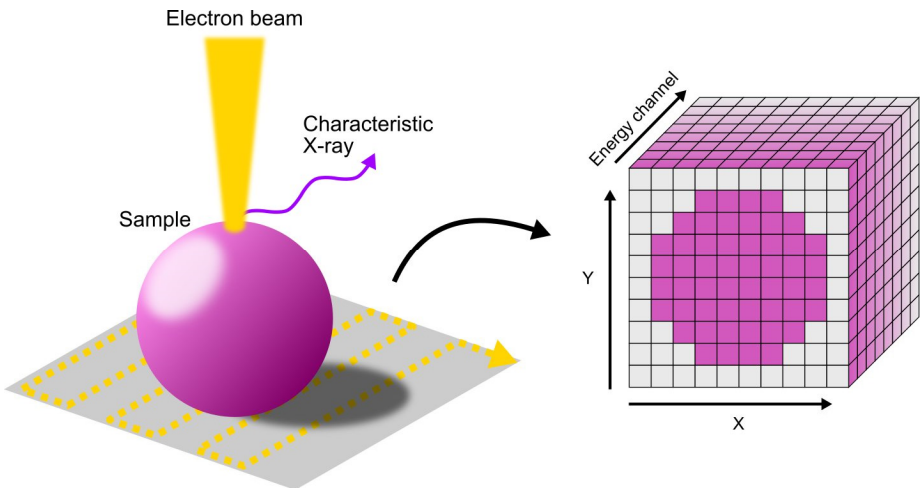


**Figure 2.10.**
Schematic of STEM-EDX. A focused electron beam is scanned over the sample in a raster pattern, and the sample's characteristic X-rays are sampled at each scan location (pixel). The STEM-EDX data can be interpreted as a datacube with two spatial dimensions and one X-ray energy dimension.

# 3 Thermal processing

The rapid motion of small NPs in the gas phase tends to lead to coagulation that results in aerosols with broad, log-normal size distributions being the product from most aerosol sources, including spark ablation. While agglomerates are interesting to study in various applications, it is often convenient to deal with monodisperse, spherical particles. One example of this has already been mentioned: the equivalence between mobility diameter and geometric diameter for spherical aerosol particles size-selected with a DMA.

An important aspect of aerosol technology is the ability to measure and modify the aerosol in situ. The previous part of the thesis introduced size-selection with DMAs. This section deals with modifying the aerosols with thermal processing. Thermal treatments, often called sintering or compaction, leads to restructuring of agglomerates by solid state diffusion, melting and evaporation. It can also lead to internal restructuring inside NPs, leading to *e.g.,* changes in crystal structure, and segregation of elements in bimetallic NPs. Such processes may be exploited to create heterogeneous NPs, like Janus and core-shell structures. The methodology to accomplish this, and to measure the processes on- and off-line, is presented here. The measurement principles will also be used to monitor other processes including condensational growth in the subsequent parts of the thesis.

## 3.1 Compaction

Heating up an aerosol with a tube furnace is a common method to actuate inorganic NPs directly in the aerosol phase. Elevated temperature leads to agglomerates shrinking, or "compacting", by primary particle rearrangement, coalescence, and elimination of pores between the particles. Of the several mechanisms that lead to the necessary material transport, surface diffusion, where atoms diffuse along surfaces, is generally much faster than *e.g.,* grain boundary diffusion of atoms between grains, and volume diffusion that involves atom diffusion inside the crystal lattice. The strong temperature dependence of these processes affect their relative importance at different stages of the

compaction process and temperature, where surface diffusion is initially dominant at lower sintering temperatures due to the large surface area of agglomerates [60].

The compaction process can be monitored on-line with the help of a DMA and a detector like a CPC or electrometer. A common setup used in this thesis is to use *two* DMAs, in a so-called tandem DMA setup, coupled to an electrometer, and a tube furnace placed between the DMAs. An example of such a setup is shown in figure 3.1. The purpose of the first DMA, DMA1, is to size-select a fixed mobility diameter $d_m$ subset of the polydisperse aerosol generated by spark ablation. The second DMA, DMA2, is scanned over a range of mobility diameters with the electrometer to monitor the size distribution after the tube furnace. At room temperature, the agglomerates size-selected by DMA1 have some size distribution centered around $d_m$, measured by DMA2 and the electrometer. Tandem DMA setups like this one can be used to study other aerosol processes, including growth of NPs, which will be described more later in the thesis.

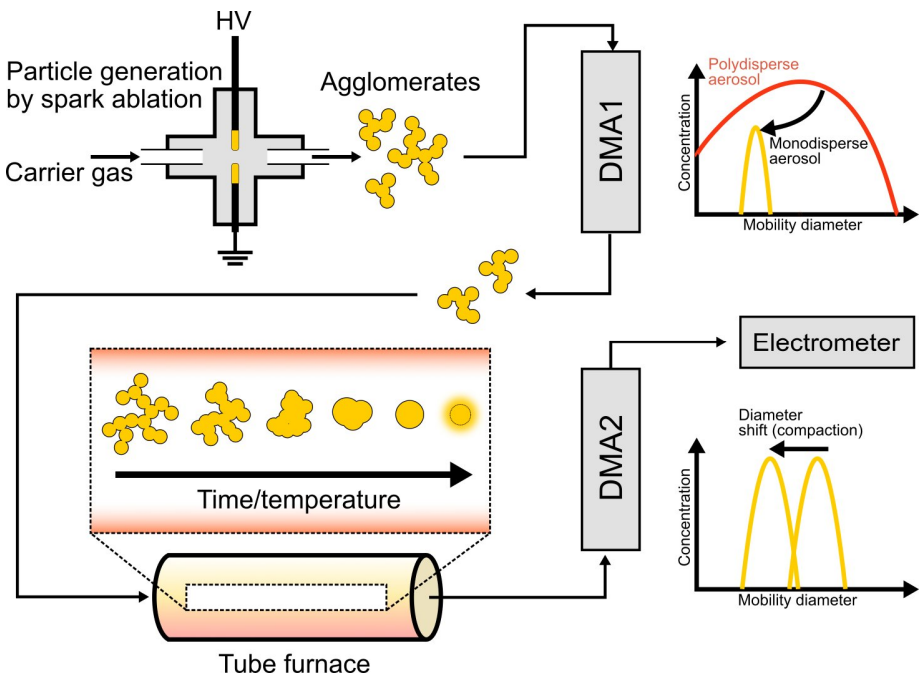


**Figure 3.1.**
Thermal compaction of aerosol nanoparticles can be studied with a tube furnace and a tandem DMA setup. DMA1 selects a monodisperse population of a polydisperse aerosol of agglomerates generated by spark ablation. As the temperature in the tube furnace is increased, compaction of agglomerates is detected as a decrease in mobility diameter measured with DMA2 and a detector like an electrometer.

As the tube furnace temperature is increased, the size distribution will shift toward smaller $d_m$, indicative of compaction. For many materials, $d_m$ will remain constant after some temperature, called the compaction temperature, $T_c$. At this point, the particles are "compacted" and essentially spherical. Depending on NP size and material, the particles may generally attain polyhedron shapes given by the Wulff construction [61]. We will for simplicity refer to the compacted shape as spherical here. $T_c$ depends on the material (and atmosphere [62]), residence time in the tube furnace, and initial agglomerate size.

Several models have been developed to describe the compaction process of aerosol agglomerates. It is suggested that strongly bond primary particles lead to compaction by coalescence of primary particles, driven by a reduction of surface area [56]; agglomerates with weakly bond primary particles can also compact by rearrangement of primary particles [63]. Models describing these processes applied to experimental data indicate that agglomerates with smaller primary particles tend to coalesce faster than agglomerates with larger primary particles that primarily compact by restructuring [64], which could be an effect of melting point suppression in smaller NPs [65].

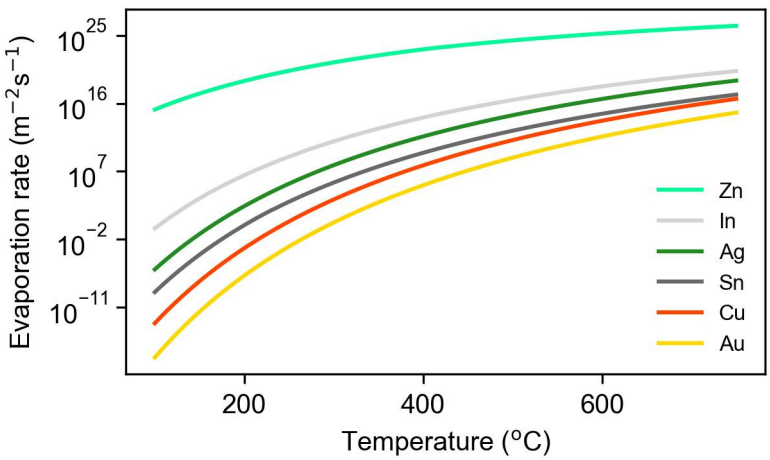


**Figure 3.2.**
Evaporation rate of some metallic elements calculated with vapor pressure data from Ref. [66].

Compilation of experimental data on metal, semiconductor and metal oxide NP compaction shows that the ratio between compaction temperature $T_c$ and melting temperature $T_m$ often lies between 0.3 – 0.8, indicative of solid state diffusion processes [60]. Beyond $T_c$, higher compaction temperatures can lead to internal rearrangements

such as increased crystallinity [67, 68]. Notably, if the temperature is high enough, a further decrease in $d_m$ is often observed due to evaporation. Evaporation can qualitatively be described with the Knudsen equation:

$$J_{ev}/A = \frac{p_v}{\sqrt{2\pi m k_B T}} \quad (3.1)$$

Where $J_{ev}/A$ is the area normalized evaporation rate at temperature $T$ for an element with vapor pressure $p_v$ and atomic mass $m$. The vapor pressure $p_v$ is material specific and strongly temperature dependent. Figure 3.2 shows the evaporation rate for a few metallic elements using vapor pressure data from Ref. [66]. Notably Zn, has a high evaporation rate due to its exceptionally high vapor pressure. This fact will be exploited later in the thesis for thermal evaporation processes used for core-shell NP synthesis.

## 3.2 Thermally induced surface segregation in free CuAg nanoparticles

The easily observable compaction of aerosol NPs entails several atomic rearrangement mechanisms that leads to shrinking and restructuring of the fractal-like agglomerates. The underlying processes are significantly more complex for composite NPs containing several elements. Under the right circumstances, we can take advantage of these processes to deterministically make segregated structures, like Janus and core-shell NPs, in one compaction step, without separate apparatus or synthesis steps that are typically utilized to add materials in a sequential manner. This is the main idea of **Paper II**, where we used a tube furnace to induce compaction and surface segregation, *i.e.,* the enrichment of one element towards the surface, of CuAg aerosol NPs generated by spark ablation.

### 3.2.1 Compaction of CuAg agglomerates

CuAg is a well-studied immiscible system [69], that has been shown to adopt both Janus and core-shell configurations in physical and chemical synthesis of NPs [70-73]. Interestingly, the authors of Refs. [70] and [71] report different conclusions on preference in chemical ordering: in the physical synthesis, the transition from a core-shell to a Janus structure is observed with increased Ag shell thickness [70], while a core-shell morphology may be more preferable with higher Ag content in the chemical synthesis [71]. Spark ablation synthesis of CuAg NPs has previously demonstrated enhanced miscibility of CuAg in the agglomerates compared to the bulk phase diagram,

presumable due to the fast quenching and small size of the primary particles [74]. To study and tailor the chemical configuration of the NPs without influence of a substrate or solvents, we have combined spark ablation with in-flight compaction of "free" CuAg agglomerates in our aerosol technology setup (figure 3.1).

Figure 3.3 shows the compaction curve of a CuAg aerosol generated by spark ablation with a pure Ag anode electrode and a pure Cu cathode electrode, using the experimental setup schematically depicted in figure 3.1. Since Cu is especially susceptible to oxidation, a 95 % $N_2$: 5 % $H_2$ carrier gas was used [75]. Figure 3.3 displays a typical shape of a metallic aerosol compaction process: the initial slow decrease in $d_m$ is followed by an accelerated decrease at around 500 °C, terminated by a plateau of constant $d_m$ at a compaction temperature around $T_c$ = 600 °C. After about 800 °C, the mobility diameter drops again, which we can assume to be from Ag evaporation, due to its higher vapor pressure and evaporation rate at that temperature (figure 3.2). This is corroborated by the decrease in rate of mobility diameter decrease; Cu evaporation would likely lead to a continued decrease of $d_m$ with increasing tube furnace temperature.

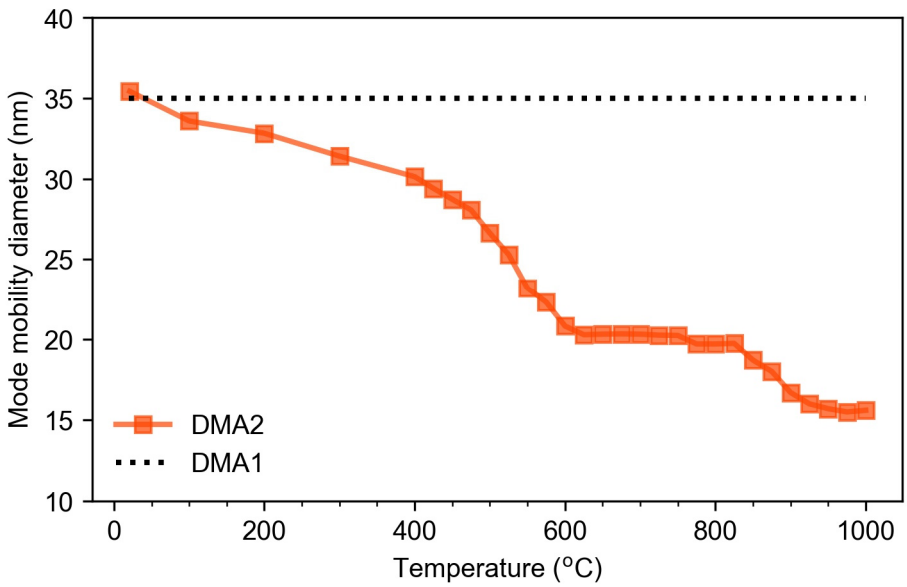


**Figure 3.3.**
Compaction curve of CuAg agglomerates. 35 nm mobility diameter CuAg agglomerates are size-selected by DMA2. The mode mobility diameter of the agglomerates, as a function of tube furnace temperature, is measured with DMA2 and an electrometer.

While the mobility measurements in figure 3.3 can give us some information about the compaction process, the different processes leading to agglomerate compaction likely affect Cu and Ag at separate rates, which is not discernible in the mobility analysis alone. Importantly, around and after $T_c$, atomic rearrangements affecting chemical ordering of Cu and Ag in the NPs may still occur. For an immiscible system like CuAg, this leads to interesting dynamics that we cannot determine from the compaction plot alone. We need off-line characterization like electron microscopy to study that in detail.

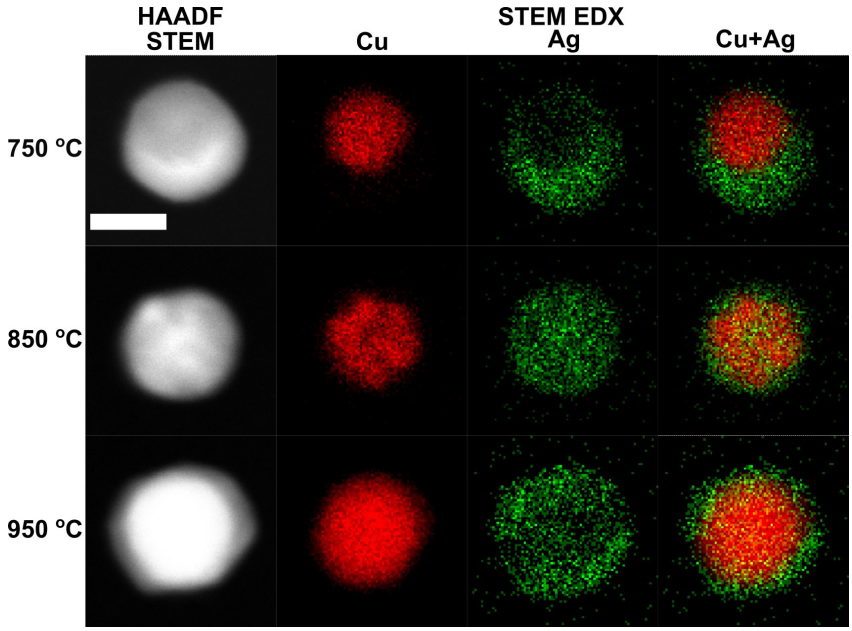


**Figure 3.4.**
STEM micrographs and STEM-EDX elemental maps of CuAg nanoparticles compacted at tube furnace temperatures of 750 ºC, 850 ºC and 950 ºC. Scalebar is 20 nm.

### 3.2.2 Electron microscopy characterization

Informed by the compaction data, we prepared 30 nm diameter size-selected NP samples compacted at 750 °C, 850 °C and 950 °C and studied them with TEM and STEM. The STEM micrographs in figure 3.4 indicate segregation discernible from the Z contrast between Ag and Cu; the brighter parts correspond to Ag rich parts of the NP. The elemental distributions obtained by STEM-EDX clearly display the segregation in the particles at the different temperatures. At 750 °C, the spherical particles obtain a "quasi-Janus" or "crescent" [71] morphology (see also figure 1.1), where an Ag rich phase partly wraps around a Cu rich phase, but is also reminiscent of

two separate “faces”. At the two higher temperatures, core-shell like configurations appear, with a patchy Ag shell 850 °C, and a more cohesive shell at 950 °C. From the compaction study, we suspect Ag evaporation at 950 °C, which was supported by TEM-EDX compositional measurements on 30 individual NPs per sample (table 3.1): at 950 °C, the particles contain significantly less Ag.

Both TEM-EDX and STEM-EDX are ideal to study composition of individual nanostructures, providing information lost in ensemble techniques like XRF. Note the compositional homogeneity among the individual particles studied (table 3.1). Not only is the average composition very similar for particles compacted at 750 °C and 850 °C, where Ag evaporation is less impactful for these NP sizes, but the standard deviation, being a measure of how spread the composition is among particles, is rather low. These results suggest that spark ablation is a reproducible technique for producing well-defined bimetallic NPs in composition, likely due to the high degree of vapor mixing in the electrode ablation, and in size, with the help of a DMA. The compositional homogeneity is comparable to optimized chemical synthesis techniques for bimetallic NPs [76].

**Table 3.1.**
TEM-EDX measured composition of 30 CuAg nanoparticles for different compaction temperatures.

| | Compaction temperature | | |
|---|---|---|---|
| | 750 °C | 850 °C | 950 °C |
| **Composition (at. % Ag)** | 60.7±5.8 | 60.6±5.3 | 24.4±6.5 |

We can estimate an Ag shell thickness, $t_{\text{shell}}$, from the compositional data in table 3.1 with a simple geometric relationship where we assume spherical shells and cores of pure Ag and Cu respectively. Note that the elemental distributions in the mappings in figure 3.4 do not necessarily indicate pure core and shell compositions, which will be discussed later. The volume of the spherical particle is calculated using the particle radius $R$ as $V = 4\pi/3 \times R^3$, and can also be expressed as the sums of the Cu and Ag volumes:

$$V = n_{\text{Ag}} V_M^{\text{Ag}} + n_{\text{Cu}} V_M^{\text{Cu}} \tag{3.2}$$

Where $n$ is the amount of moles of the element (Ag or Cu), and $V_M$ its corresponding molar volume. From the TEM-EDX data, we know the Ag concentration:

$$c_{\text{Ag}} = n_{\text{Ag}} \,/\, \left(n_{\text{Ag}} + n_{\text{Cu}}\right) \tag{3.3}$$

From which we can write $n_{\mathrm{Ag}} = c_{\mathrm{Ag}} n_{\mathrm{Cu}} \,/\, \left(1 - c_{\mathrm{Ag}}\right)$. Inserting this into equation (3.2), we can solve for the amount of Cu

$$n_{\mathrm{Cu}} = V \,/\, \left(\frac{c_{\mathrm{Ag}}}{1-c_{\mathrm{Ag}}} V_M^{\mathrm{Ag}} + V_M^{\mathrm{Cu}}\right) \qquad (3.4)$$

The number of moles of Cu times its molar volume gives us the volume of the spherical core, and we can compute the core radius $r$

$$n_{\mathrm{Cu}} V_M^{\mathrm{Cu}} = 4\pi/3 \times r^3 \rightarrow r = \sqrt[3]{3/4\pi \times n_{\mathrm{Cu}} V_M^{\mathrm{Cu}}} \qquad (3.5)$$

Finally, we identify the shell thickness as the particle radius minus the core radius, $t = R - r$. Using this approach, we find an Ag shell thickness of ca. 4.9 nm, 4.8 nm and 1.8 nm for the NPs compacted at 750 °C, 850 °C, and 950 °C. Langlois et al. [70] reported a transition from a core-shell morphology to a Janus morphology in CuAg NPs in their physical synthesis for Ag shell thicknesses of 3 – 4 nm, which is not congruent with our findings. The surface segregation in their synthesis method, thermal evaporation of Cu and Ag followed by thermal dewetting on a substrate, could be significantly influenced by the substrate and the lower temperatures used. Our findings are neither in line with a chemical synthesis method in Ref. [71], where an increasing Ag content led to an increased preference for core-shell morphologies. We observe core-shell morphologies with higher and lower Ag contents as seen in particles compacted at 850 °C and 950 °C. Similarly to the case of thermal dewetting on a substrate, the solvents may play a significant role for the preferred morphology. As previously suggested, the core and shells in the NPs synthesized in our setup are not necessarily pure Cu and Ag, which will be elaborated in the following section.

In **Paper II**, we also compared molecular dynamics (MD) simulations of heat treating CuAg NPs to the experimental results of in-flight compaction of CuAg agglomerates. The MD simulation results obtained with embedded-atom potential by Ref. [77] closely matched the experimental findings (figure 3.4) in morphology when using the compositions determined by TEM-EDX (table 3.1) and the same compaction temperatures, albeit for smaller NPs (2.5 nm to 4.2 nm and 10 nm). These results show promise for using aerosol technology as a platform to both study surface segregation in a substrate/solvent-free environment with a controlled atmosphere in terms of gas composition and temperature, and to synthesize heterogeneous NPs in a continuous and simple fashion.

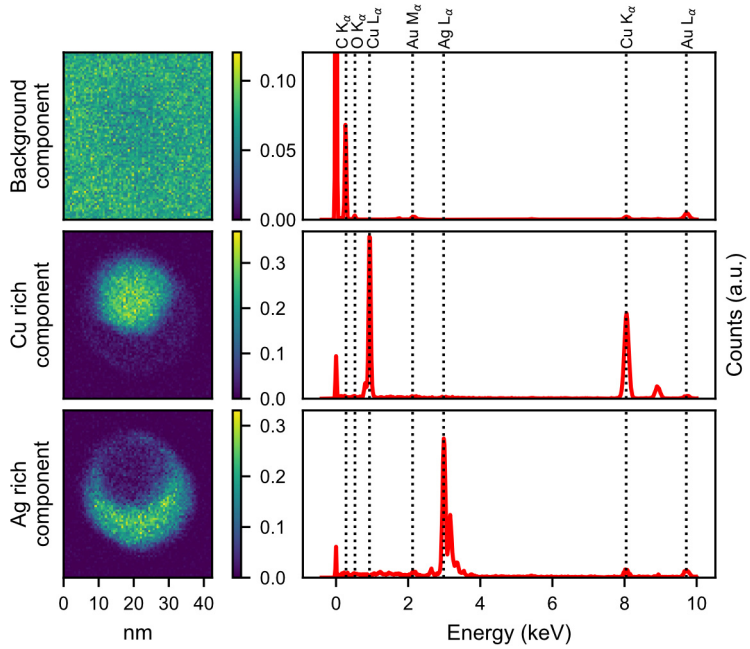


**Figure 3.5.**
Non-negative matrix factorization of a STEM-EDX map of a CuAg nanoparticle compacted at 750 ºC, showing the loadings (left column) of the spectral components (right column).

### *3.2.2.1 Phase extraction from elemental maps by machine learning*

EDX mappings can lead to insights in terms of how elements distribute in multielement NPs. However, EDX is inherently limited to elemental information, and we cannot say anything about possible chemical phases present. While Ag and Cu are immiscible in bulk, on the nanoscale, there may be some intermixing between the Ag and Cu phases that the raw EDX data cannot reveal. Further, since EDX maps are 2D projections of 3D structures, overlapping phases or components in heterogeneous NPs may confound such interpretations. Progress in multivariate statistics, in particular matrix factorization techniques, applied to EDX maps (and similar methods) has led to the exploration of extracting chemical information from elemental data and separating chemical components [78-81]. We have applied matrix factorization to the EDX maps of the compacted CuAg particles to try to understand the composition in the Ag and Cu rich parts of the particles compacted at different temperatures.

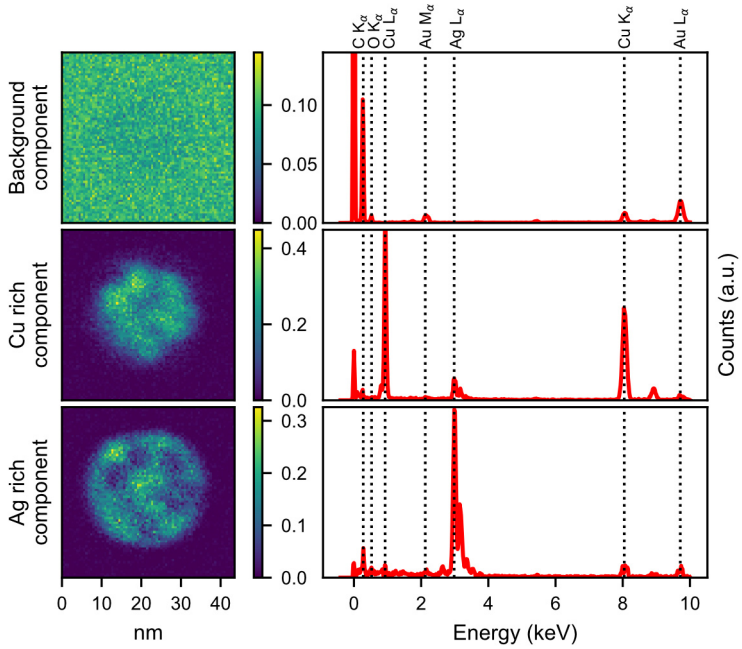


**Figure 3.6.**
Non-negative matrix factorization of a STEM-EDX map of a CuAg nanoparticle compacted at 850 ºC, showing the loadings (left column) of the spectral components (right column).

An EDX map can be described as a $(N \times K)$ matrix $\mathbf{X}$ with $N$ pixels (in the order of 10 000) and $K$ X-ray energy channels (usually 2048). If we compare $\mathbf{X}$ to the EDX map representation in figure 2.10, the two spatial dimensions are collapsed into one of length $N$. Matrix factorization decomposes $\mathbf{X}$ into two lower rank matrices, whose product approximate $\mathbf{X}$. In the context of EDX maps, these matrices are the spectral components, $\mathbf{S}$ $(J \times K)$, and their distributions in the sample (called loadings), $\mathbf{A}$ $(N \times J)$, where $J$ is the number of spectral components that ideally correlate with chemical phases in the sample. The most popular matrix factorization is principal component analysis (PCA), which creates $J$ orthogonal spectral components from linear combinations of the $K$ original channels, such that components maximize the variance in the data [79, 80]. A related technique, independent component analysis, has shown impressive results when separating overlapping EDX spectral components from core and shell in core-shell NPs [78]. We have chosen to apply non-negative matrix factorization (NMF) to the EDX maps on the CuAg particles. Although similar to PCA, NMF imposes physically meaningful constraints on $\mathbf{S}$ and $\mathbf{A}$, such that they are non-negative, which makes the results more interpretable [79-81].

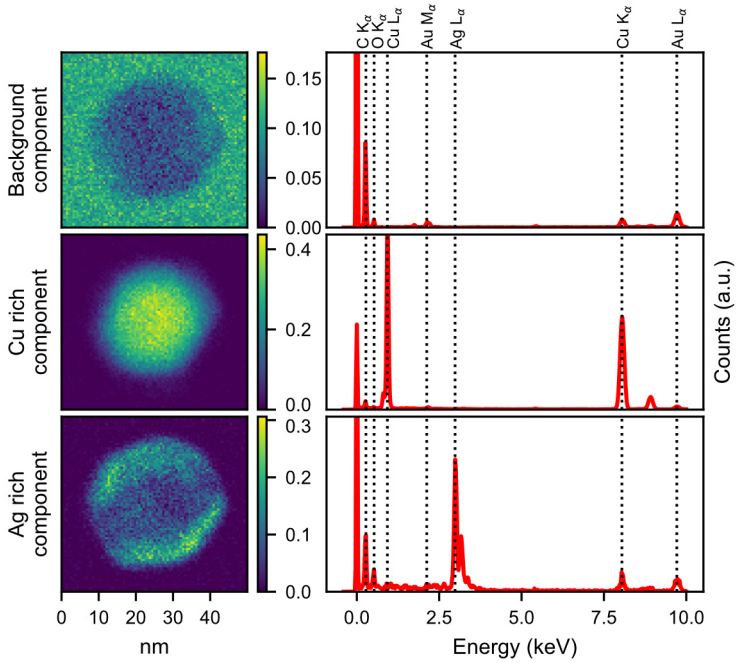


**Figure 3.7.**
Non-negative matrix factorization of a STEM-EDX map of a CuAg nanoparticle compacted at 950 ºC, showing the loadings (left column) of the spectral components (right column).

**Table 3.2.**
Average composition in Cu rich and Ag rich spectral components determined by NMF decomposition of EDX maps on CuAg nanoparticles compacted at different temperatures (five particles per temperature).

| | 750 °C | | 850 °C | | 950 °C | |
|---|---|---|---|---|---|---|
| | Cu-rich phase | Ag-rich phase | Cu core | Ag shell | Cu core | Ag shell |
| **Cu (at. %)** | 97.9±3.0 | 11.7±2.2 | 89.4±3.5 | 11.8±1.5 | 99.9±0.1 | 28.0±8.1 |
| **Ag (at. %)** | 2.1±3.0 | 88.3±2.2 | 10.6±3.5 | 88.2±1.5 | 0.1±0.1 | 72.0±8.1 |

Figures 3.5 – 3.7 show the results of NMF decompositions to extract chemical phases from EDX maps of the particles in figure 3.4. The left columns show the loadings (spatial distributions) of the factors (spectral components) in the right columns, similar to the original EDX maps. The difference is that the factors, being linear combinations of EDX channels, can be interpreted as correlating with chemical phases in the particles. This makes it possible to "separate" overlapping phases. A good example of this is the separation of the particle phases from the background component, most clearly seen for the particles compacted at 750 °C and 850 °C (figures 3.5 and 3.6). The background

component contains mostly carbon originating from the carbon support on the TEM grid. Note that the Au signals that show up in several of the factors also originate from the TEM grids. At 850 °C and 950 °C, Ag rich components that overlap with Cu rich components are separated, in support of surface segregation leading to the core-shell morphologies. From the information in the spectral components, we can quantify the composition of the Cu and Ag rich components, summarized in table 3.2.

Interestingly, the data in table 3.2 suggests stronger segregation between Cu and Ag at 750 °C than 850 °C, where there is more Ag present in the Cu core. At 950 °C, the Cu core loses virtually all Ag, which could be a consequence of Ag evaporation, but also due to a compositional trend in surface segregation in bimetallic NPs that will be discussed in the next section. The higher Cu content in the Ag phases is in line with XRD measurements on spark ablation generated CuAg agglomerates [74]. It is likely that NMF is more accurate in quantifying the composition in the shell phases than the core phases, since there is no overlap with the core phases at the edges of the shells.

### 3.2.3 Surface segregation mechanisms

The formation of quasi-Janus and core-shell Cu-Ag NPs by in-flight sintering of CuAg agglomerates made by spark ablation is attributed to surface segregation, where specifically Ag migrates toward the surface of the particles. Gas phase techniques in general, and perhaps aerosol technology in particular, are well-suited to study these processes with a controllable influence from the gas (or lack thereof) and without an influence from a substrate.

Producing controlled heterogeneous NPs via surface segregation in the aerosol phase, however, requires tinkering in the material combinations. To achieve strong heterogeneity, the material combinations need to have low miscibility as in the case of CuAg. A general observation in immiscible bimetallic NP systems is that the element with the larger atomic radius and lower surface energy tends to occupy the surface [82]. The impact of surface energy is rather intuitive in the context of minimizing total energy of the system. A macroscopic analogue to the atomic radii trend can be made with granular convection, also known is the muesli effect: shaking a packet of muesli will make larger pieces migrate upwards (toward the surface). Cu and Ag obey this trend: they have atomic radii of 2.17 Å and 2.25 Å [83], and surface energies of $2.13\ J / m^2$ and $1.21\ J / m^2$ [84] respectively.

MD and Monte Carlo simulations applied to a library of bimetallic NP combinations found that the (difference in) cohesive energy, which essentially is the heat of sublimation [85] and is correlated to surface energy, and Wigner-Seitz radius (another

definition of atomic radius) are the most influential factors in determining segregation of the constituent elements [86]: the element with the higher cohesive energy often has a smaller Wigner-Seitz radius and will tend to be the core preferring element. These trends are also consistent with the CuAg system. The simulations in Ref. [86] on varied bimetallic compositions showed that as the surface preferring element decreased in the NP, the shell becomes more mixed, while the core becomes more pure. Interestingly, this is supported by the core and shell compositions determined NMF decomposition in table 3.2, where the NPs compacted at 950 °C have a more mixed shell and purer core.

Since we are dealing with nanoscopic systems, a natural question is how the size of the NPs may affect surface segregation. In Ref. [86], the higher surface to volume ratio in smaller NPs indicated that smaller NPs obtained patchier (more mixed) shells, and purer cores. The commonly known phenomenon of melting point suppression in NPs [65, 87, 88], where decreasing NP diameter leads to a lower melting temperature, is also suggested to have analogue effects in quantities like surface energy and cohesive energy [85, 89]. Depending on the relative decrease of cohesive energy in the core and shell preferring elements, this could affect the segregation and chemical ordering in NPs smaller than about 10 nm. On the other hand, Nanda et al. argued and experimentally showed a higher surface energy of free NPs [90]. Certainly, this observation may have impacts on surface segregation tendencies in free NPs that aerosol technology has a unique position to study with precise size-selection.

# 4 Condensational growth

Condensation is a ubiquitous phenomenon in aerosol science. It is one of the main mechanisms for growth of aerosol particles in the atmosphere, including the formation of clouds from water vapor [19, 20]. In CPCs, condensation is critical to detect NPs. We have already briefly encountered the topic of condensation in engineered aerosol NPs, where we stated that nucleated particles larger than some critical diameter will continue to grow by condensation (as long as there is a supersaturation of the condensing vapor). The formation of NPs in spark ablation falls under homogeneous nucleation, where particles form spontaneously from supersaturated vapors. In an already present aerosol, growth by condensation is also called heterogeneous nucleation, and can occur at much lower supersaturations as the presence of stable particles act as seeds for vapor precipitation and continued growth.

In aerosol technology, we can exploit heterogeneous nucleation to form heterogeneous NPs by condensing one material onto an aerosol of existing NPs. This sequential form of processing is perhaps the most intuitive way to synthesize core-shell particles, and is a common approach in both chemical and physical synthesis. Physical gas-phase methods are attractive due to the possibility to obtain high-purity product without waste from solvents and chemical byproducts. Magnetron gas aggregation techniques have demonstrated excellent tunability of core/shell size and shapes [91]. They are, however, technologically demanding, requiring stringent vacuum control [92] and the produced nanoparticles may often contain metastable phases due to the fast quenching processes involved [93, 94]. The ambient nature of aerosol technology with carrier gas transportation of the NPs allows for sequential processing steps like sintering and size distribution measurements, which is difficult in vacuum systems [54]. Compared to surface-segregation that requires certain properties of the present elements, condensational growth to obtain heterogeneous NPs in the aerosol phase is theoretically more flexible in terms of material choice.

This section deals with condensational growth of core NPs made with spark ablation to create core-shell NPs. We use two approaches to accomplish condensational growth: thermal evaporation and photolysis. Thermal evaporation, which is the methodology used in **Paper III**, is technologically simple and is similar to how condensation works

in the atmosphere, where thermal gradients cause supersaturation of a vapor that condenses on an aerosol. To avoid alloying between core and shell materials, we have designed a thermal evaporator with a local heating element, and we have characterized the growth with a simple free-molecular condensation model taking into account the empirical residence time distribution of the NPs. Thermal gradients that inevitably lead to some particle losses from thermophoretic deposition are completely avoided in photolysis, where a UV light triggers condensation of a light-sensitive molecule, like metal-organic precursors, onto core NPs. Here, we have used TMIn, which is a commonly used precursor in crystal growth, as the photolytic precursor. We test the process by condensing In shells on Au particles, a combination that normally would be expected to alloy at elevated temperatures. While photolysis introduces chemical precursors to an otherwise physical process, it offers opportunities to relatively easily combine core and shell materials that otherwise would be difficult to obtain in thermal evaporation processes.

## 4.1 Condensation on nanoparticles

The general condensation process in the gas phase is obtained from kinetic gas theory: the growth is the net arrival of atoms or molecules from the gas phase on the surface of the particles. As alluded to in chapter 2, the mass transfer depends on the size of the particle, $d_p$, relative to the MFP of the condensate, $\lambda$, which is characterised by the Knudsen number, Kn. If the particles are significantly smaller than the MFP of the condensing species, such that Kn >> 1, the condensation is said to occur in the free-molecular regime. In most cases, however, we usually find ourselves in between the free-molecular regime, and the other end where Kn < 1, called the continuum regime. Since we are dealing with NPs generally smaller than the MFP of the condensing species, we will here for simplicity assume we are in the free-molecular regime.

In the free-molecular regime the expression for the average arrival of condensing atoms is, in fact, the same as the evaporation from a surface (equation (3.1)):

$$c = \frac{p_v}{\sqrt{2\pi m k_B T}} \tag{4.1}$$

Where $p_v$ and $m$ are the vapor pressure and mass of the impinging species. The net arrival of atoms onto a particle with surface area $d_p^2\pi$ is the above expression minus eventual evaporation from the particle surface:

$$n = \frac{d_p^2 \pi (p_v - p_d)}{\sqrt{2\pi m k_B T}} \tag{4.2}$$

Where $p_d$ is the vapor pressure of the condensing species over the particle surface. We realize that $p_d$ must be smaller than $p_v$ for net growth. Just as in the case of nucleation, we require a supersaturation to have condensation. The supersaturation can be realized in different ways. In thermal evaporation processes, supersaturation is obtained by a thermal gradient: as the evaporated species cools in the presence of particles, the supersaturation can lead to both heterogeneous condensation, *i.e.*, growth of the particles, and homogeneous nucleation, *i.e.*, formation of new particles. In photolysis, the photon flux leads to photodissociation of precursors and supersaturations generally not obtainable in thermal evaporation, which will be described later.

We can consider the volume change of a particle with diameter $d_p$ by the net arrival of gas phase species times their volume, $v_m$:

$$\frac{dv_p}{dt} = n v_m \tag{4.3}$$

$$v_m = M \,/\, \rho N_A \tag{4.4}$$

Where $M$ and $\rho$ are the molar mass and density of the condensing species and $N_A$ is Avogadro's number. We can rearrange the volume change to obtain the particle diameter growth rate $dd_p \,/\, dt$.

$$\frac{dv_p}{dt} = \underbrace{\frac{dv_p}{dd_p}}_{=d_p^2\pi/2} \times \frac{dd_p}{dt} = \frac{d_p^2 \pi M (p_v - p_d)}{\rho N_A \sqrt{2\pi m k_B T}} \tag{4.5}$$

$$\frac{dd_p}{dt} = \frac{2M(p_v - p_d)}{\rho N_A \sqrt{2m\pi k_B T}} \tag{4.6}$$

For NPs smaller than ca. 10 nm, $p_d$ should be evaluated with the Kelvin ratio (equation (2.13)). However, in the case where we have supersaturation, we can often neglect re-evaporation from the particles, and $p_d$ drops out. Interestingly, the diameter dependence cancels out in in equation (4.6), meaning all NPs growing in the free-molecular regime have the same increase in diameter. This is an important characteristic of free-molecular condensation.

In a region of constant supersaturation, we can finally express the grown particle diameter by simply multiplying equation (4.6) with the duration $t$ of condensation:

$$d_p = d_{p0} + \frac{2Mp_v}{\rho N_A \sqrt{2m\pi k_B T}} \times t \quad (4.7)$$

## 4.2 Condensation by thermal evaporation

As mentioned in the previous section, condensational growth of aerosol particles by thermal evaporation is a simple approach to create bimetallic NPs, including core-shell NPs. Historically, thermal evaporation has also been important in creating metallic aerosol NPs. However, the large, continuous energy consumption for maintaining high enough temperatures for metal evaporation, and the difficulty in controlling composition stemming from different evaporation rates in metals, make thermal evaporation less suited than spark ablation for generating bimetallic and multimetallic NPs.

For condensation by thermal evaporation, an aerosol of core particles can simply be introduced to, for instance, a tube furnace that evaporates the condensing material. This has previously been done to grow Ga on Au aerosol particles [95] and to deposit Ag and Au on metal-oxide particles [96, 97]. The issue with this approach is that if the core and shell materials are miscible, there will likely be alloying between the constituents. If the core material has a similar or higher vapor pressure than the shell material, the core material will also evaporate during the coating process. An alternative approach is the use of a hot-wire evaporator that heats only a wire consisting of the material that will be condensing on the aerosol [97]. While hot-wire evaporation can generally reduce heating the core aerosol NPs, the wires need to be carefully designed: they must not easily melt, which can be managed by coating the evaporating material onto a wire of a heat resistant material. In our work, we have set out to construct a thermal evaporator that, similar to a tube furnace, can evaporate arbitrary material slabs but does not thermalize the entire aerosol.

A schematic design of the thermal evaporator is shown in figure 4.1. The evaporator is a vertically oriented stainless-steel tube with a conical top, a bottom heater, and angled inlets. The purpose of the angled inlets and the conical tube is to promote swirl-like trajectories of the incoming aerosol NPs in a laminar flow, which was simulated with COMSOL Multiphysics (figure 4.1 B). The position of the small bottom heater focuses heating on the evaporating material, and the thermal gradient in the direction of the carrier gas flow should reduce particle losses by momentum transfer from hotter gas to cooler regions, known as thermophoresis.

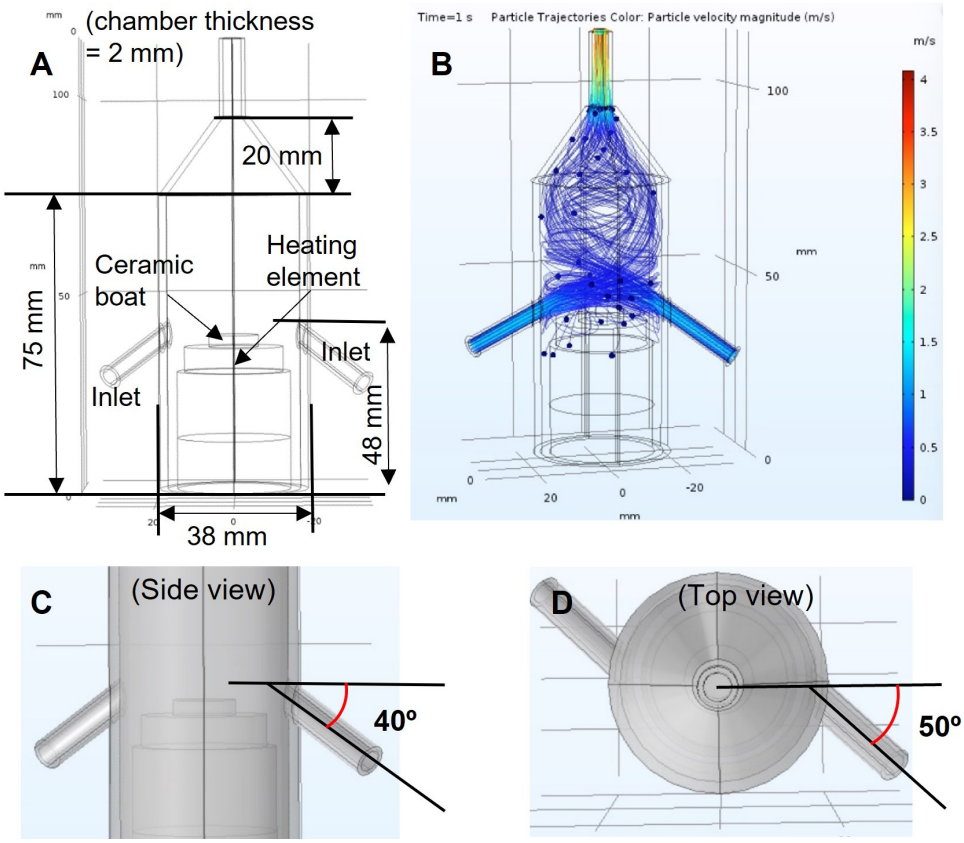


**Figure 4.1.**
Schematic of the thermal evaporator chamber design (A). An example of particle trajectories and velocities through the chamber simulated by COMSOL Multiphysics (B). Inlet angles to the chamber as seen from side view (C) and top view (D).

COMSOL simulated time-temperature history of particles traversing through the evaporator at different heater temperatures is shown in figure 4.2. Since the particle temperatures are significantly lower than the heated element in the bottom of the chamber, these simulations indicate a decoupling from heater and aerosol temperature that should promote the formation of core-shell morphologies in condensational growth.

To test and characterize condensational growth in the evaporator, we have evaporated Zn onto core particles of Au, Sn and Bi synthesized with spark ablation. Similar to the generation of CuAg NPs, a 95 % $N_2$: 5 % $H_2$ carrier gas mixture was used to generate the NPs, as that has been shown to reduce oxidation of Sn and Bi in aerosol synthesis [75]. Zn was chosen due to its exceptionally high vapor pressure [66] (figure 3.2),

although other materials can be used in principle. Au-Zn is a miscible material system [98], whereas Au-Sn and Au-Bi are strongly segregating [99-101]. The material combinations thus represent both challenging systems that we expect to alloy in a tube furnace (Au-Zn) and systems we expect to segregate (Sn-Zn and Bi-Zn).

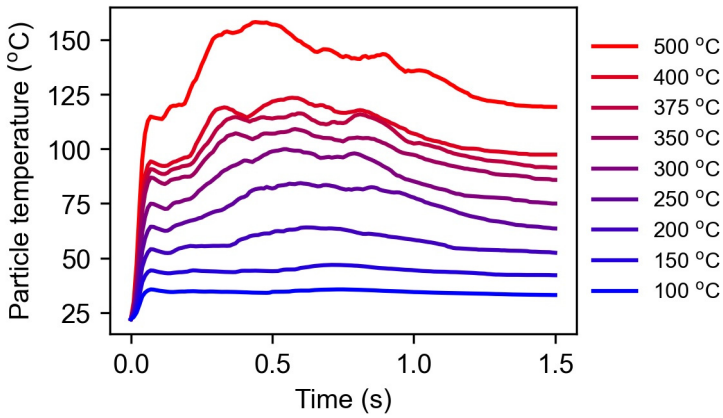


**Figure 4.2.**
COMSOL simulated particle time-temperature history inside the evaporation chamber at different heater temperatures.

Experimentally, a growth of core aerosol particles by condensation can be seen as a shift in the size distribution toward higher mobility diameters. Figure 4.3 shows the experimental setup used to monitor this. The setup employs a tandem DMA setup, as described in Chapter 3. After aerosol NPs of a core material has been made by spark ablation, the first DMA, DMA1, and the tube furnace are used to size-select a monodisperse population of compacted core NPs that then enter the evaporator. The second DMA, DMA2, and the electrometer are used to monitor the aerosol size distribution and changes thereof, for example due to condensational growth.

Figure 4.4 shows the size distributions of an aerosol of 20 nm size-selected and compacted Au NPs introduced to the evaporator at varying heater temperatures. At room temperature, we see the original Au distribution centered around a mobility diameter of 20 nm. When the heater temperature in the evaporator is increased, the size distributions shift and broaden initially to larger mobility diameters, followed by a shift back to smaller mobility diameters. The mode mobility diameters and geometric standard deviations (GSD) of the size distributions are summarized in the inset.

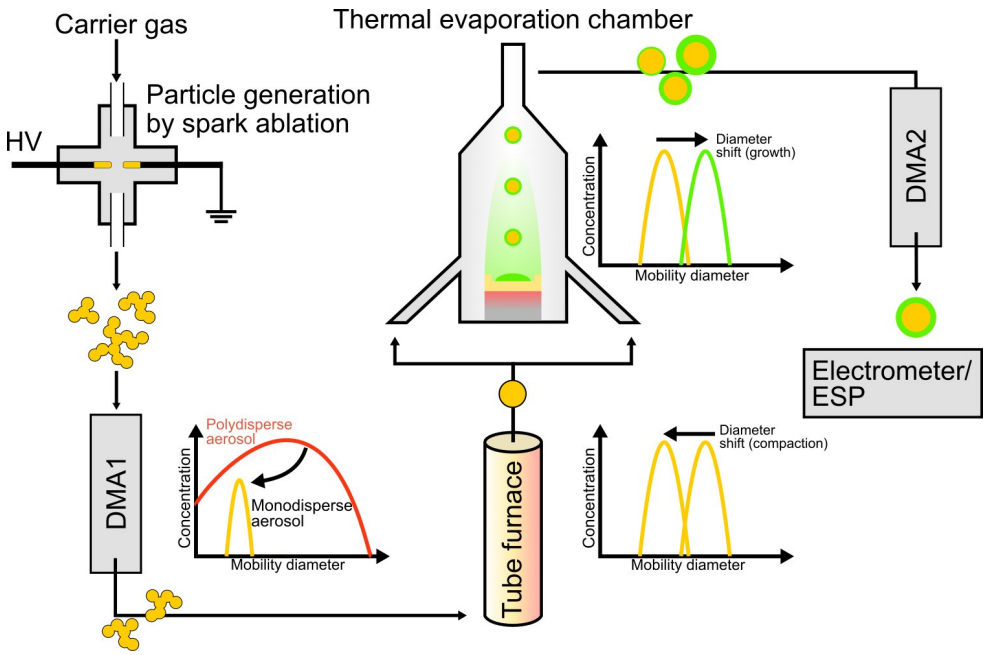


**Figure 4.3.**
Thermal evaporation setup. An aerosol generated by spark ablation is first size-selected by DMA1 and then compacted with a tube furnace before entering the custom thermal evaporator. Condensational growth of the evaporated material, in this case Zn, is monitored as a shift in the mobility diameter distribution, measured with DMA2 and an electrometer.

The increase in mode diameter is expected from condensational growth, whereas the decrease has also previously been observed from Ga condensation on Au particles [95] and is attributed to homogeneous nucleation of the condensing species, which is Zn in our case. This occurs due to the thermal gradient and supersaturation that increases with increasing heater temperature. Homogeneous nucleation scavenges Zn from the gas phase and is a competitive mechanism to condensation. In the work of Karlsson et al. [95], further increases to their tube furnace temperature lead to an increase in homogeneously nucleated particle concentration until the core particles could grow by coagulation rather than only by condensation. A similar behavior is hypothesized in our setup for even higher evaporation temperatures. Note that because these Zn particles are uncharged, they are not detected by the electrometer, and hence do not show up in the size distribution traces.

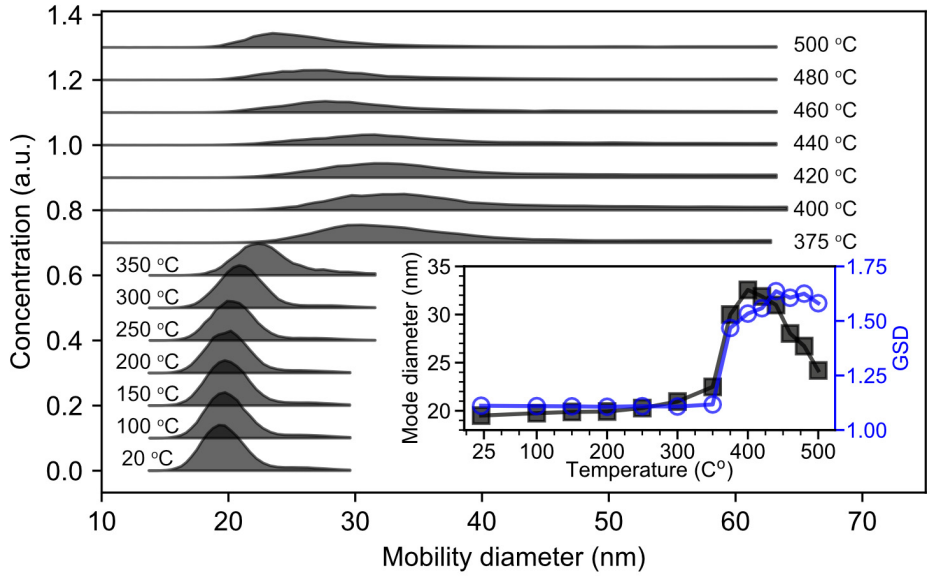


**Figure 4.4.**
Tandem DMA measurements of Au aerosol mobility diameter size deistributions at different evaporator temperatures (grey filled traces). The inset shows the mode diameter and GSD of the traces.

### 4.2.1 Aerosol residence time distribution in the evaporator

As discussed in section 4.1, condensational growth in the free-molecular regime implies a linear growth rate, such that all NPs have the same diameter increase. To test this, we condensed a few nm of Zn onto Au particles of varying core diameters and studied the shift in mode mobility diameter. Figure 4.5 shows there is no clear trend in core particle growth with increasing core diameter, which is indicative of free-molecular condensation. Similarly, we would expect the entire aerosol size distribution to maintain its shape and to shift linearly toward larger mobility diameters during condensational growth in the evaporator. However, figure 4.4 clearly shows that the size distributions shift and broaden with increasing evaporator temperatures. The broadening in the size distributions is tracked with their respective GSD.

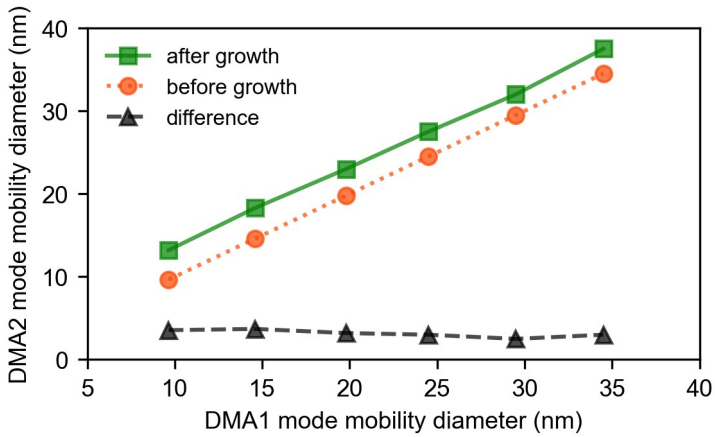


**Figure 4.5.**
Zn condensation on Au core particles between 10 nm to 35 nm shows that the growth rate is not dependent on core particle diameter, indicative of condensational growth in the free-molecular regime.

We aim to explain this observation in broadening of the size distributions by the concept of a residence time distribution (RTD) of NPs in the evaporator. Inside the reactor, a particle may take different paths leading to different residence times. A particle staying for a longer time inside the evaporator will undergo more condensational growth than a particle that exits the evaporator quicker. If we were conceptually to track many particles, a "pattern" of residence times with corresponding probabilities would emerge, which we call the RTD.

The RTD in an important concept in chemical reactor engineering to understand variations in the product due to varying reaction times species inside a reactor experience, and theories for measuring the empirical RTDs and estimating ideal theoretical RTDs in reactors have been developed [102]. Here, we will use the same theory to measure the RTD in our custom thermal evaporator. In chemical reactor engineering, the empirical RTD $E(t)$ can be measured by injecting a tracer of a known concentration into the reactor and measuring the temporal concentration response after the reactor. The relation between the injected tracer concentration, $c_{in}(t)$, and the measured tracer concentration after the reactor, $c_{out}(t)$, is described by a convolution [102]:

$$c_{out}(t) = \int_0^t c_{in}(t - t')E(t')dt' \qquad (4.8)$$

Where $E(t)$ is the RTD. If $c_{in}(t)$ is a step function with some amplitude $c_0$, it is trivial to obtain the RTD by differentiating equation (4.8):

$$c_{in}(t) = \begin{cases} 0, & t < 0 \\ c_0, & t \geq 0 \end{cases} \tag{4.9}$$

$$c_{out}(t) = c_0 \int_0^t E(t')dt' \rightarrow E(t) = \frac{d}{dt}\left(\frac{c_{out}(t)}{c_0}\right) \tag{4.10}$$

In this work, we use a new approach to measure the empirical residence time of aerosol NPs in the evaporator. Instead of dedicated tracer measurements, which can be complicated to acquire and set up, we use the NPs themselves as tracers. The setup used to accomplish this is depicted in figure 4.6. Briefly, a step function-like concentration $c_{in}(t)$ of aerosol NPs can be realized by bypassing a HEPA filter prior to the evaporator. The spark ablation particulate output is first allowed to stabilize with respect to particle concentration for some time before a measurement. 20 nm Au particles are size-selected with DMA1 and compacted to spherical NPs in the tube furnace prior to the HEPA filter. When the HEPA filter is bypassed, $c_{in}(t)$ goes from 0 to some concentration $c_0$ essentially immediately, mimicking a step-function. The aerosol concentration after the evaporator, $c_{out}(t)$, is measured as a function of time with the electrometer.

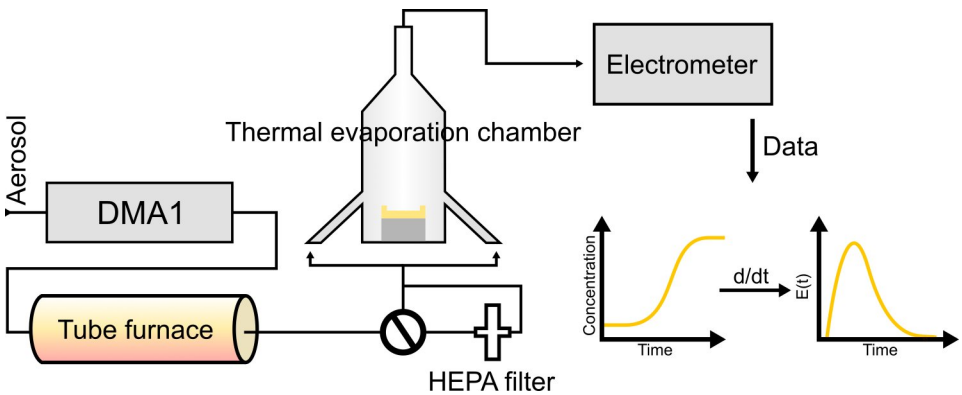


**Figure 4.6.**
Schematic of setup to measure the residence time distribution inside the thermal evaporation chamber. A stable concentration of size-selected and compacted Au nanoparticles are injected to the thermal evaporation chamber by bypassing a HEPA filter. The concentration response is measured by an electrometer.

An example obtaining $E(t)$ from differentiating measurements of $c_{out}(t)$ is shown in figure 4.7. $c_{out}(t)$, corresponding to the electrometer signal (left panel in figure 4.7), was first smoothed with a moving average filter before differentiation. An exponentially modified Gaussian (EMG) function was used to model the RTD (right panel in figure 4.7). The mean of the EMG was found to be significantly longer than the residence time simulated with COMSOL. Interestingly, the mean of the Gaussian part (table

4.1) is similar to the COMSOL simulated residence time of particles in the evaporator (figure 4.2).

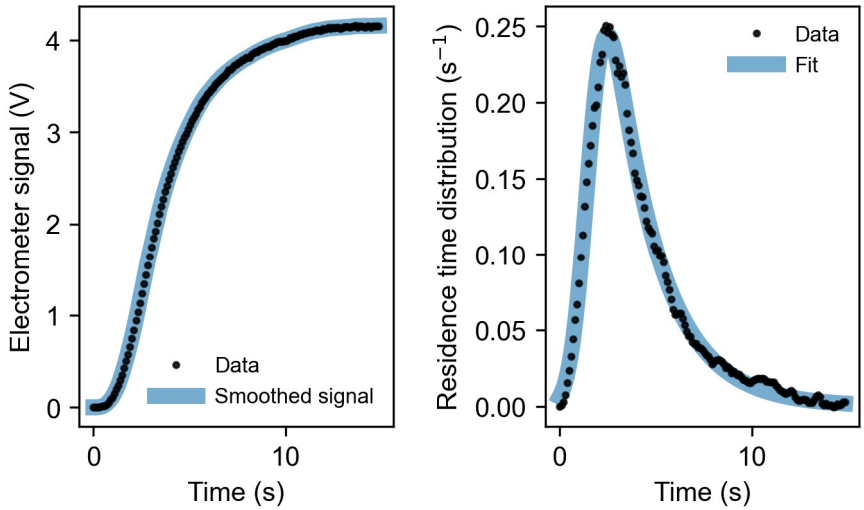


**Figure 4.7.**
Measurements of aerosol nanoparticle RTD in the evaporator at room temperature. The electrometer signal and smoothed data (left panel), proportional to the time dependent aerosol concentration exiting the evaporator, are differentiated to obtain the RTD (right panel). The RTD has been fitted with an exponentially modified Gaussian function.

**Table 4.1.**
Average best parameter values of exponentially modified Gaussian fits. $\mu$ and $\sigma$ are the mean and standard deviation of the Gaussian, and $\lambda$ is the exponential rate.

| $\boldsymbol{\mu}$**(s)** | $\boldsymbol{\sigma}$**(s)** | $\boldsymbol{\lambda}$**(s$^{-1}$)** | **Mean=$\mu + 1/\lambda$ (s)** |
|---|---|---|---|
| 1.59 | 0.81 | 0.39 | 4.15 |

The EMG models the empirical RTD data quite well. With this fitted function, we can now modify the condensational growth equation (4.7) to accommodate for a stochastic NP residence time:

$$d_p = d_{p0} + \frac{2Mp_v}{\rho N_A \sqrt{2m\pi k_B T}} \times \tau \qquad (4.11)$$

Where $\tau$ is the randomly distributed time variable realized by the RTD, which here is the EMG with the parameters in table 4.1. Using equation (4.11), we can model the observed changes in size distribution data to solve for the effective growth rate inside the evaporator. Figure 4.8 shows the best fits obtained by applying equation (4.11) to

the original Au size distribution data, *i.e.,* the bottom size distribution trace in figure 4.4. The empirical RTD in equation (4.11) can fit the observed changes to the size distributions from growth in the evaporator well, supporting the theory of condensational growth in a chamber with a broad RTD. The results obtained here indicate that condensational growth is the dominating growth mechanism, even in the presence of homogeneous nucleation of Zn that likely is the cause to the observed decreasing growth rates at higher temperatures. We reiterate that continuing to increase the evaporator temperature could eventually lead to further core particle growth by coagulation with homogeneously nucleated Zn NPs.

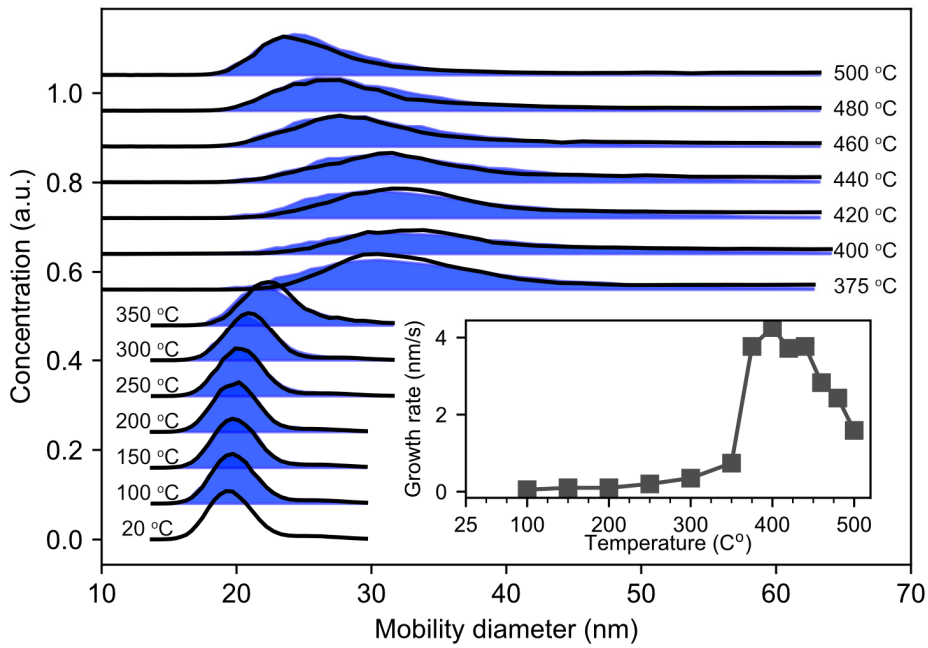


**Figure 4.8.**
Tandem DMA measurements of Au aerosol mobility diameter distributions (black traces) and simulated growth based on empirical residence time distribution (blue fills) applied the room temperature Au aerosol distribution (bottom trace). The inset shows the best fit growth rate as a function of temperature.

### 4.2.2 Shell structure

Electron microscopy of Au, Bi and Sn particles synthesized with a target Zn shell thickness of 5 nm, corresponding to a mobility diameter increase of ca. 10 nm reveals the shell formation in all three material systems.

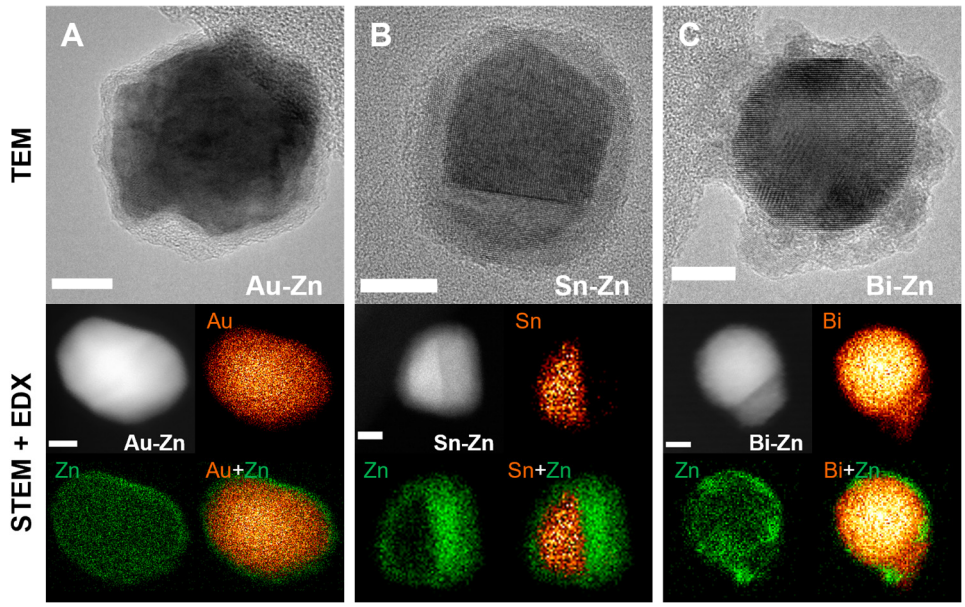


**Figure 4.9.**
Electron microscopy investigations of Au-Zn (A), Sn-Zn (B) and Bi-Zn (C) nanoparticles. TEM micrographs in the top row reveal a core-shell formation in all material systems, supported by elemental maps obtained by STEM-EDX, shown in the bottom row. Scalebars are 10 nm.

If we consider an "ideal" core-shell structure of a spherical core and shell, we can estimate an equivalent shell thickness $t_{\text{shell}}$ from micrographs using the following equation:

$$t_{\text{shell}} = \sqrt{A_{\text{particle}}/\pi} - \sqrt{A_{\text{core}}/\pi} \qquad (4.12)$$

Where $A_{\text{particle}}$ and $A_{\text{core}}$ are the projected equivalent circular areas of the entire particle and core particle, respectively. Using equation (4.12) on NP areas measured from TEM micrographs, we find Zn shell thicknesses of 2.7±0.4 nm for Au-Zn, 5.8±2.9 nm for Sn-Zn and 6.3±1.4 nm for Bi-Zn. The estimated Zn shell thicknesses are close to the DMA mobility diameter increase for Sn-Zn and Bi-Zn, but is slightly thinner than expected for Au-Zn. The core-shell morphology is particularly interesting for the Au-Zn shell, which is the miscible system, that indicates a difference in particle and evaporation temperature predicted by the COMSOL simulations in figure 4.2. However, the smaller shell thickness obtained from TEM micrograph measurements

could be due to partial alloying of Zn with Au due to the increased temperature of the core Au particles.

While the structure of the shell for certain Bi-Zn NPs looks like it could be formed by coagulation with smaller Zn particles (*e.g.,* the particle in figure 4.9), it can also be explained by the difference in surface energy of the core and the shell [54]. Briefly, there is a tendency to form a cohesive, smooth shell if the shell surface energy is lower than that of the core and the interface between core and shell:

$$\gamma_{\text{core}} + \gamma_{\text{core-shell}} > \gamma_{\text{shell}} \tag{4.13}$$

If the inequality is reversed, it is not energetically favorable to form a cohesive shell. Instead, the shell tends to form islands on the core, creating a "patchy" shell.

$$\gamma_{\text{core}} + \gamma_{\text{core-shell}} < \gamma_{\text{shell}} \tag{4.14}$$

Comparing tabulated values of surface energies for Au, Sn, Bi and Zn (table 4.2), the surface energy inequalities suggest it is plausible for Au-Zn to form cohesive shells in accordance with equation (4.13) if the interface term is sufficiently small. Sn-Zn and Bi-Zn, on the other hand, should prefer the "patchy shell" morphology, which seems to be the case for Bi-Zn. Complementary elemental maps on smaller Bi-Zn NPs, with core diameters of 9 – 12 nm, however, reveal more cohesive shells (figure 4.10). This observation could be due to changes in surface energy of the Bi core and Bi-Zn interface for smaller NPs in the gas phase [90]: an increased surface energy of free NPs could reverse the surface energy balance in the Bi-Zn case, allowing for the growth of cohesive Zn shells on smaller Bi NPs.

**Table 4.2.**
Experimental values of surface energies for Au, Sn, Bi and Zn.

| | Au | Sn | Bi | Zn |
|---|---|---|---|---|
| **Surface energy** ($J/m^2$) | 1.506 [103], 1.500 [104] | 0.675 [103], 0.709 [104] | 0.490 [103], 0.489 [104] | 0.990 [103], 0.993 [104] |

Sn-Zn shows an interesting morphology with a sharp interface between what seems to be crystalline Zn, as well as an amorphous ZnO shell. This hybrid Janus-core-shell morphology cannot be explained by the surface energy balance. It could be that the Zn first preferentially grows on one side of the Sn core until a critical thickness is exceeded and Zn grows over the rest of the Sn. It should be noted that kinetic effects, including

growth temperature and lattice mismatches between the core and shell materials, play important roles in the shell structure [54].

It is in these Sn-Zn particles with a comparatively thick Zn segment where we see crystalline Zn, whereas Zn appears mostly amorphous in the other particles. This can be explained by Zn surface oxidation when exposed to ambient conditions, which is observed in Zn NPs [105]. Looking at the bright-field TEM micrographs of the core particles, Sn and Bi appears crystalline without clear signs of surface oxidations that are otherwise typically the case for these NPs [75]. Thus, the Zn shell may act as an oxidation barrier to protect sensitive core materials from oxidation.

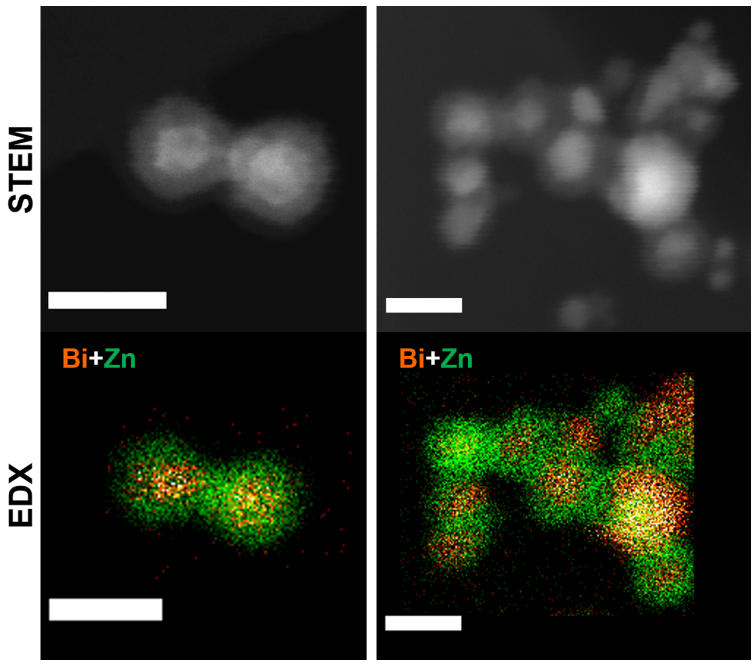


**Figure 4.10.**
Complementary STEM-EDX on smaller (9 – 12 nm) Bi-Zn nanoparticles reveal a more cohesive Zn shell structure. Scalebars are 20 nm.

## 4.3 Growth by photolysis

While thermal evaporation is a straightforward approach to achieve condensational growth and create heterogeneous nanostructures, working with high temperatures have downsides in aerosol technology. First, a lot of energy is spent on maintaining high temperature devices like tube furnaces. Second, the thermal gradients leading to

heterogeneous nucleation will likely also lead to some homogeneous nucleation that reduces condensational growth efficiency or creates new growth mechanisms (coagulation) that may compete with the condensational growth. Thermal engineering with multiple tube furnaces to reduce homogeneous nucleation makes the setups more complex and energy demanding [96]. At the very least, thermal gradients lead to particulate losses by thermophoresis, where momentum transfer from a hotter region causes deposition of particles onto a colder region. As NPs are already relatively quickly lost from deposition by diffusion in the aerosol phase, thermophoretic losses should ideally be avoided.

One strategy to avoid high temperature condensational growth is photolysis of light sensitive precursors. Photolysis is the photoactivation or photodissociation of molecules by light, typically UV radiation. A common type of molecule for photolysis is metal-organic precursors that have a central metal atom bound to some number of organic ligands, like trimethyl indium (TMIn) that has a central In atom bound to three methyl ligands. The metal-organic bonds can be broken both by high temperatures, called thermolysis, and by UV illumination in photolysis. Thermolysis is typically used with metal-organic precursors in crystal growth like metal-organic chemical vapor deposition (MOCVD). However, photolysis can be carried out at any temperature, with potential benefits for condensational growth in aerosol technology. This process is also called photo-induced CVD.

In contrast to pure metals, many metal-organic precursors have a finite (non-zero) vapor pressure at room temperature and even lower temperatures, and the metal-organic molecule concentration in a gas flow can be set by the gas flow through its container (a bubbler) and the container temperature. Upon photolysis, photodissociation of the organic ligands leads to the presence of free metal atoms in the gas phase already at room temperature, causing extreme supersaturation as the precursor concentration often is significantly higher than the equilibrium metal vapor pressure. In combination with an aerosol, this should cause condensational growth of the aerosol NPs. The room temperature processing and ability to control the metal-organic concentration separately from the aerosol provides a flexibility in choice of aerosol synthesis method, and should enable us to create structures that are not thermodynamically stable if produced simultaneously [106], like core-shell structures of miscible elements. The drawback is that we introduce chemical precursors to the otherwise comparatively clean physical processing. On the other hand, the low-temperature processing requires much less energy than thermal evaporation methods.

Boies et al. [106] demonstrated tunable $SiO_2$ coatings on Ag core particles by changing the metal-organic precursor flow and particle residence time in photoinduced CVD of a silicon containing precursor. In a similar approach, but with completely organic

precursors, Nasri Lari et al. [107], Zhang et al. [108] and Shaban et al. [109] have shown tunable polymer coatings on various core particle materials by photoinduced polymerization. To test the formation of core-shell morphologies from miscible metals, we have used photolysis to condense an In shell on Au core NP, though any core material could in principle be used, where the choice of shell material is limited by the availability of the metal-organic precursor.

### 4.3.1 Photolysis of TMIn on Au aerosol

Figure 4.11 shows the setup used to condense In onto Au core particles with UV photolysis. The Au core particles are made by spark ablation, which makes it flexible to tailor the core material by selecting the appropriate electrode material. The Au agglomerates exiting the spark ablation chamber are first compacted with a tube furnace, however, there is no size-selection prior to the optical chamber where subsequent photolysis and condensation occurs, so a rather broad size distribution of Au NPs enters the optical chamber.

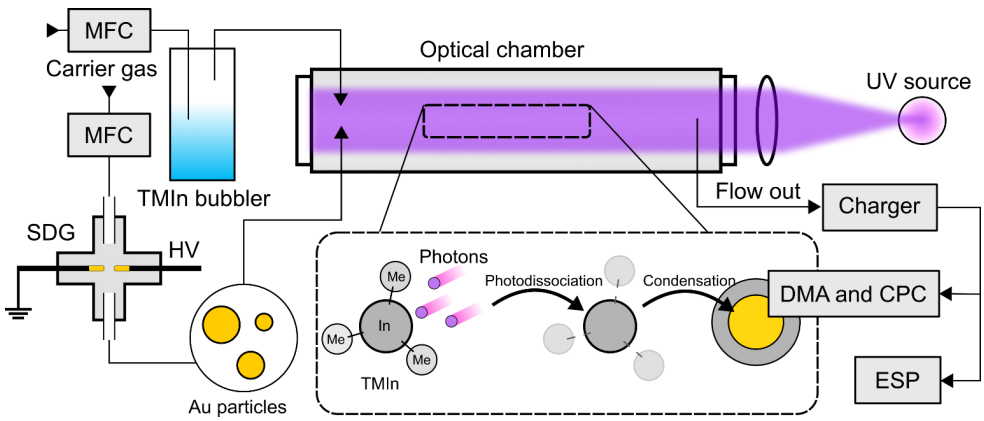


**Figure 4.11.**
TMIn photolytic condensation setup. An aerosol of compacted Au nanoparticles made with spark ablation is mixed with a flow of TMIn inside the optical chamber. A deuterium lamp is used to trigger photolysis of TMIn. The process is monitored by measuring the aerosol size distribution with a DMA and a CPC, and samples for off-line analysis are deposited with an ESP.

TMIn precursor is introduced at varying concentrations by changing the $N_2$ flow through the TMIn bubbler at flow rates $Q_{\mathrm{TMIn}}$ of 0.02 L/min, 0.04 L/min and 0.06 L/min. The aerosol flow through the spark ablation chamber is kept constant at $Q_{\mathrm{A}} =$ 0.2 L/min. The optical chamber where the photolysis takes place has a fused silica window through which UV light from a 30 W deuterium lamp is shone. The UV light

was collimated with an aperture and a fused silica lens to reduce the production of free electrons from interactions between the UV photons and the inside of the chamber.

To reduce condensation of TMIn and deposition of NPs on the optical access window, a sheath flow was introduced closest to the silica window (not shown in figure 4.11), and set to balance the total flow to 0.3 L/min that was drawn by the CPC. The photolysis process was studied on-line with a DMA and a CPC that was used to measure the evolution in the size distribution of the aerosol from the onset of photolysis. An ESP was used to deposit particle samples for off-line EM analysis.

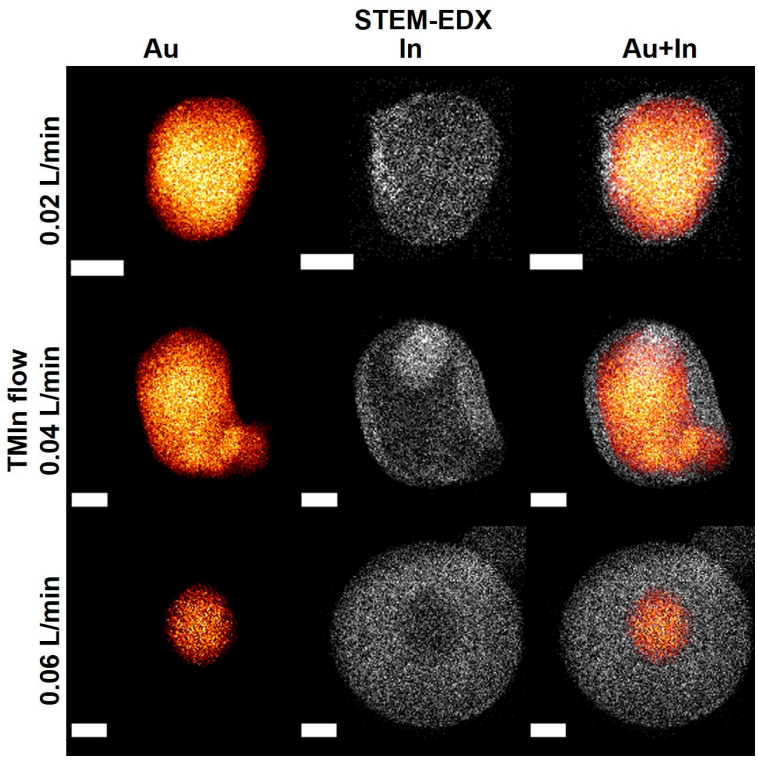


**Figure 4.12.**
STEM-EDX elemental maps of Au-In core-shell nanoparticles at TMIn precursor flows of 0.02 L/min, 0.04 L/min and 0.06 L/min. Scalebars are 20 nm.

#### *4.3.1.1 Off-line analysis: electron microscopy*

Figure 4.12 shows STEM-EDX of representative Au-In particles for the three precursor flow conditions. In all samples, we see coherent In shells forming around the Au NPs. Note that the In is likely partially oxidized due to sample handling in air. This promising data indicates that the photolysis process indeed takes place at room

temperature, and such Au-In core-shell particles are expected to be difficult to obtain using conventional thermal condensation approaches, due to the miscibility of the metals. Additionally, the low temperature processing avoids thermophoretic losses of the NPs in the optical chamber.

The general trend of the elemental maps is that the In shell thickness increases with higher precursor flow. However, if we consider additional EM micrographs of the sample made with the highest TMIn precursor flow (0.06 L/min) we see a lot of variability in the particles. Some Au particles have a thin shell, while others a much thicker shell (see figure 4.13). We also see pure In particles that are amorphous, in contrast to the crystalline Au, further confirming the low temperature the condensation takes place in. The pure In particles are from homogeneous nucleation of In due to the high supersaturation in the photolysis process, and their concentration and size also increase with a higher precursor concentration. At higher TMIn precursor concentration, there is not enough Au NP surface area to capture the supersaturated In in the gas phase. Strategies to reduce homogeneous nucleation include decreasing the precursor concentration, increasing NP surface area concentration and to tune the intensity of the UV illumination.

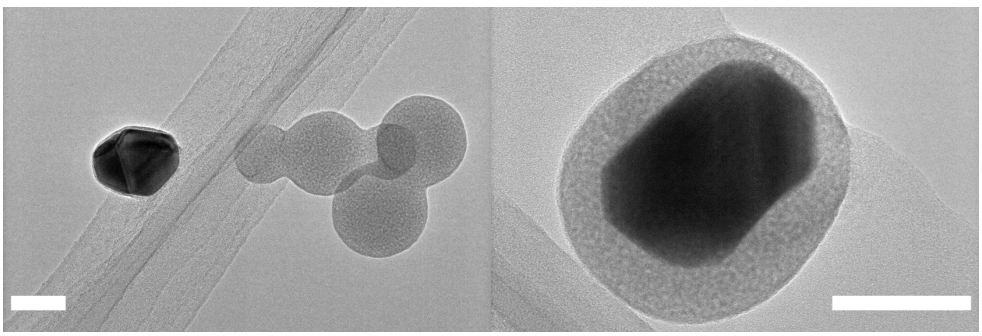

**Figure 4.13.**
TEM micrographs on Au-In particles synthesized with 0.06 L/min TMIn flow. Scalebars are 50 nm.

#### *4.3.1.2 On-line analysis: size distribution measurements*

Figure 4.14 shows the measured size distribution of the Au NPs generated by spark ablation followed by a size distribution measured 10 minutes after introducing 0.06 L/min TMIn precursor and starting UV illumination. The original Au size distribution has been fitted with a log-normal function, whose parameters will be used later to fit the subsequent size distributions measured during photolysis. The Au aerosol size distribution markedly changes during photolysis, and we have tried deconvoluting the data by fitting a number of log-normal size distributions to it. For this precursor flow,

three log-normal size distributions have been used to fit the data. The constraints put on the log-normal functions in the fit are informed by the EM data: one distribution should belong to a growing Au-In aerosol, and one distribution should correspond to larger, self-nucleated In particles. The constraints put on the Au-In aerosol is that its geometric mean diameter (GMD) may increase, but not decrease. The reasoning behind this is that from the EM we know that In condenses on Au, meaning Au particles grow and the GMD may increase. The large variability in shell thickness observed suggests it is reasonable to also let the GSD fluctuate. Since the aerosol output from the spark ablation was stable after some time, the concentration is not allowed to change much in the fitting procedure. Repeating this fitting procedure for size distributions measured at different time points, we can extract parameters like GMD, GSD and concentration, and track how they change over time, as seen in the right panel of figure 4.14.

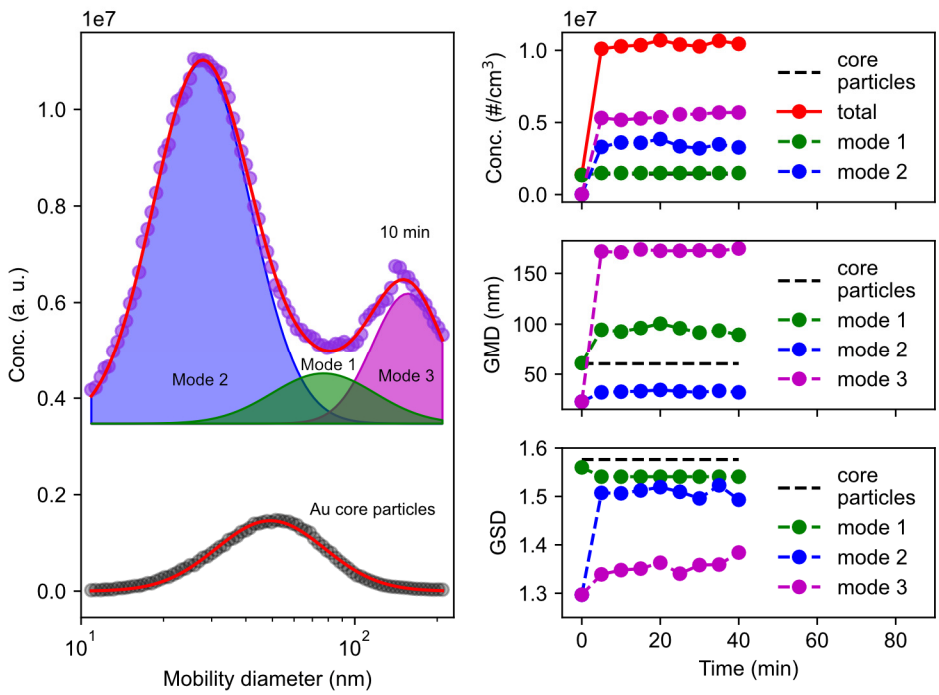


**Figure 4.14.**
Example of on-line measurement with DMA and CPC, and analysis of TMIn photolysis process.The bottom of the left panel shows a typical size distribution of compacted Au nanoparticles generated by spark ablation (dark grey dots), with a best-fit log-normal distribution (red trace). After 0.06 L/min TMIn is introduced to the flow under UV illumination, the size distribution measurement is repeated after 10 min (top trace). The size distribution data (purple dots) is deconvoluted by three log-normal distributions (filled curves, their sum is the red trace). The evolution of the concentration GMD, and GSD of these best-fit distributions is shown in the righ panel.

From the best-fit log-normal distributions in figure 4.14, we can qualitatively make comparisons to the EM data. Mode 1 and mode 3 are interpreted as an Au-In core-shell NP distribution and a self-nucleated In NP distribution, respectively. This is qualitatively corroborated by EM micrographs on the 0.06 L/min TMIn photolysis samples (figure 4.13), where we observe Au-In NPs with various In shell thicknesses, and a larger amount of pure, presumably self-nucleated In NPs. The variation in shell thickness suggests that an increase in the GSD is to be expected, but as can be seen in figure 4.14, the GSD of the Au-In distribution (mode 1) has a small decrease after the onset of photolysis. Care must be taken when interpreting fits to this data, as the search space for fitting three log-normal distributions is large, and thus requires informed constraints as those we have imposed. Unfortunately, quantitative comparisons between the mobility analysis and EM data are considerable more difficult: due to the diameter dependence in the surface concentration of ESP deposited NPs (equation 2.17), there is a bias towards a relatively higher surface concentration of smaller NPs. Interestingly, we do not observe the large population of particles corresponding to mode 2 in figure 4.14 in the EM characterization. We suspect these particles are semi-volatile compounds consisting of organics from the TMIn photodissociation process that do not survive handling in air or the vacuum inside the microscopes. Further experiments are required to confirm the characteristics of these particles. For instance, a catalytic stripper placed between the optical chamber and the DMA could be used to test the hypothesis of the volatility of these compounds.

To the best of our knowledge, this is the first time photolytic condensation onto aerosol NPs has been used with group III metal-organic precursors like TMIn. These results show promise for realizing heterogeneous NPs that are expected to mix at elevated temperatures, thanks to the room temperature processing. By controlling the precursor flow, we demonstrated a tunability in In shell thickness. The extreme supersaturations attainable by photolysis do, however, pose challenges for avoiding homogeneous nucleation of In particles that becomes more prominent with higher precursors flows. Here, we require further experimentation of different flows, NP core sizes and concentrations, UV light intensities and chamber designs to optimize coating of the particles and reduce homogeneous nucleation.

# 5 Conclusions and outlook

This thesis has explored and developed aerosol technology methods to create and characterize heterogeneous bimetallic NPs, including core-shell and Janus NPs. Heterogeneous NPs show promise in many applications as they offer unprecedented tunability in properties by varying *e.g.,* the amount and composition of the present phases, and their chemical ordering. The core-shell structure is useful to shield the core particle from the outside and retain its properties [4, 5], or, inversely, to protect the environment from the core, which is important in biomedical applications [9, 10, 110]. It is also convenient for combining different functionalities into the same structure by using materials with certain physical properties [12-14]. The compositional anisotropy in Janus NPs likewise find applications where the different faces can incorporate multiple and enhanced particle functionalities. An interesting use-cases is in catalytic self-propulsion [111], where a chemical reaction on one side of the nanostructure induces a directional movement of the particle. The nanoscale interfaces make Janus NPs particularly useful in photocatalysis to enhance photon absorption and charge transfer [16, 17].

Aerosol technology hold certain benefits over conventional strategies, like batch chemical synthesis, for creating these exciting structures. The two main advantages of aerosol technology are continuous processing and ambient pressure conditions. Continuous processing allows us to monitor and actuate processes in situ, enabling rapid diagnosis to study and optimize the synthesis to obtain the desired products. Aerosol metrology, especially size distribution measurements, are crucial to characterize many processes affecting aerosol NPs. The benefits of ambient pressure processing include avoiding expensive vacuum or high-pressure equipment, and a controllable atmosphere to reduce contamination of NPs from *e.g.,* solvents [18]. Moreover, physical synthesis without chemical precursors, including spark ablation, does not produce toxic chemical waste or byproducts.

Regardless of application, the yield of NPs produced by aerosol technology needs to be high enough for practical use. In many cases, it is further desirable to produce NPs of similar size, *i.e.,* NPs with a monodisperse size distribution. Some important challenges aerosol technology faces for large scale synthesis are related to process control and

efficiency. Given enough time, the diffusion of small NPs leads to wide size distributions from coagulation, and particle losses by, for instance, diffusional deposition. One solution to these issues is to dilute the aerosol and to have as short processing time as possible. At first glance, it seems we should reduce sequential aerosol processing and manipulation steps. For instance, the low charging efficiency of NPs and a narrow transfer function in a DMA makes continuous size-selection very inefficient for high product yield. Size distribution measurements still remain important for process monitoring. Depending on the synthesis method used, it is probably more efficient to primarily tune process parameters to obtain desired size distributions.

The methods explored in this thesis, thermally induced surface segregation and condensational growth, take advantage of the continuous and ambient conditions in aerosol technology. Starting from some aerosol source, they serve to modify the aerosol to create heterogeneous NP structures with tailored composition and chemical ordering, including core-shell and Janus structures. The results in the thesis therefore advances aerosol technology by opening new approaches for creating custom nanostructures with diverse applications. The aerosol source used in this work has been spark ablation, which is a versatile technique for creating complex nanostructures without byproducts. Spark ablation's simple setup shows opportunity for larger scale production of NPs, and observables like optical emission and the discharge current can be used to control and monitor important particle properties. One of the most important properties for bimetallic heterogeneous NPs is their composition, and the thesis describes how the optical emission in spark ablation can be used to directly measure particle composition. Like all experimental methods, the ones developed in this thesis have their benefits and drawbacks, and opportunities for future work and developments will be discussed in this final chapter.

## 5.1 Process control and monitoring in spark ablation

Spark ablation is an attractive aerosol method to create NPs due to the relatively simple setup and the flexibility in electrode choice that to a large extent determines the NP composition, which is one of the most important parameters for bimetallic NPs. The method has several process parameters that can be changed to control particle production rate, and particle size and composition. For applications, the mass output is perhaps the most important variable. As discussed in section 2.3, the main strategy to increase the material output is to increase the discharge power [40, 41], through discharge frequency and/or discharge energy, without transitioning to a glow or arc

discharge [38]. Indeed, the NP production rate is linear in discharge energy and frequency [40, 41], and the maximum discharge frequency can be scaled up by electrode geometry [41], and by decoupling charging and discharging cycles with electrical switches [40].

We are of course not limited in using a single spark ablation setup for scaling up NP production. One could imagine using many setups in parallel and combining the outputs from each setup into one NP flow [112]. Parallelization can also be achieved in a single spark ablation setup with several electrode pairs connected in serial [113, 114]. In these "multi-spark" setups, a separate voltage pulse setup was used to trigger the discharges at a controlled discharge voltage independent from the main charging circuit in order to control discharge frequency and discharge energy. With twelve electrode pairs, a NP mass production rate of up to 9 g/h was demonstrated in a single setup [114]. Not only are multiple electrode pairs one way to increase mass output, but also a way to increase the fraction of energy consumed for NP production compared to a single pair of electrodes [43].

As particle production rate increases, particle-particle collision rates resulting in the formation of agglomerates with broad size distributions increase. Common strategies to limit coagulation and obtain more monodisperse NP populations involve reducing the likelihood for primary NP collision by decreasing the time particles spend in the gas phase and by diluting them. Both can be achieved with a higher carrier gas mass flow rate, which accomplishes a shorter particle residence time in a setup, and increased dilution that limits particle collisions [18]. Another way to slow down coagulation is to charge them unipolarly by injecting unipolar ions close to the electrode gap. The unipolar charges create repulsive inter-particle forces that can significantly reduce the coagulation rate [115].

It is often reported that the aerosol NPs attain the same composition as that of the electrodes. That claim is under scrutiny in Paper viii, where we have studied the literature on spark ablation and conducted extensive compositional characterization on spark synthesized AuAg NPs as a test system. It has further been observed that the composition of the NPs may change over time when using different electrodes, which could be a result of material deposition on one electrode from the opposite electrode [116]. The final NP composition can additionally be controlled by tuning the discharge characteristics, mainly *via* the circuit resistance. The drawback of changing the discharge energy partitioning by increasing the circuit resistance [48] is that the total ablated mass is decreased, although it can be advantageously used to obtain smaller NPs [46].

Compositional control in spark ablation requires on-line compositional measurements that our work on OES measurements in **Paper I** targets. With this barebones setup essentially consisting of a parabolic mirror, an optical fibre, and a relatively cheap spectrometer, we demonstrated good performance of the LASSO regression models applied to optical spectra sampled at various discharge energies. More advanced setups utilizing time and space resolved spectral measurements can provide a great detail of information about temporal and spatial plasma properties, at the cost of much more expensive and complex setups. The increased experimental complexity also leads to more complex data processing and analysis. However, there are things that can be learned and adopted from such in-depth studies. It is known, for instance, that the bremsstrahlung background is most intense at the early stages of the optical emission [117, 118]. By triggering the optical sampling at the right time, for instance by observing the discharge current/voltage, we can obtain better signal-to-background. A simple delay circuit was demonstrated by Ref. [51] for this purpose.

Other accessible approaches for improving the signal to background lie on the data-processing side. Clustering can be used to reject spectra with poor signal-to-background to optimize training set partitioning of the data to improve the calibration models [51, 119]. Automated baseline correction and automated peak detection can be implemented to first subtract the background, and to further discard information unimportant for the elements we want to detect [52, 120]. Apart from the LASSO, there are other multivariate machine learning models that are worth exploring as calibration models for these types of spectra [49].

## 5.2 Thermal compaction and surface segregation

Surface segregation has been termed a “critical issue” in electrocatalyst engineering [121], which is one of several fields where bimetallic NPs make a big impact. With the ability to control NP stoichiometry and size, and atmosphere temperature and composition, we believe the aerosol phase is ideal for studying surface segregation without influence from substrate or solvent. The flexibility of spark ablation in making different metallic NPs enables studying various bimetallic material combinations and comparing to theoretical results [86]. However, the cycle of sample deposition followed by off-line analysis like EM or other techniques is time consuming and rather expensive. It would be beneficial if we could measure NP surface composition as the particles are still suspended. While its technically possible to introduce an aerosol directly to a synchrotron for surface sensitive chemical measurements [122, 123], it is even more costly than EM.

Fortunately, there is a clever way to potentially characterize NP surface composition directly in the aerosol phase by measuring the NP electronic work function with a technique called aerosol photoemission spectroscopy. Briefly, size-selected NPs with a known charge are radiated with wavelength-selected UV light. At the onset of photoemission, *i.e.,* when the UV photon energy exceeds the electronic work function of the NP surface, the new charge state can easily be detected with an electrometer and a CPC [124, 125]. The electronic work function is a very surface sensitive quantity that depends on the material and geometry. Although it cannot be used to measure the kinetic energy of the photoelectron like other surface techniques do, it could still be an ideal method to detect and quantify surface segregation in aerosol NPs as a shift in the work function toward one element or the other. Combined with total NP compositional measurements using our OES technique, this could be a powerful technique to test surface segregation models, and to extract parameters from such models like segregation energies [121].

A drawback of any thermal treatment for gas-borne particles, be it thermal compaction or evaporation processes, is particle losses from thermophoresis. But we are not limited to using high temperature furnaces to compact particles. Recent investigations of laser sintering show promise for compacting metallic aerosol NPs [126, 127]. Lasers have a completely different set of knobs that can be turned to control compaction, most importantly wavelength, pulse repetition rate (in pulsed lasers), and laser power, which opens up new, exciting dynamics for NP restructuring processes to be explored.

Returning to the CuAg particles generated with spark ablation and thermal compaction, we believe they may find several applications. The antimicrobial properties of Cu and Ag make CuAg NPs interesting for antibacterial surfaces and coatings [128]. With some modifications, the CuAg NPs generated with spark ablation and thermal compaction may find uses in catalysis and photocatalysis. In Paper iv, we placed CuAg NPs generated by spark ablation and thermal compaction in an environmental TEM and studied the transformation from Cu to $Cu_3P$ under a phosphine atmosphere in situ. We went one step further in Paper vi where we studied the growth of ternary Ag-$Cu_3P$-GaP NPs in an environmental TEM by first converting Cu to $Cu_3P$, followed by the introduction of trimethylgallium to precipitate GaP in the $Cu_3P$ phase of the NP. $Cu_3P$ is a semiconductor made from earth-abundant materials, and the combination with a plasmonically active Ag face makes this NP system interesting in photocatalytic applications [129]. Likewise, GaP is a well-studied semiconductor that also finds interest in photocatalysis [130]. With advances in aerotaxy, which is a technique to grow semiconductor structures from reactions between metal-organic precursors and aerosol NPs [131], it should be feasible to obtain $Cu_3P$-Ag and even Ag-$Cu_3P$-GaP directly in the aerosol phase from CuAg seed NPs.

## 5.3 Condensational growth

The condensational growth of NPs is perhaps the most intuitive approach to obtain core-shell structures in the aerosol phase. The thermal evaporator chamber with a local heating element designed in this work is a step towards obtaining such segregated structures even in miscible material systems, like Au-Zn. We also demonstrated a simple setup to characterize the RTD in the chamber by measuring the transient concentration of the aerosol NPs exiting the evaporator. Knowing the RTD is useful to understand variability in the product, like the obtained shell thickness and material composition. This type of measurement approach will hopefully find use in characterizing the RTD in arbitrary instrument volumes used for aerosol modifications or measurements in aerosol science and technology.

We found that the empirical RTD combined with a linear condensational growth model captured the shift and broadening of the aerosol size distributions observed by Zn condensation in the evaporator. A more general approach to measuring the RTD involves measuring the aerosol concentration going into the chamber, $c_{in}(t)$, as well as the aerosol concentration exiting the chamber, $c_{out}(t)$. Depending on if the aerosol is charged or not, these can be measured with an electrometer or a CPC. By measuring both $c_{in}(t)$ and $c_{out}(t)$, the convolution equation connecting these quantities (equation 4.8) can more generally be solved with, for example, a Fourier or Laplace transform, at the cost of two detectors instead of one as used in our implementation.

The benefit of thermal evaporators is that a heated material holder allows for selecting other materials to evaporate than Zn, although most metals require significantly higher temperatures. Another technologically simple alternative that can obtain similar local heating of the evaporating material are hot-wire evaporators [97]. Whilst they require specially engineered wires, they can be powered by comparatively cheap power supplies. Arranging multiple wires controlled by separate power supplies should make it possible to condense separate shells sequentially or in parallel. The flexibility of metallic wires also make them convenient for arranging them in various chamber prototype designs to experimentally optimize, *e.g.,* residence time and aerosol-vapor mixing.

Local heating elements necessarily imply temperature gradients that make homogeneous nucleation of the condensing material, and thermophoretic losses of the aerosol an issue. We indirectly observed what was likely the effect of homogeneous nucleation by a decrease in the NP growth rate with increasing evaporator temperature inside the custom evaporator. Based on similar work by Karlsson et al. [95], a further increase in NP growth rate is expected by coagulation with homogeneously nucleated particles with increasing evaporator temperature. Harra et al. [96] demonstrated a

reduction in homogeneous nucleation through thermal gradient engineering with multiple heated segments in series. It is also worthwhile to study the impact of, for instance, aerosol surface area on the homogeneous nucleation and condensational growth rate. The idea here is that more aerosol surface area can suppress homogeneous nucleation of the condensing species. These types of measurements require a CPC to detect uncharged homogeneously nucleated particles.

Photolytic condensation of metal-organic precursors can, as we demonstrated, be used at room temperature to condense metallic shells onto aerosol NPs, mitigating all aforementioned issues of thermal gradients. Indeed, we were able to condense In onto Au core particles with photolysis of TMIn, forming completely segregated Au-In core-shell NPs. Some control over the shell thickness was exercised *via* the precursor flow rate, although there was a lot of variability between the particles. A case to be made against photolysis involves the introduction chemicals to an otherwise chemical-free method. As we saw in the on-line analysis of the size distributions during photolysis, a mode of small NPs emerged that could not be detected by EM. We therefore attributed this mode to semi-volatile compounds forming from the organic ligands. If such semi-volatile compounds form, they could likely be removed from the process with a catalytic stripper. Their formation, however, leads to questions regarding the purity of the condensed shell that could contain residual organics.

Regardless of what happens to the organic ligands, we believe photolytic condensation of metal-organic precursors to be a promising method to obtain heterostructures not easily achieved otherwise. An important aspect for future work is improving the coating of core particles in favor of heterogeneous nucleation. There are several opportunities to explore process parameters for this apart from the precursor flow, including the UV light intensity and the core particle surface area. The size and shape of the optical chamber is important as it influences average aerosol residence time, residence time uniformity and mixing of particles with the metal-organic precursors. We could even imagine using certain UV wavelengths for the photolysis. Wavelength-selected UV illumination opens for the opportunity of mixing several metal-organic precursors with different wavelength absorption profiles [132], and to selectively trigger their condensation by periodically varying the UV wavelength to grow core-multi shell structures.

Note that we are not limited to controlling the decomposition of the metal-organic precursors with UV light. Metal-organic precursors are easily cracked with high temperatures to form and coat aerosols [133, 134], and more commonly in crystal growth processes like MOCVD. A combination of elevated temperature, and UV illumination, could perhaps be used to better control precursor dissociation and the evaporation of semi-volatile compounds. Another promising, room temperature

method to dissociate metal-organic precursors is using corona discharge. Corona discharges are relatively simple to implement by applying a high voltage to a sharp pointed electrode, producing a non-thermal plasma and the emission of energetic electrons that interact with the precursors. Corona discharge is already a commonly used method in aerosol science to charge aerosols [19], and we believe it can also be useful for cracking metal-organic precursors to grow core-shell aerosol NPs.

One peculiar strategy to limit self-nucleation of a decomposing metal-organic precursor in presence of an aerosol is to "flip" the dissociation process: instead of triggering it from the gas phase, *i.e.,* with a photon or electron flux, or with a high gas temperature, what if we could trigger it from the particle phase? By illuminating NPs with laser light of a wavelength the NPs absorb strongly, it is possible to locally increase the NP temperature far above the gas temperature [117]. The high NP temperature could, in turn, perhaps induce thermal decomposition locally of the metal-organic precursor, likely resulting in local condensation onto the NPs and reduced homogeneous nucleation of the condensing metal.

# References


[1] W. J. Stark, P. R. Stoessel, W. Wohlleben, and A. Hafner, "Industrial applications of nanoparticles," *Chemical Society Reviews,* vol. 44, no. 16, pp. 5793-5805, 2015.

[2] K. Loza, M. Heggen, and M. Epple, "Synthesis, structure, properties, and applications of bimetallic nanoparticles of noble metals," *Advanced Functional Materials,* vol. 30, no. 21, 2020, Art no. 1909260.

[3] M. Fan, F.-J. Lai, H.-L. Chou, W.-T. Lu, B.-J. Hwang, and A. G. Brolo, "Surface-enhanced Raman scattering (SERS) from Au: Ag bimetallic nanoparticles: the effect of the molecular probe," *Chemical Science,* vol. 4, no. 1, pp. 509-515, 2013.

[4] L. T. Kuhn, A. Bojesen, L. Timmermann, M. M. Nielsen, and S. Mørup, "Structural and magnetic properties of core–shell iron–iron oxide nanoparticles," *Journal of Physics: Condensed Matter,* vol. 14, no. 49, p. 13551, 2002.

[5] Z. Nemati, J. Alonso, H. Khurshid, M. Phan, and H. Srikanth, "Core/shell iron/iron oxide nanoparticles: are they promising for magnetic hyperthermia?," *RSC Advances,* vol. 6, no. 45, pp. 38697-38702, 2016.

[6] S. Gong, Y.-X. Zhang, and Z. Niu, "Recent advances in earth-abundant core/noble-metal shell nanoparticles for electrocatalysis," *ACS Catalysis,* vol. 10, no. 19, pp. 10886-10904, 2020.

[7] S. T. Hunt and Y. Román-Leshkov, "Principles and methods for the rational design of core–shell nanoparticle catalysts with ultralow noble metal loadings," *Accounts of Chemical Research,* vol. 51, no. 5, pp. 1054-1062, 2018.

[8] E. E. Carpenter, "Iron nanoparticles as potential magnetic carriers," *Journal of Magnetism and Magnetic Materials,* vol. 225, no. 1-2, pp. 17-20, 2001.

[9] Y. Cui, B. Ren, J.-L. Yao, R.-A. Gu, and Z.-Q. Tian, "Synthesis of AgcoreAushell bimetallic nanoparticles for immunoassay based on surface-enhanced Raman spectroscopy," *The Journal of Physical Chemistry B,* vol. 110, no. 9, pp. 4002-4006, 2006.

[10] G. P. Kumar, S. Shruthi, B. Vibha, B. A. Reddy, T. K. Kundu, and C. Narayana, "Hot spots in Ag core– Au shell nanoparticles potent for surface-enhanced Raman scattering studies of biomolecules," *The Journal of Physical Chemistry C,* vol. 111, no. 11, pp. 4388-4392, 2007.

[11] M. A. Hines and P. Guyot-Sionnest, "Synthesis and characterization of strongly luminescing ZnS-capped CdSe nanocrystals," *Journal of Physical Chemistry,* Article vol. 100, no. 2, pp. 468-471, 1996.

[12] H. Kim, M. Achermann, L. P. Balet, J. A. Hollingsworth, and V. I. Klimov, "Synthesis and characterization of Co/CdSe core/shell nanocomposites: Bifunctional magnetic-optical nanocrystals," *Journal of the American Chemical Society,* Article vol. 127, no. 2, pp. 544-546, 2005.

[13] G. Chen, S. Desinan, R. Nechache, R. Rosei, F. Rosei, and D. Ma, "Bifunctional catalytic/magnetic Ni@ Ru core–shell nanoparticles," *Chemical Communications,* vol. 47, no. 22, pp. 6308-6310, 2011.

[14] Y. JunáPark, "Demonstration of a magnetic and catalytic Co@Pt nanoparticle as a dual-function nanoplatform," *Chemical Communications,* no. 15, pp. 1619-1621, 2006.

[15] M. Lattuada and T. A. Hatton, "Synthesis, properties and applications of Janus nanoparticles," *Nano Today,* vol. 6, no. 3, pp. 286-308, 2011.

[16] S. Pradhan, D. Ghosh, and S. Chen, "Janus nanostructures based on Au– TiO2 heterodimers and their photocatalytic activity in the oxidation of methanol," *ACS Applied Materials & Interfaces,* vol. 1, no. 9, pp. 2060-2065, 2009.

[17] S. K. Dutta, S. K. Mehetor, and N. Pradhan, "Metal semiconductor heterostructures for photocatalytic conversion of light energy," *The Journal of Physical Chemistry Letters,* vol. 6, no. 6, pp. 936-944, 2015.

[18] J. Feng, G. Biskos, and A. Schmidt-Ott, "Toward industrial scale synthesis of ultrapure singlet nanoparticles with controllable sizes in a continuous gas-phase process," *Scientific Reports,* Article vol. 5, 2015, Art no. 15788.

[19] W. C. Hinds, *Aerosol Technology : Properties, Behavior, and Measurement of Airborne Particles*, 2nd ed. New York: Wiley-Interscience (in English), 1999.

[20] P. M. Winkler and P. E. Wagner, "Characterization techniques for heterogeneous nucleation from the gas phase," *Journal of Aerosol Science,* vol. 159, p. 105875, 2022.

[21] S. K. Friedlander, *Smoke, dust, and haze*, 2nd ed. Oxford University Press New York, 2000.

[22] A. Wiedensohler, "An approximation of the bipolar charge distribution for particles in the submicron size range," *Journal of Aerosol Science,* Article vol. 19, no. 3, pp. 387-389, 1988.

[23] M. Karlsson, *Methods to Generate Size-and Composition Controlled Aerosol Nanoparticles*. Lund University, 2004.

[24] S. Schwyn, E. Garwin, and A. Schmidt-Ott, "Aerosol generation by spark discharge," *Journal of Aerosol Science,* Article vol. 19, no. 5, pp. 639-642, 1988.

[25] H. Burtscher and A. Schmidt-Ott, "In situ measurement of adsorption and condensation of a polyaromatic hydrocarbon on ultrafine C particles by means of photoemission," *Journal of Aerosol Science,* vol. 17, no. 4, pp. 699-703, 1986.

[26] J. H. Byeon, J. H. Park, and J. Hwang, "Spark generation of monometallic and bimetallic aerosol nanoparticles," *Journal of Aerosol Science,* vol. 39, no. 10, pp. 888-896, 2008.

[27] A. Muntean, M. Wagner, J. Meyer, and M. Seipenbusch, "Generation of copper, nickel, and CuNi alloy nanoparticles by spark discharge," *Journal of Nanoparticle Research,* vol. 18, pp. 1-9, 2016.

[28] N. S. Tabrizi, M. Ullmann, V. Vons, U. Lafont, and A. Schmidt-Ott, "Generation of nanoparticles by spark discharge," *Journal of Nanoparticle Research,* vol. 11, pp. 315-332, 2009.

[29] J. Feng, D. Chen, P. V. Pikhitsa, Y.-h. Jung, J. Yang, and M. Choi, "Unconventional alloys confined in nanoparticles: Building blocks for new matter," *Matter,* vol. 3, no. 5, pp. 1646-1663, 2020.

[30] C. Preger, C. Bulbucan, B. O. Meuller, L. Ludvigsson, A. Kostanyan, M. Muntwiler, K. Deppert, R. Westerström, and M. E. Messing, "Controlled oxidation and self-passivation of bimetallic magnetic FeCr and FeMn aerosol nanoparticles," *The Journal of Physical Chemistry C,* vol. 123, no. 26, pp. 16083-16090, 2019.

[31] N. S. Tabrizi, Q. Xu, N. Van Der Pers, U. Lafont, and A. Schmidt-Ott, "Synthesis of mixed metallic nanoparticles by spark discharge," *Journal of Nanoparticle Research,* vol. 11, pp. 1209-1218, 2009.

[32] A. Efimov, A. Lizunova, V. Sukharev, and V. Ivanov, "Synthesis and Characterization of TiO2, Cu2O and Al2O3 Aerosol Nanoparticles Produced by the Multi-Spark Discharge Generator," *Korean Journal of Materials Research,* vol. 26, no. 3, pp. 123-129, 2016.

[33] J.-T. Kim and J.-S. Chang, "Generation of metal oxide aerosol particles by a pulsed spark discharge technique," *Journal of Electrostatics,* vol. 63, no. 6-10, pp. 911-916, 2005.

[34] V. A. Vons, L. C. de Smet, D. Munao, A. Evirgen, E. M. Kelder, and A. Schmidt-Ott, "Silicon nanoparticles produced by spark discharge," *Journal of Nanoparticle Research,* vol. 13, pp. 4867-4879, 2011.

[35] A. Lizunova, A. Mazharenko, B. Masnaviev, E. Khramov, A. Efimov, A. Ramanenka, I. Shuklov, and V. Ivanov, "Effects of Temperature on the Morphology and Optical Properties of Spark Discharge Germanium Nanoparticles," *Materials,* vol. 13, no. 19, p. 4431, 2020.

[36] D. Lee, K. Lee, D. S. Kim, J.-K. Lee, S. J. Park, and M. Choi, "Hydrogen-assisted spark discharge generation of highly crystalline and surface-passivated silicon nanoparticles," *Journal of Aerosol Science,* vol. 114, pp. 139-145, 2017.

[37] A. Maisser, K. Barmpounis, M. Attoui, G. Biskos, and A. Schmidt-Ott, "Atomic cluster generation with an atmospheric pressure spark discharge generator," *Aerosol Science and Technology,* vol. 49, no. 10, pp. 886-894, 2015.

[38] E. Hontañón, J. M. Palomares, M. Stein, X. Guo, R. Engeln, H. Nirschl, and F. E. Kruis, "The transition from spark to arc discharge and its implications with respect to nanoparticle production," *Journal of Nanoparticle Research,* vol. 15, pp. 1-19, 2013.

[39] B. O. Meuller, M. E. Messing, D. L. Engberg, A. M. Jansson, L. I. Johansson, S. M. Norlén, N. Tureson, and K. Deppert, "Review of spark discharge generators for production of nanoparticle aerosols," *Aerosol Science and Technology,* vol. 46, no. 11, pp. 1256-1270, 2012.

[40] T. Pfeiffer, J. Feng, and A. Schmidt-Ott, "New developments in spark production of nanoparticles," *Advanced Powder Technology,* vol. 25, no. 1, pp. 56-70, 2014.

[41] S. R. Noh, D. Lee, S. J. Park, D. S. Kim, and M. Choi, "High throughput nanoparticle generation utilizing high-frequency spark discharges via rapid spark plasma removal," *Aerosol Science and Technology,* vol. 51, no. 1, pp. 116-122, 2017.

[42] J.-M. Palomares, A. Kohut, G. Galbács, R. Engeln, and Z. Geretovszky, "A time-resolved imaging and electrical study on a high current atmospheric pressure spark discharge," *Journal of Applied Physics,* vol. 118, no. 23, 2015, Art no. 233305.

[43] D. Mylnikov, A. Efimov, and V. Ivanov, "Measuring and optimization of energy transfer to the interelectrode gaps during the synthesis of nanoparticles in a spark discharge," *Aerosol Science and Technology,* vol. 53, no. 12, pp. 1393-1403, 2019.

[44] A. Kohut, G. Galbács, Z. Márton, and Z. Geretovszky, "Characterization of a copper spark discharge plasma in argon atmosphere used for nanoparticle generation," *Plasma Sources Science and Technology,* vol. 26, no. 4, p. 045001, 2017.

[45] A. Kohut, L. Ludvigsson, B. O. Meuller, K. Deppert, M. E. Messing, G. Galbács, and Z. Geretovszky, "From plasma to nanoparticles: optical and particle emission of a spark discharge generator," *Nanotechnology,* vol. 28, no. 47, p. 475603, 2017.

[46] A. Kohut, L. Villy, T. Ajtai, Z. Geretovszky, and G. Galbács, "The effect of circuit resistance on the particle output of a spark discharge nanoparticle generator," *Journal of Aerosol Science,* vol. 118, pp. 59-63, 2018.

[47] J. Feng, N. Ramlawi, G. Biskos, and A. Schmidt-Ott, "Internally mixed nanoparticles from oscillatory spark ablation between electrodes of different materials," *Aerosol Science and Technology,* vol. 52, no. 5, pp. 505-514, 2018.

[48] A. Kohut, L. P. Villy, A. Kéri, Á. Bélteki, D. Megyeri, B. Hopp, G. Galbács, and Z. Geretovszky, "Full range tuning of the composition of Au/Ag binary nanoparticles by spark discharge generation," *Scientific Reports,* vol. 11, no. 1, p. 5117, 2021.

[49] T. F. Boucher, M. V. Ozanne, M. L. Carmosino, M. D. Dyar, S. Mahadevan, E. A. Breves, K. H. Lepore, and S. M. Clegg, "A study of machine learning regression methods for major elemental analysis of rocks using laser-induced breakdown spectroscopy," *Spectrochimica Acta Part B: Atomic Spectroscopy,* vol. 107, pp. 1-10, 2015.

[50] R. Tibshirani, "Regression shrinkage and selection via the lasso," *Journal of the Royal Statistical Society Series B: Statistical Methodology,* vol. 58, no. 1, pp. 267-288, 1996.

[51] S. A. Davari and A. S. Wexler, "Quantification of toxic metals using machine learning techniques and spark emission spectroscopy," *Atmospheric Measurement Techniques,* vol. 13, no. 10, pp. 5369-5377, 2020.

[52] H. Li, L. Mazzei, C. D. Wallis, and A. S. Wexler, "Improving quantitative analysis of spark-induced breakdown spectroscopy: Multivariate calibration of metal particles using machine learning," *Journal of Aerosol Science,* vol. 159, p. 105874, 2022.

[53] L. Zheng, P. Kulkarni, and P. Diwakar, "Spatial and temporal dynamics of a pulsed spark microplasma used for aerosol analysis," *Spectrochimica Acta Part B: Atomic Spectroscopy,* vol. 144, pp. 55-62, 2018.

[54] T. V. Pfeiffer, P. Kedia, M. E. Messing, M. Valvo, and A. Schmidt-Ott, "Precursor-less coating of nanoparticles in the gas phase," *Materials,* vol. 8, no. 3, pp. 1027-1042, 2015.

[55] J. Feng, L. Huang, L. Ludvigsson, M. E. Messing, A. Maisser, G. Biskos, and A. Schmidt-Ott, "General approach to the evolution of singlet nanoparticles from a rapidly quenched point source," *The Journal of Physical Chemistry C,* vol. 120, no. 1, pp. 621-630, 2016.

[56] W. Koch and S. Friedlander, "The effect of particle coalescence on the surface area of a coagulating aerosol," *Journal of Colloid and Interface Science,* vol. 140, no. 2, pp. 419-427, 1990.

[57] M. R. Zachariah and M. J. Carrier, "Molecular dynamics computation of gas-phase nanoparticle sintering: a comparison with phenomenological models," *Journal of Aerosol Science,* vol. 30, no. 9, pp. 1139-1151, 1999.

[58] M. L. Eggersdorfer and S. E. Pratsinis, "Agglomerates and aggregates of nanoparticles made in the gas phase," *Advanced Powder Technology,* vol. 25, no. 1, pp. 71-90, 2014.

[59] C. Preger, N. C. Overgaard, M. E. Messing, and M. H. Magnusson, "Predicting the deposition spot radius and the nanoparticle concentration distribution in an electrostatic precipitator," *Aerosol Science and Technology,* vol. 54, no. 6, pp. 718-728, 2020.

[60] M. Karlsson, K. Deppert, L. Karlsson, M. Magnusson, J.-O. Malm, and N. Srinivasan, "Compaction of agglomerates of aerosol nanoparticles: A compilation of experimental data," *Journal of Nanoparticle Research,* vol. 7, pp. 43-49, 2005.

[61] E. Ringe, R. P. Van Duyne, and L. Marks, "Wulff construction for alloy nanoparticles," *Nano Letters,* vol. 11, no. 8, pp. 3399-3403, 2011.

[62] M. Seipenbusch, A. Weber, A. Schiel, and G. Kasper, "Influence of the gas atmosphere on restructuring and sintering kinetics of nickel and platinum aerosol nanoparticle agglomerates," *Journal of Aerosol Science,* vol. 34, no. 12, pp. 1699-1709, 2003.

[63] A. P. Weber and S. K. Friedlander, "In situ determination of the activation energy for restructuring of nanometer aerosol agglomerates," *Journal of Aerosol Science,* vol. 28, no. 2, pp. 179-192, 1997.

[64] K. Nakaso, M. Shimada, K. Okuyama, and K. Deppert, "Evaluation of the change in the morphology of gold nanoparticles during sintering," *Journal of Aerosol Science,* vol. 33, no. 7, pp. 1061-1074, 2002.

[65] J. Lee, J. Lee, T. Tanaka, and H. Mori, "In situ atomic-scale observation of melting point suppression in nanometer-sized gold particles," *Nanotechnology,* vol. 20, no. 47, p. 475706, 2009.

[66] C. Alcock, V. Itkin, and M. Horrigan, "Vapour pressure equations for the metallic elements: 298–2500K," *Canadian Metallurgical Quarterly,* vol. 23, no. 3, pp. 309-313, 1984.

[67] M. E. Messing, "Engineered Nanoparticles Generation, Characterization and Applications," Lund University, 2011.

[68] M. E. Messing, R. Westerström, B. O. Meuller, S. Blomberg, J. Gustafson, J. N. Andersen, E. Lundgren, R. van Rijn, O. Balmes, and H. Bluhm, "Generation of Pd model catalyst nanoparticles by spark discharge," *The Journal of Physical Chemistry C,* vol. 114, no. 20, pp. 9257-9263, 2010.

[69] C. Yang, B. H. Ko, S. Hwang, Z. Liu, Y. Yao, W. Luc, M. Cui, A. S. Malkani, T. Li, and X. Wang, "Overcoming immiscibility toward bimetallic catalyst library," *Science Advances,* vol. 6, no. 17, p. eaaz6844, 2020.

[70] C. Langlois, Z. Li, J. Yuan, D. Alloyeau, J. Nelayah, D. Bochicchio, R. Ferrando, and C. Ricolleau, "Transition from core–shell to Janus chemical configuration for bimetallic nanoparticles," *Nanoscale,* vol. 4, no. 11, pp. 3381-3388, 2012.

[71] W. T. Osowiecki, X. Ye, P. Satish, K. C. Bustillo, E. L. Clark, and A. P. Alivisatos, "Tailoring morphology of Cu–Ag nanocrescents and core–shell nanocrystals guided by a thermodynamic model," *Journal of the American Chemical Society,* vol. 140, no. 27, pp. 8569-8577, 2018.

[72] C. Langlois, D. Alloyeau, Y. Le Bouar, A. Loiseau, T. Oikawa, C. Mottet, and C. Ricolleau, "Growth and structural properties of CuAg and CoPt bimetallic nanoparticles," *Faraday Discussions,* vol. 138, pp. 375-391, 2008.

[73] G. A. Kamat, C. Yan, W. T. Osowiecki, I. A. Moreno-Hernandez, M. Ledendecker, and A. P. Alivisatos, "Self-limiting shell formation in Cu@ Ag Core–shell nanocrystals during galvanic replacement," *The Journal of Physical Chemistry Letters,* vol. 11, no. 13, pp. 5318-5323, 2020.

[74] N. S. Tabrizi, Q. Xu, N. Van Der Pers, and A. Schmidt-Ott, "Generation of mixed metallic nanoparticles from immiscible metals by spark discharge," *Journal of Nanoparticle Research,* vol. 12, pp. 247-259, 2010.

[75] R. T. Hallberg, L. Ludvigsson, C. Preger, B. O. Meuller, K. A. Dick, and M. E. Messing, "Hydrogen-assisted spark discharge generated metal nanoparticles to prevent oxide formation," *Aerosol Science and Technology,* Article vol. 52, no. 3, pp. 347-358, 2018.

[76] C. Srivastava, D. E. Nikles, and G. B. Thompson, "Tailoring nucleation and growth conditions for narrow compositional distributions in colloidal synthesized FePt nanoparticles," *Journal of Applied Physics,* vol. 104, no. 10, 2008, Art no. 104314.

[77] P. Williams, Y. Mishin, and J. Hamilton, "An embedded-atom potential for the Cu–Ag system," *Modelling and Simulation in Materials Science and Engineering,* vol. 14, no. 5, p. 817, 2006.

[78] D. Rossouw, P. Burdet, F. de la Peña, C. Ducati, B. R. Knappett, A. E. Wheatley, and P. A. Midgley, "Multicomponent signal unmixing from nanoheterostructures: overcoming the traditional challenges of nanoscale X-ray analysis via machine learning," *Nano Letters,* vol. 15, no. 4, pp. 2716-2720, 2015.

[79] P. Torruella Besa, "Development of novel EELS methods to unveil nanoparticle properties," Universitat de Barcelona, 2019.

[80] N. Braidy and R. Gosselin, "Unmixing noisy co-registered spectrum images of multicomponent nanostructures," *Scientific Reports,* vol. 9, no. 1, p. 18797, 2019.

[81] B. Jany, A. Janas, and F. Krok, "Retrieving the quantitative chemical information at nanoscale from scanning electron microscope energy dispersive X-ray measurements by machine learning," *Nano Letters,* vol. 17, no. 11, pp. 6520-6525, 2017.

[82] R. Ferrando, J. Jellinek, and R. L. Johnston, "Nanoalloys: from theory to applications of alloy clusters and nanoparticles," *Chemical Reviews,* vol. 108, no. 3, pp. 845-910, 2008.

[83] M. Rahm, R. Hoffmann, and N. Ashcroft, "Atomic and ionic radii of elements 1–96," *Chemistry–A European Journal,* vol. 22, no. 41, pp. 14625-14632, 2016.

[84] L. Vitos, A. V. Ruban, H. L. Skriver, and J. Kollár, "The surface energy of metals," *Surface Science,* vol. 411, no. 1-2, pp. 186-202, 1998.

[85] W. Qi and M. Wang, "Size effect on the cohesive energy of nanoparticle," *Journal of Materials Science Letters,* vol. 21, pp. 1743-1745, 2002.

[86] N. Eom, M. E. Messing, J. Johansson, and K. Deppert, "General trends in core–shell preferences for bimetallic nanoparticles," *ACS Nano,* vol. 15, no. 5, pp. 8883-8895, 2021.

[87] S. Lai, J. Guo, V. Petrova, G. Ramanath, and L. Allen, "Size-dependent melting properties of small tin particles: nanocalorimetric measurements," *Physical Review Letters,* vol. 77, no. 1, p. 99, 1996.

[88] L. J. Lewis, P. Jensen, and J.-L. Barrat, "Melting, freezing, and coalescence of gold nanoclusters," *Physical Review B,* vol. 56, no. 4, p. 2248, 1997.

[89] H. Farrell and C. Van Siclen, "Binding energy, vapor pressure, and melting point of semiconductor nanoparticles," *Journal of Vacuum Science & Technology B: Microelectronics and Nanometer Structures Processing, Measurement, and Phenomena,* vol. 25, no. 4, pp. 1441-1447, 2007.

[90] K. Nanda, A. Maisels, F. Kruis, H. Fissan, and S. Stappert, "Higher surface energy of free nanoparticles," *Physical Review Letters,* vol. 91, no. 10, p. 106102, 2003.

[91] D. Llamosa, M. Ruano, L. Martínez, A. Mayoral, E. Roman, M. García-Hernández, and Y. Huttel, "The ultimate step towards a tailored engineering of core@ shell and core@ shell@ shell nanoparticles," *Nanoscale,* vol. 6, no. 22, pp. 13483-13486, 2014.

[92] J. Hanuš, M. Vaidulych, O. Kylián, A. Choukourov, J. Kousal, I. Khalakhan, M. Cieslar, P. Solař, and H. Biederman, "Fabrication of Ni@ Ti core–shell nanoparticles by modified gas aggregation source," *Journal of Physics D: Applied Physics,* vol. 50, no. 47, p. 475307, 2017.

[93] P. Grammatikopoulos, J. Kioseoglou, A. Galea, J. Vernieres, M. Benelmekki, R. E. Diaz, and M. Sowwan, "Kinetic trapping through coalescence and the formation of patterned Ag–Cu nanoparticles," *Nanoscale,* vol. 8, no. 18, pp. 9780-9790, 2016.

[94] J.-G. Mattei, P. Grammatikopoulos, J. Zhao, V. Singh, J. Vernieres, S. Steinhauer, A. Porkovich, E. Danielson, K. Nordlund, and F. Djurabekova, "Gas-phase synthesis of trimetallic nanoparticles," *Chemistry of Materials,* vol. 31, no. 6, pp. 2151-2163, 2019.

[95] M. N. Karlsson, K. Deppert, M. H. Magnusson, L. S. Karlsson, and J.-O. Malm, "Size- and composition-controlled Au–Ga aerosol nanoparticles," *Aerosol Science and Technology,* vol. 38, no. 9, pp. 948-954, 2004.

[96] J. Harra, P. Juuti, J. Haapanen, M. Sorvali, E. Roumeli, M. Honkanen, M. Vippola, J. Yli-Ojanperä, and J. M. Mäkelä, "Coating of silica and titania aerosol nanoparticles by silver vapor condensation," *Aerosol Science and Technology,* vol. 49, no. 9, pp. 767-776, 2015.

[97] A. M. Boies, P. Lei, S. Calder, and S. L. Girshick, "Gas-phase production of gold-decorated silica nanoparticles," *Nanotechnology,* Article vol. 22, no. 31, 2011, Art no. 315603.

[98] H. Okamoto and T. Massalski, "The Au-Zn (gold-zinc) system," *Bulletin of Alloy Phase Diagrams,* vol. 10, no. 1, pp. 59-69, 1989.

[99] M. H. Braga, J. Vizdal, A. Kroupa, J. Ferreira, D. Soares, and L. F. Malheiros, "The experimental study of the Bi-Sn, Bi-Zn and Bi-Sn-Zn systems," *Calphad: Computer Coupling of Phase Diagrams and Thermochemistry,* Article vol. 31, no. 4, pp. 468-478, 2007.

[100] D. V. Malakhov, "Thermodynamic assessment of the Bi-Zn system," *Calphad: Computer Coupling of Phase Diagrams and Thermochemistry,* Article vol. 24, no. 1, pp. 1-14, 2000.

[101] Z. Moser, J. Dutkiewicz, W. Gasior, and J. Salawa, "The Sn– Zn (tin-zinc) system," *Bulletin of Alloy Phase Diagrams,* vol. 6, no. 4, pp. 330-334, 1985.

[102] H. S. Fogler, "Distributions of Residence Times for Chemical Reactors," in *Elements of Chemical Reactor Engineering*, 3 ed. (Prentice Hall international series in the physical and chemical engineering sciences. Upper Saddle River, N.J. Prentice-Hall, 1999, ch. 13.

[103] F. R. De Boer, W. Mattens, R. Boom, A. Miedema, and A. Niessen, "Cohesion in metals. Transition metal alloys," vol. 1. Netherlands, 1988.

[104] W. Tyson and W. Miller, "Surface free energies of solid metals: Estimation from liquid surface tension measurements," *Surface Science,* vol. 62, no. 1, pp. 267-276, 1977.

[105] R. Nakamura, J. G. Lee, D. Tokozakura, H. Mori, and H. Nakajima, "Formation of hollow ZnO through low-temperature oxidation of Zn nanoparticles," *Materials Letters,* Article vol. 61, no. 4-5, pp. 1060-1063, 2007.

[106] A. M. Boies, J. T. Roberts, S. L. Girshick, B. Zhang, T. Nakamura, and A. Mochizuki, "SiO2 coating of silver nanoparticles by photoinduced chemical vapor deposition," *Nanotechnology,* Article vol. 20, no. 29, 2009, Art no. 295604.

[107] H. Nasri Lari, J. Chaouki, and J. R. Tavares, "Continuous aerosol photopolymerization to coat de-agglomerated nanoparticles," *Chemical Engineering Journal,* Article vol. 390, 2020, Art no. 124526.

[108] B. Zhang, Y. C. Liao, S. L. Girshick, and J. T. Roberts, "Growth of coatings on nanoparticles by photoinduced chemical vapor deposition," *Journal of Nanoparticle Research,* Article vol. 10, no. 1, pp. 173-178, 2008.

[109] M. Shaban, J. Poostforooshan, and A. P. Weber, "Surface-initiated polymerization on unmodified inorganic semiconductor nanoparticles via surfactant-free aerosol-based synthesis toward core–shell nanohybrids with a tunable shell thickness," *Journal of Materials Chemistry A,* vol. 5, no. 35, pp. 18651-18663, 2017.

[110] K. Chatterjee, S. Sarkar, K. J. Rao, and S. Paria, "Core/shell nanoparticles in biomedical applications," *Advances in colloid and interface science,* vol. 209, pp. 8-39, 2014.

[111] Z. Wu, L. Li, T. Liao, X. Chen, W. Jiang, W. Luo, J. Yang, and Z. Sun, "Janus nanoarchitectures: From structural design to catalytic applications," *Nano Today,* vol. 22, pp. 62-82, 2018.

[112] L. Ludvigsson, B. O. Meuller, and M. E. Messing, "Investigations of initial particle stages during spark discharge," *Journal of Physics D: Applied Physics,* vol. 48, no. 31, p. 314012, 2015.

[113] A. Efimov, V. Ivanov, A. Bagazeev, I. Beketov, I. Volkov, and S. Shcherbinin, "Generation of aerosol nanoparticles by the multi-spark discharge generator," *Technical Physics Letters,* vol. 39, pp. 1053-1056, 2013.

[114] V. V. Ivanov, A. A. e. Efimov, D. A. Mylnikov, A. A. Lizunova, A. V. Bagazeev, I. V. Beketov, and S. V. e. Shcherbinin, "High-efficiency synthesis of nanoparticles in a repetitive multigap spark discharge generator," *Technical Physics Letters,* vol. 42, pp. 876-878, 2016.

[115] K.-T. Park, M. M. Farid, and J. Hwang, "Anti-agglomeration of spark discharge-generated aerosols via unipolar air ions," *Journal of Aerosol Science,* vol. 67, pp. 144-156, 2014.

[116] S. M. Franzén, L. Jönsson, P. Ternero, M. Kåredal, A. Eriksson, J.-M. Hübner, and M. E. Messing, "Compositional tuning of gas-phase synthesized Pd-Cu nanoparticles," *Nanoscale Advances,* 2023.

[117] P. Samuelsson, "Towards optical diagnostics and control in aerotaxy semiconductor nanowire growth," Lund University, 2021.

[118] F. Anabitarte, A. Cobo, and J. M. Lopez-Higuera, "Laser-induced breakdown spectroscopy: fundamentals, applications, and challenges," *International Scholarly Research Notices,* vol. 2012, p. 285240, 2012.

[119] R. B. Anderson, J. F. Bell III, R. C. Wiens, R. V. Morris, and S. M. Clegg, "Clustering and training set selection methods for improving the accuracy of quantitative laser induced breakdown spectroscopy," *Spectrochimica Acta Part B: Atomic Spectroscopy,* vol. 70, pp. 24-32, 2012.

[120] H. Li, L. Mazzei, C. D. Wallis, S. A. Davari, and A. S. Wexler, "The performance of an inexpensive spark-induced breakdown spectroscopy instrument for near real-time analysis of toxic metal particles," *Atmospheric Environment,* vol. 264, p. 118666, 2021.

[121] H. Liao, A. Fisher, and Z. J. Xu, "Surface segregation in bimetallic nanoparticles: a critical issue in electrocatalyst engineering," *Small,* vol. 11, no. 27, pp. 3221-3246, 2015.

[122] M. Patanen, I. Unger, C.-M. Saak, G. Gopakumar, R. Lexelius, O. Björneholm, M. Salter, and P. Zieger, "Surface composition of size-selected sea salt particles under the influence of organic acids studied in situ using synchrotron radiation X-ray photoelectron spectroscopy," *Environmental Science: Atmospheres,* vol. 2, no. 5, pp. 1032-1040, 2022.

[123] O. Sublemontier, C. Nicolas, D. Aureau, M. Patanen, H. Kintz, X. Liu, M.-A. Gaveau, J.-L. Le Garrec, E. Robert, and F.-A. Barreda, "X-ray photoelectron spectroscopy of isolated nanoparticles," *The journal of physical chemistry letters,* vol. 5, no. 19, pp. 3399-3403, 2014.

[124] L. Zhou and M. R. Zachariah, "Size resolved particle work function measurement of free nanoparticles: Aggregates vs. spheres," *Chemical Physics Letters,* vol. 525, pp. 77-81, 2012.

[125] J. Röhrbein and A. P. Weber, "A system for on-line characterization of gas-borne particle surface properties based on their photoemission," *Journal of Aerosol Science,* vol. 120, pp. 82-91, 2018.

[126] K. Khabarov, M. Nouraldeen, S. Tikhonov, A. Lizunova, O. Seraya, E. Filalova, and V. Ivanov, "Comparison of Aerosol Pt, Au and Ag Nanoparticles Agglomerates Laser Sintering," *Materials,* vol. 15, no. 1, p. 227, 2021.

[127] K. Khabarov, M. Nouraldeen, S. Tikhonov, A. Lizunova, A. Efimov, and V. Ivanov, "Modification of Aerosol Gold Nanoparticles by Nanosecond Pulsed-Periodic Laser Radiation," *Nanomaterials,* vol. 11, no. 10, p. 2701, 2021.

[128] A. Perdikaki, A. Galeou, G. Pilatos, I. Karatasios, N. K. Kanellopoulos, A. Prombona, and G. N. Karanikolos, "Ag and Cu monometallic and Ag/Cu bimetallic nanoparticle–graphene composites with enhanced antibacterial performance," *ACS Applied Materials & Interfaces,* vol. 8, no. 41, pp. 27498-27510, 2016.

[129] A. Dutta, S. K. Dutta, S. K. Mehetor, I. Mondal, U. Pal, and N. Pradhan, "Oriented attachments and formation of ring-on-disk heterostructure Au–Cu3P photocatalysts," *Chemistry of Materials,* vol. 28, no. 6, pp. 1872-1878, 2016.

[130] Z. Zhao, E. J. Willard, J. R. Dominguez, Z. Wu, and F. E. Osterloh, "Depletion layer controls photocatalytic hydrogen evolution with p-type gallium phosphide particles," *Journal of Materials Chemistry A,* vol. 7, no. 30, pp. 18020-18029, 2019.

[131] S. Sivakumar, A. R. Persson, W. Metaferia, M. Heurlin, R. Wallenberg, L. Samuelson, K. Deppert, J. Johansson, and M. H. Magnusson, "Aerotaxy: gas-phase epitaxy of quasi 1D nanostructures," *Nanotechnology,* vol. 32, no. 2, p. 025605, 2020.

[132] P. Samuelsson, M. H. Magnusson, K. Deppert, M. Aldén, and Z. Li, "Quantitative laser diagnostics on trimethylindium pyrolysis and photolysis for functional nanoparticle growth," *Measurement Science and Technology,* vol. 33, no. 5, p. 055201, 2022.

[133] M. Karlsson, K. Deppert, B. Wacaser, L. Karlsson, and J.-O. Malm, "Size-controlled nanoparticles by thermal cracking of iron pentacarbonyl," *Applied Physics A,* vol. 80, pp. 1579-1583, 2005.

[134] F. Weis, M. Seipenbusch, and G. Kasper, "Film Growth Rates and Activation Energies for Core-Shell Nanoparticles Derived from a CVD Based Aerosol Process," *Materials,* vol. 8, no. 3, pp. 966-976, 2015.

Printed by Media-Tryck, Lund 2023 NORDIC SWAN ECOLABEL 3041 0903

Clouds are some of the most well-known aerosols: a mixture of liquid and/or solid particles in a gas. Clouds form by water condensation onto small particles in the atmosphere. In this thesis, I create aerosols of heterogeneous nanoparticles by condensing metal vapors onto metal particles. The front cover shows measurements of a gold aerosol growing by zinc condensation.

LUND UNIVERSITY

Faculty of Engineering
Department of Physics
Solid State Physics

ISBN 978-91-8039-874-9